

Fall 2011

Buoyancy-driven motion of bubbles in the presence of soluble surfactants

Weihua Li

University of New Hampshire, Durham

Follow this and additional works at: <https://scholars.unh.edu/thesis>

Recommended Citation

Li, Weihua, "Buoyancy-driven motion of bubbles in the presence of soluble surfactants" (2011). *Master's Theses and Capstones*. 663.
<https://scholars.unh.edu/thesis/663>

This Thesis is brought to you for free and open access by the Student Scholarship at University of New Hampshire Scholars' Repository. It has been accepted for inclusion in Master's Theses and Capstones by an authorized administrator of University of New Hampshire Scholars' Repository. For more information, please contact nicole.hentz@unh.edu.

**BUOYANCY-DRIVEN MOTION OF BUBBLES IN
THE PRESENCE OF SOLUBLE SURFACTANTS**

By

Weihua LI

B.S. Environmental Engineering, Xi'an Jiaotong University, July, 2007

THESIS

Submitted to the University of New Hampshire

in Partial Fulfillment of

the Requirements for the Degree of Masters of Science

in

Chemical Engineering

September 2011

UMI Number: 1504955

All rights reserved

INFORMATION TO ALL USERS

The quality of this reproduction is dependent upon the quality of the copy submitted.

In the unlikely event that the author did not send a complete manuscript and there are missing pages, these will be noted. Also, if material had to be removed, a note will indicate the deletion.



UMI 1504955

Copyright 2011 by ProQuest LLC.

All rights reserved. This edition of the work is protected against unauthorized copying under Title 17, United States Code.



ProQuest LLC

789 East Eisenhower Parkway

P.O. Box 1346

Ann Arbor, MI 48106-1346

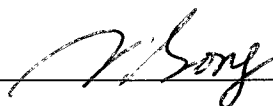
This thesis has been examined and approved.



Nivedita R. Gupta,
Thesis Director,
Associate Professor of Chemical Engineering



Palligarnai T. Vasudevan,
Professor and Chair of Chemical Engineering



Qing Song,
Assistant Professor of Chemical Engineering

AUGUST 22, 2011

Date

DEDICATION

To Yumin Li and Ruiqiao Ge

ACKNOWLEDGEMENTS

I am heartily thankful to my advisor, Dr. Nivedita Gupta, whose encouragement, guidance and support from the initial to the final level enabled me to develop an understanding of the subject. I would like to thank Dr. Vasu and Dr. Song for taking time to be on my thesis committee.

I consider it an honor to work with Yuanyuan Cui, Michelle Liu and Ruizhi He. They give me many useful suggestions and help me with instruments operation at Interfacial Phenomena Lab. I also would like to thank Mr. Jonathan E. Newell for his assistance with customized capillaries.

Lastly, I offer my regards and blessings to all of those who supported me in any respect during the completion of the project.

TABLE OF CONTENTS

DEDICATION	iii
ACKNOWLEDGMENTS	iv
LIST OF TABLES.....	vii
LIST OF FIGURES.....	viii
ABSTRACT	xiv
CHAPTER	PAGE
1. INTRODUCTION	1
1.1 FLUID RHEOLOGY EFFECT	3
1.2 SURFACTANT EFFECTS	6
1.3 OBJECTIVES.....	10
2. BACKGROUND	12
2.1 DROPS RISING IN NEWTONIAN FLUID.....	12
2.1.1 Unbounded Flows.....	12
2.1.2 Flow in Cylindrical Tubes	13
2.1.3 Flow in Non-circular Tubes.....	16
2.2 FLUID RHEOLOGY EFFECT	18
2.2.1 Unbounded Flows.....	18
2.2.2 Flow in Cylindrical Tubes	20
2.3 SURFACTANT EFFECTS	20
2.3.1 Unbounded Flows.....	20
2.3.2 Flow in Cylindrical Tubes	23
3. EXPERIMENTAL METHODS	26
3.1 Experimental Setup	26
3.2 Materials and Chemicals	28

3.3 Operating Procedure.....	29
3.4 Fluid Property Measurement.....	32
3.4.1 Newtonian Rheology	33
3.4.2 Non-Newtonian Rheology	34
3.4.3 Surface Tension	39
3.5 Model Problem.....	45
3.6 Data Analysis	47
3.7 Dimensionless Parameter Space.....	52
4. RESULTS AND DISCUSSION.....	56
4.1 NEWTONIAN BULK FLUID.....	57
4.1.1 Surfactant-free System	57
4.1.2 Surfactant-laden System.....	63
4.1.2.1 Surfactant Concentrations Below CMC.....	65
4.1.2.2 Surfactant Concentrations Above CMC.....	79
4.2 NON-NEWTONIAN BULK FLUID.....	86
4.2.1 Surfactant-free System	86
4.2.2 Surfactant-laden System.....	95
4.2.2.1 Surfactant Concentrations Below CMC.....	95
4.2.2.2 Surfactant Concentrations Above CMC.....	105
5. SUMMARY AND FUTURE WORK	110
6. REFERENCES.....	115

LIST OF TABLES

Table	Page
3.1: Channel geometries considered for studying dynamics of drops and bubbles rising in a channel filled with an immiscible fluid.....	27
3.2: Properties of the chemicals used in the experiments for studying dynamics of drops and bubbles rising in a channel filled with an immiscible fluid.	30
3.3: Material properties of Newtonian systems studied.....	46
3.4: Material properties and range of dimensionless parameters of systems studied	48
3.5: The range of dimensionless parameters of Newtonian systems studied.....	54
3.6: The range of dimensionless parameters of Non-Newtonian systems studied.....	55

LIST OF FIGURES

Figure	Page
1.1: Schematic showing the Weissenberg effect (or rod-climbing) in a polymeric fluid...	5
1.2: Shapes of the broad edge of the two-dimensional cusps	6
1.3: Schematic of equilibrium behavior of surfactant molecules at an air-water interface.	7
1.4: Schematic of equilibrium surface tension as a function of bulk surfactant concentration.....	8
1.5: Schematic of surfactant molecules non-equilibrium behavior at interface.	9
2.1: Schematic of the velocity field near the leading edge of a Taylor bubble rising in a stagnant fluid.....	14
2.2: Schematic of the velocity field in the wake of a Taylor bubble rising in a stagnant fluid.....	14
3.1: Schematic of the experimental setup used to study the buoyancy-driven motion of bubbles in channels.....	27
3.2: Shear stress as a function of shear rate for 75 wt % glycerol-water solution.	34
3.3: Frequency dependence of G' and G'' for 2 wt% carboxymethyl cellulose solution...	36
3.4: Frequency dependence of G' and G'' for 0.1 wt% polyacrylamide solution.	36
3.5: Frequency dependence of G' and G'' for 0.3 wt% polyacrylamide solution.	37
3.6: Steady shear viscosity as a function of shear rate for 2 wt% carboxymethyl cellulose, 0.1 wt% polyacrylamide, and 0.3 wt% polyacrylamide solutions.....	38
3.7: Surface tension of Triton X-100 in 75 wt% glycerol water solution.....	41
3.8: Surface tension of Aerosol-OT in 75 wt% glycerol water solution.....	41
3.9: Surface tension SDS in 75 wt% glycerol water solution.....	42

3.10: Surface tension of Triton X-100 in 2 wt% carboxymethyl cellulose solution_	42
3.11: Surface tension of Tergitol 15-S-9 in 2 wt% carboxymethyl cellulose solution.....	43
3.12: Surface tension of Triton X-100 in 0.1wt% polyacrylamide solution.....	43
3.13: Surface tension of Triton X-100 in 0.3 wt% polyacrylamide solution.....	44
3.14: Schematic of the front view and the cross-sectional view of a bubble or drop rising through a channel. This bubble may be (a), (b) and (d) axisymmetric or (c) and (e) non-axisymmetric in the cross-sectional view.	49
3.15: Schematic of the data analysis using National Instruments Vision Assistant.	50
3.16: Volume calculation for square and circular channels: Volume of evolution	51
3.17: Area calculation for rectangular channels	51
4.1: Terminal velocity of steady bubbles as a function of bubble size for bubbles rising in 75 wt% glycerol water solution in 10×10 mm square channel (2-G). The open symbols correspond to the bubbles presented in the figure.....	58
4.2: Terminal velocity of steady bubbles normalized with the Hadamard-Rybczynski velocity as a function of dimensionless bubble size for bubbles rising in 75 wt% glycerol water solution in 10×10 mm square channel (2-G).	58
4.3: Length versus width for bubble rising in 75 wt% glycerol water solution in 10×10 mm square channel (2-G). The dashed line represents $L = B$ line. The open symbols correspond to the bubble shapes presented in Figure 4.1.	60
4.4: Deformation parameter as a function of dimensionless bubble size for bubble rising in 75 wt% glycerol water solution in 10×10 mm square channel (2-G). The open symbols correspond to the bubble shapes presented in Figure 4.1.....	61
4.5: Dimensionless film thickness as a function of dimensionless bubble size for bubble rising in 75 wt% glycerol water solution in 10×10mm square channel (2-G). The open symbols correspond to the bubble shapes presented in Figure 4.1.....	61
4.6: Comparison of terminal velocity as a function of bubble size for steady bubbles rising in 75 wt% glycerol water solution in a circular tube (1-G) and square channel (2-G) with $D_H=10\text{mm}$	63
4.7: The bubble shapes corresponding to different bubble terminal velocity as a function of bubble size for 75 wt% glycerol water solution in a circular tube (1-G) and square channel (2-G) with $D_H=10\text{mm}$	64
4.8: Comparison of deformation parameter for steady bubbles rising in 75 wt% glycerol water solution in a circular tube (1-G) and square channel (2-G) with $D_H=10\text{mm}$	64

4.9: Comparison of film thickness as a function of bubble size for steady bubbles rising in 75 wt% glycerol water solution in a circular tube (1-G) and square channel (2-G) with $D_H=10\text{mm}$	65
4.10: Schematic of a bubble rising in a channel in the presence of surfactants.....	66
4.11: The terminal velocity as a function of bubble size for bubble rising in 75 wt% glycerol water solution at low concentrations of AOT in 10mm × 10 mm square channel.	69
4.12: The terminal velocity as a function of bubble size for bubble rising in 75 wt% glycerol water solution with tiny amount of TX-100 in 10mm × 10 mm square channel.	69
4.13: The terminal velocity as a function of bubble size for bubble rising in 75 wt% glycerol water solution with tiny amount of TX-100 in 16mm × 3 mm rectangular channel.	70
4.14: The terminal velocity as a function of bubble size for bubbles rising in 75 wt% glycerol water solution with various concentration (below CMC) of AOT in 10mm × 10 mm square channel.	70
4.15: Comparison of deformation parameter for steady bubbles rising in 75 wt% glycerol water solution with various concentration (below CMC) of AOT in a square channel with $D_H=10\text{mm}$	72
4.16: Shape comparison for steady bubbles rising in 75 wt% glycerol water solution with various concentration (below CMC) of AOT in a square channel with $D_H=10\text{mm}$	72
4.17: The terminal velocity as a function of bubble size for bubbles rising in 75 wt% glycerol water solution with various concentration (below CMC) of TX-100 in 10mm × 10 mm square channel.	73
4.18: The terminal velocity as a function of bubble size for bubbles rising in 75 wt% glycerol water solution with various concentration (below CMC) of TX-100 in a 15 mm square channel.....	73
4.19: The terminal velocity as a function of bubble size for bubbles rising in 75 wt% glycerol water solution with various concentration (below CMC) of TX-100 in 16mm × 3 mm rectangular channel.....	74
4.20: Schematic of the flow pattern around a bubble rising in a rectangular channel with width w and depth t	76
4.21: Comparison of deformation parameter for steady bubbles rising in 75 wt% glycerol water solution with various concentration (below CMC) of TX-100 in a 16mm × 3mm rectangular channel.	77

4.22: Shape comparison for steady bubbles rising in 75 wt% glycerol water solution with various concentration (below CMC) of TX-100 in a 16mm × 3mm rectangular channel.	77
4.23: The terminal velocity as a function of bubble size for bubble rising in 75 wt% glycerol water solution with 10 ppm Triton X-100 in a circular tube (1-TG-e) and square channel (2-TG-e) with $D_H=10$ mm.	78
4.24: The bubble shapes corresponding to different bubble terminal velocity as a function of bubble size for 75 wt% glycerol water with 10 ppm of TX-100 in a circular tube (1-TG-e) and square channel (2-TG-e) with $D_H=10$ mm.	78
4.25: Schematic of surfactant concentration above CMC	79
4.26: The terminal velocity as a function of bubble size for bubbles rising in 75 wt% glycerol water solution with various concentration (below CMC) of TX-100 in 10mm × 10 mm square channel.	82
4.27: Comparison of deformation parameter for steady bubbles rising in 75 wt% glycerol water solution with various concentration (below CMC) of TX-100 in a square channel with $D_H=10$ mm.	82
4.28: The bubble shapes corresponding to different bubble terminal velocity as a function of bubble size for 75 wt% glycerol water with 10 ppm of TX-100 in a square channel with $D_H=10$ mm.	83
4.29: The terminal velocity as a function of bubble size for bubble rising in 75 wt% glycerol water solution with various concentration of TX-100 in 15mm × 15 mm square channel.	83
4.30: The terminal velocity as a function of bubble size for bubble rising in 75 wt% glycerol water solution with various concentration of TX-100 in a 16mm × 3 mm rectangular channel.	84
4.31: Comparison of deformation parameter for steady bubbles rising in 75 wt% glycerol water solution with various concentration (below CMC) of TX-100 in a 16×3 rectangular channel.	85
4.32: Shape comparison for steady bubbles rising in 75 wt% glycerol water solution with various concentration (around CMC) of TX-100 in a 16×3 rectangular channel.	85
4.33: Shapes and dimensional terminal velocity of steady bubbles as a function of dimensionless bubble size for bubble rising in 2 wt% carboxymethyl cellulose solution in 10×10mm square channel (2-C). The open symbols correspond to the bubbles presented in the figure.	87
4.34: Dimensionless terminal velocity of steady bubbles as a function of dimensionless bubble size for bubble rising in 2 wt% carboxymethyl cellulose solution in 10×10 mm	

square channel (2-C). The open symbols correspond to the bubble shapes presented in Figure 4.34.....	88
4.35: The dimensionless bubble width as a function of dimensionless bubble length for bubble rising in 2 wt% carboxymethyl cellulose solution in 10×10mm square channel (2-C). The dashed line represents $L = B$ curve. The open symbols correspond to the bubble shapes presented in Figure 4.34.....	90
4.36: Deformation parameter as a function of dimensionless bubble size for bubble rising in 2 wt% carboxymethyl cellulose solution in 10×10 mm square channel (2-C). The open symbols correspond to the bubble shapes presented in Figure 4.34.....	90
4.37: The dimensionless film thickness as a function of dimensionless bubble size for bubble rising in 2 wt% carboxymethyl cellulose solution in 10×10mm square channel (2-C). The open symbols correspond to the bubble shapes presented in Figure 4.34.....	91
4.38: Comparison of dimensional terminal velocity of steady bubbles as a function of dimensionless bubble size for bubble rising in 0.1 wt% polyacrylamide solution and 0.3 wt% polyacrylamide solution in 10×10mm square channel, respectively.....	93
4.39: Shape comparison for bubble rising in 0.1 wt% polyacrylamide solution and 0.3 wt% polyacrylamide solution in 10×10mm square channel, respectively.....	93
4.40: Deformation parameter as a function of dimensionless bubble size for bubbles rising in 0.1 wt% polyacrylamide solution (2-P) and 0.3 wt% polyacrylamide solution (2-PP) in 10×10mm square channel.	94
4.41: Dimensionless film thickness as a function of dimensionless bubble size for bubbles rising in 0.1 wt% polyacrylamide solution (2-P) and 0.3 wt% polyacrylamide solution (2-PP) in 10×10mm square channel.....	94
4.42: The terminal velocity as a function of bubble size for bubbles rising in 2 wt% carboxymethyl cellulose solution with various concentration (below CMC) of TX-100 in a 10mm ×10 mm square channel.....	97
4.43: Shape comparison for bubbles rising in 2 wt% carboxymethyl cellulose solution with various concentration (below CMC) of TX-100 in a 10mm ×10 mm square channel.	98
4.44: Dimensionless film thickness as a function of bubble size for bubbles rising in 2 wt% carboxymethyl cellulose solution with various concentration (below CMC) of TX-100 in a 10mm ×10 mm square channel.....	98
4.45: The terminal velocity as a function of bubble size for bubble rising in 2 wt% carboxymethyl cellulose solution with various concentration of Tergitol in a 16mm × 3 mm rectangular channel.....	99

4.46: The terminal velocity as a function of bubble size for bubbles rising in 0.1 wt% polyacrylamide solution with various concentration (below CMC) of TX-100 in a 10mm ×10 mm square channel.	100
4.47: The terminal velocity as a function of bubble size for bubble rising in 2 wt% carboxymethyl cellulose solution with 10 ppm Triton X-100 in a circular tube (1-TC-e) and square channel (2-TC-e) with $D_H=10$ mm.	101
4.48: The bubble shapes corresponding to different bubble terminal velocity as a function of bubble size for 2 wt% carboxymethy cellulose water solution with 1000 ppm of Tergitol in 10mm circular tube and 10 × 10 mm square channel.	102
4.49: Shape comparison for bubbles rising in 2 wt% carboxymethy cellulose solution with various concentration of Tergitol in 10mm ×10 mm square channel.	103
4.50: Shape comparison for bubbles rising in 2 wt% carboxymethy cellulose solution with various concentration of TX-100 in 15 mm × 15 mm square channel.	103
4.51: The bubble shapes corresponding to different bubble terminal velocity as a function of bubble size for 2 wt% carboxymethy cellulose solution with various concentration of Triton X-100 in 16mm × 3 mm rectangular channel.	104
4.52: The bubble shapes corresponding to different bubble terminal velocity as a function of bubble size for 2 wt% carboxymethy cellulose solution with various concentration of Tergitol in 16mm × 3 mm square channel.	104
4.53: The terminal velocity as a function of bubble size for bubbles rising in 0.1 wt% polyacrylamide solution with various concentration of TX-100 in a 10mm ×10 mm square channel.	106
4.54: Shape comparison for bubble rising in 0.1 wt% polyacrylamide solution in 10×10mm square channel.	106
4.55: The terminal velocity as a function of bubble size for bubble rising in 2 wt% carboxymethy cellulose solution with various concentration of Tergitol in 10mm × 10 mm square channel.	107
4.56: The terminal velocity as a function of bubble size for bubble rising in 2 wt% carboxymethy cellulose solution with various concentration of Triton X-100 in 16mm × 3 mm rectangular channel.	108
4.57: The terminal velocity as a function of bubble size for bubble rising in 2 wt% carboxymethy cellulose solution with various concentration of Tergitol in 16mm × 3 mm rectangular channel.	108

ABSTRACT

BUOYANCY-DRIVEN MOTION OF BUBBLES IN THE PRESENCE OF SOLUBLE SURFACTANTS

by

Weihua LI

University of New Hampshire, September, 2011

We present our experimental results for the effect of bulk-soluble surfactants on the buoyancy-driven motion of an air bubble rising in circular, square and rectangular channels filled with a liquid. The bulk fluid is either Newtonian or viscoelastic with or without surfactants. In a Newtonian fluid, small bubbles are nearly spherical travelling with a velocity much lower than the Hadamard-Rybczynski velocity. Long bubbles were prolate translating with a velocity independent of the bubble size. Cusps form in all the viscoelastic systems studied. Even in the presence of small amounts of surfactants bubble shapes were elongated and mobility is reduced due to Marangoni effects. At surfactant concentrations above CMC small bubbles are partially remobilized while long bubbles are completely remobilized. The effect of the channel geometry on bubble mobility and deformation are also presented.

Chapter 1

INTRODUCTION

In fluid mechanics, two phase flows are encountered in many natural and industrial processes such as vapor bubbles rising in a pot of boiling water, raindrops falling through air, enhanced oil recovery, inkjet printing, and so on. Knowledge of two-phase flow behavior is important for the optimum design and safe operation of a wide range of industrial systems. A single bubble rising in a liquid is an important first approach to understanding the structure of two-phase flows. For example, the motion of bubbles and drops in confined domains plays a significant role in the field of enhanced oil recovery. On an average, oil recovery by primary depletion and water flooding recovers only about one third of the original oil in the reservoir [48]. Enhanced oil recovery (EOR) techniques are used to increase the recovery of hydrocarbons from various types of petroleum reservoirs. One of the techniques applied in EOR is flooding the reservoir with surfactant solutions. Surfactants can dramatically alter the wettability of the walls and improve the mobility of the oil droplets. Anionic surfactants are widely used in enhanced oil recovery due to their lower adsorption on reservoir rocks as compared to other types of surfactants [13]. Another technique that has been used for many years in enhanced oil recovery is polymer flooding. Polymers can control the mobility of injected water, improve the volumetric sweep efficiency, and reduce channeling and breakthrough. Polymers can also be combined with surfactants and alkali agents to increase the sweep

efficiency of these tertiary recovery floods.

The behavior of a bubble moving in a liquid differs from that of a solid particle, because the bubble shape can change due to the action of hydrodynamic forces. At a fluid-fluid interface, the fluid properties change very rapidly and continuously in the interfacial region but are constant in the bulk of the two fluids. However due to lack of appropriate molecular theories, the interface is modeled as a massless macroscopic surface where the fluid properties are maintained at their bulk values on either side of the interface and change discontinuously at the interface. Moreover, the fluid interface is characterized by an interfacial tension, σ , which may depend on the temperature, pressure, concentration of any impurities, or charges in the system. Physically, the interfacial tension is termed as the net inward force of molecular attraction per unit length experienced by a fluid that minimizes its surface area or as the work done in generating a unit area of the fluid interface. Since the interface is a massless surface with zero volume, the net force acting on the interface must be zero. A force balance at the interface can be written as,

$$(p_{d,tot} - p_{tot})\mathbf{n} + (\boldsymbol{\tau} - \boldsymbol{\tau}_d) \cdot \mathbf{n} + \nabla_s \sigma - \sigma (\nabla \cdot \mathbf{n})\mathbf{n} = \mathbf{0} \quad (1.1)$$

where quantities with the subscript d represent the drop phase, p_{tot} and $\boldsymbol{\tau}$ represent the actual total pressure and the deviatoric stress tensor in the fluids, and \mathbf{n} represents the outward pointing unit normal. Equation (1.1) shows that the total stress undergoes a jump as the interface is crossed. The normal stress jumps by an amount $\sigma (\nabla \cdot \mathbf{n})$, that is interfacial tension multiplied by the curvature of the interface. The tangential stress, on the other hand, jumps by an amount $\nabla_s \sigma$, that is, the gradient in the interfacial tension along the interface. Equation (1.1) is applied at the fluid-fluid interface to determine the

dynamics of drops and bubbles in confined domains. However, the location of the interface is not known *a priori* and is dependent on the state of stress in the fluid, the interfacial tension and the variation of interfacial tension at the interface.

Bubble sizes and shapes play an important role in heat and mass transfer. Bubble volume and shapes also affect the rise velocity and drag coefficient. Bubble dynamics are affected by the presence of surfactants or polymers in the bulk solution. Understanding detailed bubble behavior can thus provide a rational approach for predictive methods and new design approaches in various industrial processes, such as underground transportation of pollutants, enhanced oil recovery, blood flow in capillaries, bioreactors, food processing, and solvent extraction processes. The effect of changing the fluid rheology due to addition of polymers and the effect of surfactants are briefly discussed in the remaining sections and the primary objectives of this study are outlined.

1.1 FLUID RHEOLOGY EFFECT

Newtonian fluids are widely used as suspension bulk liquids as mentioned in the previous paragraph. All gases, low molecular weight liquids and their solutions (for example, water and glycerol) and molten salts behave as Newtonian fluids. In a Newtonian system, the value of viscosity, η , is independent of the shear rate, and it depends only on temperature, pressure, and the chemical composition of the fluid. In reality, most of the fluids we encounter in physical and industrial processes are non-Newtonian, such as polymer solutions and melts, multiphase mixtures (slurries, emulsions, and gas-liquid

dispersions), personal care products (cosmetics), soap solutions, food products (jam, jellies, cheese, yogurt) [10]. These solutions behave in unexpected ways which cannot be described by Newton's law of viscosity. The viscosity of a non-Newtonian fluid is not constant at a given temperature and pressure but depends on other factors such as the rate of shear in the fluid, the apparatus in which the fluid is contained, or even on the previous history of the fluid. A pseudoplastic or shear-thinning fluid shows decreased resistance with increasing stress, that is, the viscosity decreases with increasing shear rate. If the thinning effect is very strong, the fluid is termed plastic. Alternately, a dilatant or shear-thickening fluid shows increased resistance with increasing applied stress [47]. Fluids such as polymer solutions show both viscous and elastic behavior and are termed as viscoelastic fluids. Due to their elastic nature, such fluids are capable of storing energy and hence can exhibit time dependent viscosity.

Viscoelastic fluids exhibit fluid behavior very different from Newtonian fluids such as the Weissenberg effect (rod-climbing), hole-pressure error, and Uebler effects [35]. The Weissenberg effect is one of the most interesting phenomena exhibited by viscoelastic fluids [29]. As shown in Figure 1.1(b), a viscoelastic fluid in a cylindrical vessel will climb up a rotating rod against centrifugal force and gravity; while, a Newtonian liquid will form a hole instead as presented in Figure 1.1(a). Rod-climbing is a second-order effect associated with the inequality of normal stresses in shear flow. It is suggested that the normal stress acts like a hoop around the rod and forces the fluid inwards against the centrifugal force and upwards against the gravitational force [27]. Another interesting effect in two-phase flow of viscoelastic fluids is cusp formation. Liu et al. investigated

the shape of air bubbles rising in a quiescent viscoelastic fluid in the absence of wall effects. In a system that was completely axisymmetric, they observed bubble shapes that exhibited a two-dimensional cusp. In the front view, the bubbles showed a pointed shape as seen in Figure 1.2. In the side view, they reported that the broad edge showed a variety of shapes such as flat like a spade, arched like an axe, pointed like an arrow or flat and tilted like a guillotine as seen in Figure 1.2. It is hard to imagine how such a singularly asymmetric feature could arise in a situation which in every respect suggests that an axisymmetric shape should prevail. The fluids used in this study were shear-thinning and viscoelastic and that affects both the deformation and mobility of the bubbles rising in these fluids [26].

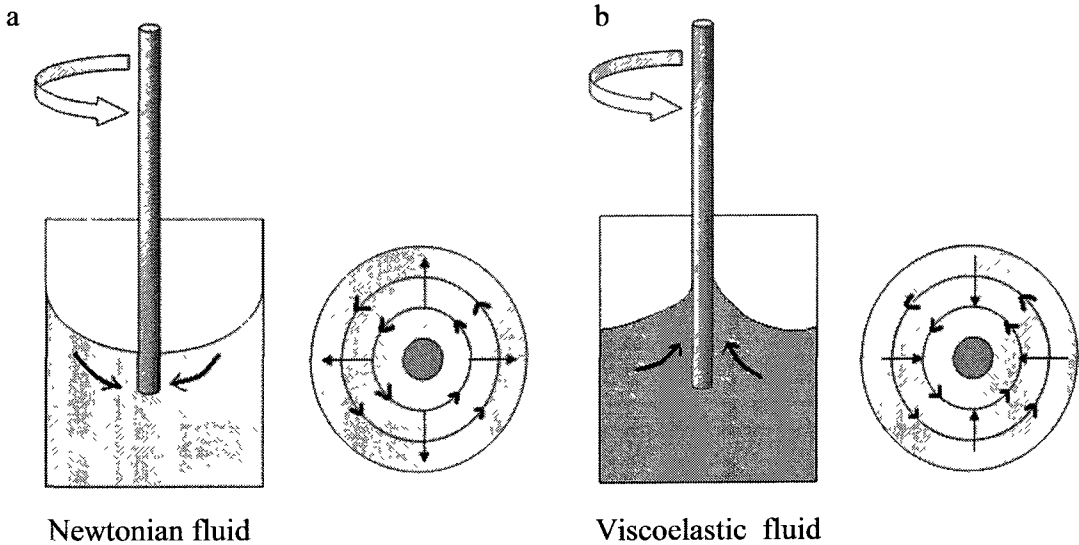


Figure 1.1: Schematic showing the Weissenberg effect (or rod-climbing) in a polymeric fluid.

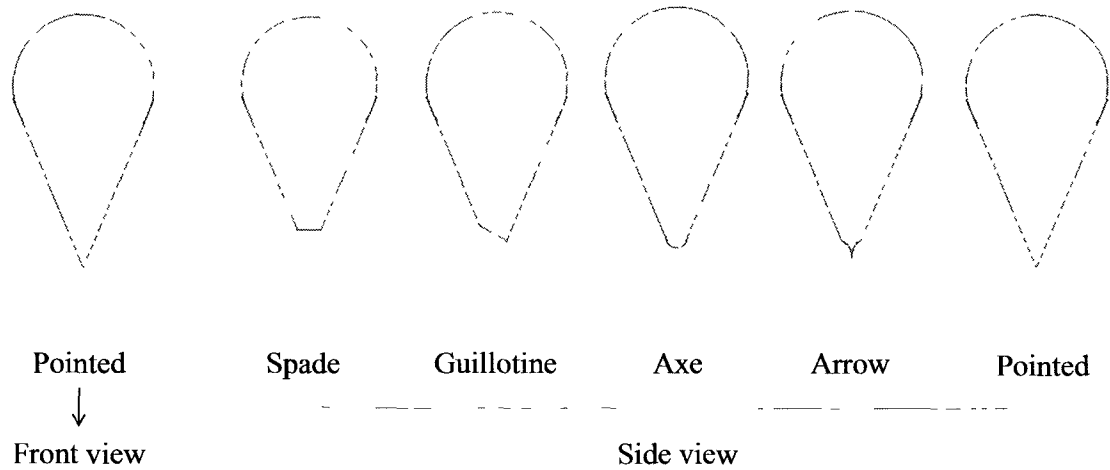


Figure 1.2: Schematic of the two-dimensional cusps seen for bubbles rising in a quiescent viscoelastic fluid as reported by Liu et al. [26].

1.2 SURFACTANT EFFECTS

Surfactants are versatile compounds that can be found in many applications such as food products, motor oils, detergents, and flotation agents used for separation processes. Surfactants are either added as additives or present as impurities which cannot be avoided. Surfactants have an amphipathic structure which consists of a hydrophilic head and a hydrophobic tail. As a result of the special structure, when surfactants are present in a system, they adsorb at the two-phase interface in an oriented way such that the hydrophilic head stays in the aqueous phase while the hydrophobic tail stays away from it as shown in Figure 1.3. This alters the interfacial free energies of these surfaces in a marked way [37]. If an interface with a clean interfacial tension σ_c is created in a surfactant solution and the system is allowed to reach an equilibrium, the concentration of surfactants at the interface reaches an equilibrium value. The equilibrium interfacial

tension, σ_{eq} corresponding to the equilibrium surfactant concentration is less than the clean interfacial tension, σ_c .

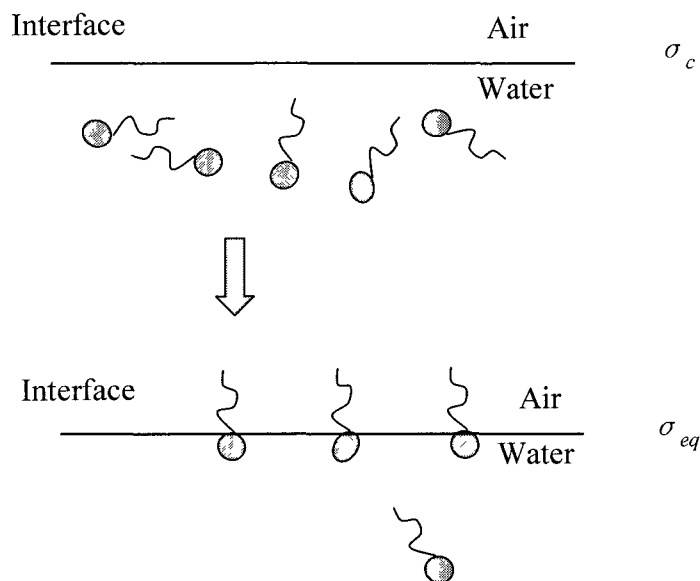


Figure. 1.3: Schematic of equilibrium behavior of surfactant molecules at an air-water interface.

If we conduct the experiment shown in Figure 1.3 for varying bulk concentrations of surfactants, we can obtain the graph for the equilibrium surface tension as a function of bulk surfactant concentration as shown in Figure 1.4. As seen in the figure, the equilibrium surface tension remains a constant for very small amount of surfactants present in the solution. Then, with increasing bulk surfactant concentration, the equilibrium surface tension decreases until it reaches a lower plateau value termed as the critical micelle concentration (CMC) point. Below CMC, surfactants only appear in monomer form while above CMC surfactants start to aggregate and form micelles. The

shapes of micelles could be cylindrical, spherical, vesicular, lamellar, or hexagonal. The interfacial tension values continue to decrease as the bulk surfactant concentration is increased above the apparent CMC values, although the rate is lesser. The CMC value depends on several factors such as the length of the molecule, the nature of the solvent, the concentration of salt, the temperature [30]. In a polymer solution system, however, surface tension is greatly affected by both surfactants and the polymer molecules due to the associative nature of the molecules [33]. The surface tension of polymer–surfactant systems can be divided into three regions depending on their concentrations: a monomer region, a polymer–surfactant complex region, and a micellization region [46].

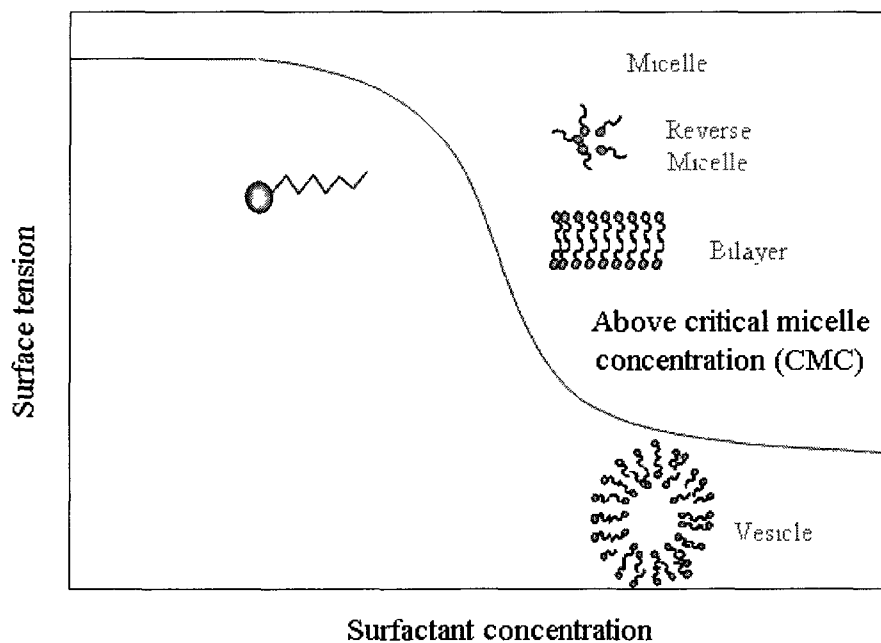


Figure. 1.4: Schematic of equilibrium surface tension as a function of bulk surfactant concentration

For flow around a single bubble rising in a vertical tube filled with surfactant solution, time to reach equilibrium may not be possible. Figure 1.5 shows a schematic of the different timescales at play for the non-equilibrium effects at an interface with surface convection. The bulk concentration is assumed to be less than the critical micellar concentration (CMC) value. The surfactants' non-equilibrium behavior depends on the mass transfer time scale, τ_{MT} and the convection time scale, τ_{conv} at the interface. The surfactant mass transfer timescale, τ_{MT} , depends on the timescale of diffusion of surfactant from the bulk to the sublayer, τ_D and the timescale of adsorption and desorption from the sublayer to the interface, $\tau_{a/d}$. The timescale for convection at the interface depends on the tangential velocity, U_i at the interface. Surface convection leads to accumulation of surfactants at the stagnation points. If $\tau_{MT} \ll \tau_{conv}$, the interface gets replenished with surfactants very quickly and the surface tension of the interface reduces

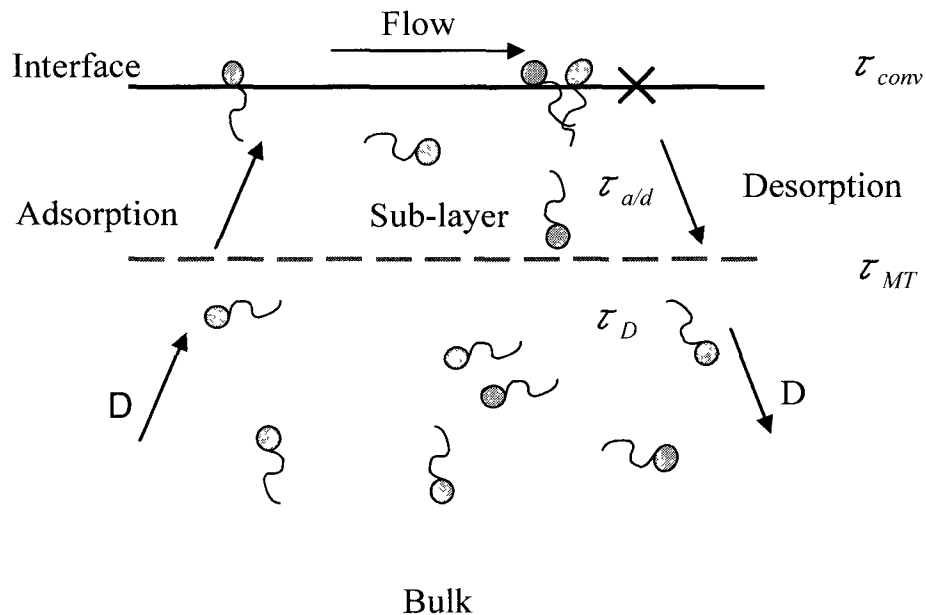


Figure. 1.5: Schematic of non-equilibrium behavior of surfactant molecules at interface.

to a uniform equilibrium surface tension corresponding to the bulk concentration. If $\tau_{MT} \gg \tau_{conv}$, the mass transfer of surfactant to the interface is inhibited and the surfactant may be considered insoluble. If $\tau_{MT} \sim \tau_{conv}$, the relative magnitudes of $\tau_{a/d}$ and τ_D determines the behavior of the interface. For example, in the adsorption-desorption limit, $\tau_{a/d} \gg \tau_D$, and the sublayer concentration is equal to the bulk surfactant concentration while in the diffusion-controlled limit, $\tau_{a/d} \ll \tau_D$. The same surfactant system may exhibit different behavior depending on the surfactant concentration and the type of flow.

1.3 OBJECTIVES

The dynamics of a single bubble in a confined system can help us understand the dynamics of two-phase flows in complex geometries. Several two-phase flow applications of interest involve complex geometries with fluids that exhibit non-Newtonian behavior and may require the presence of surfactants. Here we focus on conducting a systematic experimental study on the buoyancy-driven motion of bubbles rising through vertical channels. The goal of this thesis is to investigate the effects of

- shape of confining wall,
- fluid rheology, and
- presence of surfactants

on the deformation and mobility of bubbles. In Chapter 2, we discuss existing studies on the effects of confinement, elasticity, and surfactants on bubble dynamics. In Chapter 3, we describe our experimental set up, systems studied, and analysis conducted. In Chapter

4 we summarize the experimental results of this study. We conclude with a summary of this work and future recommendations in Chapter 5.

Chapter 2

BACKGROUND

The motion of bubbles in confined domains is encountered in a variety of natural phenomena and technical applications. It also remains a problem of considerable fundamental importance as a pore-scale model for studying the dynamics of two-phase flow through porous media. Therefore, extensive theoretical and experimental research dealing with motion of bubbles or drops in Newtonian and non-Newtonian fluids in the presence or absence of surfactants has been conducted. However, a large number of these studies are restricted to bubble dynamics in the absence of wall effects or long bubbles in cylindrical tubes.

2.1 DROPS RISING IN NEWTONIAN FLUID

2.1.1 Unbounded Flows

The rise of a single gas bubble in an unbounded quiescent flow has been studied since 1911 [16, 38]. The well-known Hadamard–Rybczynski equation describes the terminal velocity of slowly moving spherical bubble through an unbounded fluid which is shown in Equation 2.1. From this equation we can see that the terminal velocity of a single freely rising bubble in a quiescent flow is dependent on the radius of the bubble R , the gravitational acceleration g , the density of the bubble ρ_d , the density of

the ambient fluid ρ_o , the viscosity of the ambient fluid η^o . The equation is valid for a spherical bubble at very low Reynolds number.

$$U_l = R^2 g(\rho_o - \rho_d) / 3\eta^o \quad (2.1)$$

2.1.2 Flow in Cylindrical Tubes

The general shape of a Taylor bubble is a bubble whose length is several times the tube diameter and whose leading edge is rounded. The trailing edge can take on either a rounded, indented, or unsteady shape depending upon the flow conditions and fluid properties. There has been extensive research about Taylor bubbles in Newtonian fluids. Taylor [44] measured the amount of fluid left behind when a viscous Newtonian liquid was blown from an open-ended horizontal tube. He concluded that the film thickness was a monotonic increasing function of the capillary number, $Ca \equiv \eta U_d / \sigma$, where η is viscosity, U_d is bubble velocity, and σ is the surface tension. Bretherton [7] was perhaps among the first to perform a detailed theoretical analysis of the movement of long Taylor bubbles in vertical circular tubes in a Newtonian system. He demonstrated that the free rise of a long bubble was completely inhibited if Bond number was less than 0.842, the midsection of a rising bubble which had a uniform liquid film thickness increases with increasing bubble volume, and the shapes of the front and rear of the long bubbles remain the same for various bubble volumes.

Polonsky et al. [32] performed experimental research on the relationship between buoyancy driven motion of a Taylor bubble rising in water and the velocity field ahead of

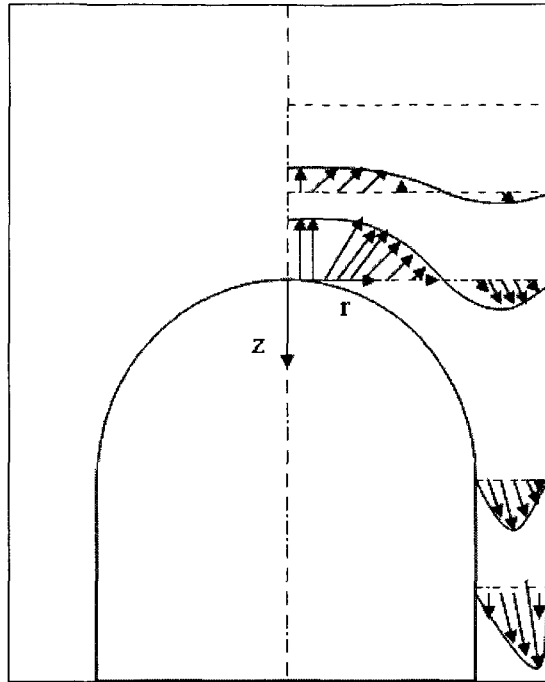


Figure 2.1: Schematic of the velocity field near the leading edge of a Taylor bubble rising in a stagnant fluid.

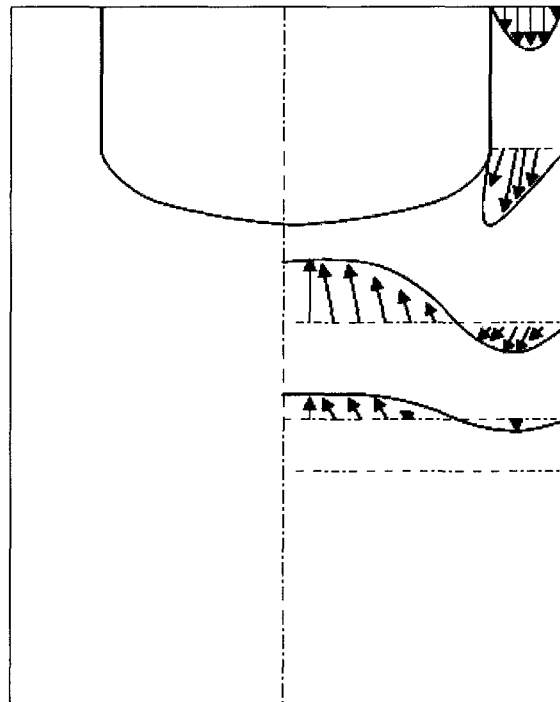


Figure. 2.2: Schematic of the velocity field in the wake of a Taylor bubble rising in a stagnant fluid.

it. They found that the propagation velocity of the bubble was related to the maximum local liquid velocity ahead of it. Bugg and Saad [8] produced the velocity profile around a rising Taylor bubble in olive oil by particle image velocimetry (PIV) method, which is schematically shown in Figures 2.1 and 2.2. From the figures we can see that the outside fluid diverges at the leading end of the bubble and converges at the trailing end of the bubble. Bugg and Saad also found that the velocities in the liquid reduced to less than 5% of the bubble speed at $D/3$ ahead of the bubble, D being the tube diameter. The velocity dropped to 10% of the bubble speed at about $0.77D$ below the bubble due to the influence of the wake.

Feng [14] numerically studied the buoyancy-driven motion of a long gas bubble through viscous liquid in a round tube. He concluded that the terminal velocity of long bubbles was independent of bubble volume. Moreover, he showed that the surface profiles of long bubbles exhibited a prolate nose-like shape and various tail shapes were obtained by adjusting the values of Reynolds and Weber numbers. Borhan and Pallinti [6] experimentally and numerically investigated buoyancy-driven motion of viscous drops through cylindrical capillaries at small Reynolds numbers. They found that the retarding effect of the capillary wall decreased as the buoyancy force became more dominant compared to surface tension, or as the drop fluid became less viscous relative to the suspending fluid. However, for a given viscosity ratio and beyond a certain limiting value of the Bond number, the wall effect remained unchanged with increase of Bond number. The thickness of the liquid film surrounding large drops was insensitive to the value of the viscosity ratio.

2.1.3 Flow in Non-circular Tubes

All study of motion of bubbles in non-circular channels, to date, arose due to its relevance to very slow two-phase flow in channels of microscopic dimensions. This flow is similar to the flow within the porous rock of an oil reservoir where typically the driven fluid is significantly more viscous than the driver. In enhanced oil recovery applications the film thickness is a direct measure of the fraction of oil that can be recovered by flooding techniques. However, circular capillaries serve as poor models for flow in porous media. Non-circular capillaries provide a better model for describing the irregular and angular nature of porous media [19].

Kolb and Cerro [19] numerically presented results for the two phase flow in a capillary of square cross section. They reported that the transition from a nonaxisymmetric to axisymmetric bubble was found to occur at $Ca \approx 0.1$ [20]. Clanet et al. [11] studied the buoyancy driven motion of long bubbles in vertical tubes of different cross-sections (rectangles, regular polygons, toroidal tubes) filled with Newtonian fluids. They showed that the velocity in high-Reynolds-number domain was characterized by $U_b = (8\pi)^{-1/2}(gP)^{1/2}$, and the low-Reynolds number range by $U_b \approx 0.012gS/\nu$, where P and S stand for the wetted perimeter and the area of the normal cross-section of the tube respectively. Recently, Li et al. [23] studied the buoyancy-driven motion of air bubbles in Newtonian fluids in square capillaries (10mm×10mm and 15mm×15mm) over a range of Reynolds numbers, where wall effects cannot be neglected. This study proposed a relationship between the Weber number, $We = \rho U_T^2 R_c / \sigma$ and important flow parameters

such as bubble velocity, bubble deformation, and film thickness. This complex behavior also clearly indicated that the walls had a significant retarding effect on the bubble motion. Most of their experimental results were numerically confirmed by Amaya-Bower and Lee [1].

Several investigations were done on miniature non-circular tubes. Bi and Zhao investigated the motion of Taylor bubbles in miniature circular and noncircular channels with stagnant water. They found that in large circular tubes ($d > 2.9$ mm), bubbles rose up periodically. As the diameter of the circular tubes became smaller, the up-motion of the gas slugs was slowed down, and ceased completely when the tube size was sufficiently reduced ($d \leq 2.9$ mm). For the miniature triangular channels, however, it was found that the gas slug always rose upward even though the hydraulic diameter was as small as 0.866 mm due to buoyancy force. Similarly, they found that the drift velocity in the square and rectangular channels is not zero [5]. Later, Liao and Zhao presented a theoretical model that predicts the drift velocity of a Taylor bubble in vertical mini triangular and square channels filled with a stagnant liquid. They found that the drift velocities in the triangular channel are substantially higher than those in the square channel having the same hydraulic diameter [24]. Yue et al. [49] investigated flow and mass transfer properties under air–water Taylor flow in horizontal square microchannels. They found that Taylor bubble moves slightly faster than the liquid slug due to the existence of a nearly stagnant film surrounding the bubble body. The experimental bubble velocity results can be well interpreted based upon an approximate measurement of the liquid film profile in microchannels, where it was shown that the velocity ratio

between Taylor bubble and the liquid slug further increased with increasing Ca primarily as a result of the thickening of the liquid film in the corner of the microchannel cross-section.

2.2 FLUID RHEOLOGY EFFECT

2.2.1 Unbounded Flows

Astarita and Apuzzo [2] experimentally presented data on the rising gas bubbles in a variety of non-Newtonian liquids. For small bubbles, the velocity-volume curve in the highly elastic liquids showed a striking peculiarity: a critical volume exists corresponding to an abrupt increase in the velocity. They speculated that it may be due to a transition from the Stokes to the Hadamard regime and that viscoelasticity is responsible for the abruptness of the velocity transition. A gas bubble moves in the Stokes regime when the liquid is in creeping flow, the bubble is spherical, and the interface is rigid. However, a gas bubble moves in Hadamard regime when the liquid is in creeping flow, the bubble is spherical, and the interface is free. Liu et al. [26] also confirmed the velocity jump when an air bubble rose in a viscoelastic fluid beyond a critical capillary number, which they believed was due to the reduction in the drag and effects of surfactants. Rodrigue et al. [35] examined the motion of a freely rising gas bubble in non-Newtonian fluids to determine the conditions for the possible existence of a discontinuity in the bubble velocity-bubble volume log-log plot. They proposed that the discontinuity results as a balance between elastic and Marangoni instabilities.

Liu et al. [26] also reported that after a critical capillary number, cusp formed in the viscoelastic fluid. The cusped tail is basically two-dimensional with a broad edge in one view and a sharp cusped edge in the orthogonal view. Cusp formation would appear in Newtonian liquids only when the column was tilted, and no cusp was seen for free rising bubbles. The two-dimensional cusp of rising air bubbles appeared to depend on the fluid and the bubble volume, and was independent of the size or shape of the bubble column. Shapes of rising bubble in viscous Newtonian fluids went from spherical to oblate spherical to that of a spherical cap. However, bubble shapes in many viscoelastic fluids ranged from spherical to prolate spherical to that with a trailing cusp. Belmonte [3] also observed the cusp formation but for the motion of a bubble rising in a micellar non-Newtonian system.

The flow field around air bubbles rising in aqueous polyacrylamide solutions and the viscoelastic and wall effects on the bubble mobility and velocity jump was considered by Herrera-Velarde et al [17]. The flow configuration changed drastically below and above the critical bubble volume. Negative wake appeared behind the bubble above the critical volume. Additionally, the container walls significantly affected the magnitude of the terminal velocity as well as the velocity jump. However, the critical volume at which the velocity jump appeared did not change for different container sizes. They believed the velocity jump was mainly due to the formation of negative wake. Lind and Phillips [25] investigated numerically the role of viscoelasticity on the dynamics of a rising gas bubble. They also reported that the negative wake was primarily responsible for the velocity jump discontinuity.

2.2.2 Flow in Cylindrical Tubes

There are very limited studies on the motion of bubbles in confined domains filled with viscoelastic fluids and are restricted to cylindrical capillaries. Recently, Sousa et al. have used simultaneous PIV and shadowgraphy techniques to study the shape and flow fields around a Taylor bubble rising in a cylindrical tube filled with non-Newtonian fluids. They conducted experiments with carboxymethyl cellulose solutions and polyacrylamide solutions of varying concentrations. The shape of Taylor bubbles was prolate spheroid at the leading edge with higher curvatures for higher viscosity fluids. The bubble radius increased and reached a maximum value at certain distance from the nose of the bubble. For higher concentrations of carboxymethyl cellulose solutions (> 0.8 wt%) which exhibit viscoelastic fluid behavior, the bubbles show a two-dimensional cusp at the rear of the bubble and a negative wake. In case of polyacrylamide solutions, the authors found that flow field behind the bubbles was not always axisymmetric and showed a negative wake at higher concentrations ([41], [42], [43]).

2.3 SURFACTANT EFFECTS

2.3.1 Unbounded Flows

Frumkin [15] & Levich [22] were among the first to describe the mechanism by which surfactants modify the velocity field in the vicinity of a fluid-fluid interface. They pointed out that surfactants tend to be convected along the bubble surface and accumulate at the rear part of the bubble. The nonuniform surfactants distribution results in

nonuniform surface tensions, which cause Marangoni stresses that retard the surface mobility. Chen and Stebe [9] confirmed Frumkin and Levich's theory about Marangoni retarding effects and further thoroughly explained the mechanism of remobilizing surfactant-retarded fluid particle interface by adjusting surfactant concentration. They established that a surfactant with fast sorption kinetics at concentrations above CMC can be used to control surface mobility. Later, Stebe and Maldarelli [40] demonstrated that this mechanism is effective even with the presence of surface retarding surfactants by adding sufficient remobilizing surfactant. The theoretical progress has identified three regimes of surfactant transport, which are the stagnant cap regime, uniformly retarded regime, and remobilization regime. In the stagnant cap regime, the maximum rate of either the diffusive or kinetic fluxes of surfactant to the surface is much smaller than surface convection. As a result, adsorbed surfactant behaves as if it were insoluble, and is swept to the back end of the particle. In the uniformly retarded regime, the rate of bulk diffusion and surfactant kinetic exchange are of the same order as the interfacial convection, surfactant exchanges between the bulk and the surface. In the remobilization regime, the bulk concentration of surfactant is large. The kinetic and bulk diffusive exchange are fast relative to convection. The difference between the bulk and sublayer concentrations becomes small [31].

Some experimental results have been reported for the case of a bubble rising in unbounded Newtonian or non-Newtonian fluid with the presence of surfactants. Rodrigue et al. [34] investigated the motion of free rising spherical gas bubbles in three Newtonian and eight non-Newtonian polymeric liquids in the presence of surfactants

(SDS). They showed that the surfactant had an effect on the velocity of the bubbles in both Newtonian and non-Newtonian fluids. As the viscosity of the liquid increased, the effect of surfactant was less pronounced in Newtonian systems. A jump discontinuity in the case of viscoelastic fluids was observed which they believe was due to the change of the ratio of elastic to surface tension forces. Later, they calculated the drag force experienced by free rising bubbles in an inelastic shear-thinning fluid in the presence of SDS [36]. They detected no variation in the viscosity curve with or without surfactants. They found that the presence of contamination increased the drag resulting in a decrease of the rise velocity. Inversely, the effect of shear thinning was to decrease the drag, thus leading to a balance between both effects.

Tomiyama et al. [45] investigated the terminal velocity of a single distorted bubble in distilled water and in water contaminated with surfactants in the surface tension force dominant regime experimentally. They confirmed that bubble motion, shape and velocity were markedly sensitive to initial shape. The primary role of surfactants in this regime was to cause the damping of bubble shape oscillation, by which a contaminated bubble behaved as if it were a clean bubble with low initial shape deformation. Saito et al. [39] examined the non-equilibrium effects of surfactants in water solution. Although the bulk equilibrium surface tension was almost the same as that of purified water, the bubble motion and the surrounding liquid motion in the solutions were very different from those in purified water which they believed was due to Marangoni stress. They found a critical concentration of a surfactant at which, the intensity and size of the vorticity around the bubble became the largest. Zhang et al. [51] numerically simulated a free rising bubble

in aqueous surfactant solutions assuming the stagnant cap model and applying different mass transfer control steps. They found that the stagnant cap model and boundary layer mass transfer control were valid for Triton X-100 adsorption onto a rising 0.8 mm diameter bubble by comparing the simulated velocity profiles with the experimental ones.

2.3.2 Flow in Cylindrical Tubes

Several experimental results have also been presented for the case of a bubble rising in confined domains filled with either a Newtonian or a non-Newtonian fluid in the presence of surfactants. Krzan et al. [21] performed experiments to determine the local and the terminal velocities, the size and the degree of bubbles' shape deformations as a function of distance from the position of the bubble formation (capillary orifice) in a water-surfactant system. They found that the bubbles accelerated rapidly and deformed immediately after detachment from the capillary. After the acceleration period the bubbles either attained a constant value of the terminal velocity (distilled water and high concentrations of surfactant), or a maximum in the velocity profiles was observed (low concentrations of surfactant). The values of the terminal velocity diminished drastically with increasing surfactant concentration. Rodrigue et al. [8] observed a velocity discontinuity as a function of volume ($0.1\text{--}10\text{ cm}^3$) for air bubbles using a 0.5 wt% polyacrylamide solution in a 20/80 glycerin/water mixture when smaller volumes are used. They reported that for concentrations of SDS above CMC, polymer-surfactant association can remobilize surface velocity and eliminate velocity discontinuity.

Dynamics of bubbles in the presence of surfactants has also been studied numerically. Cuenot et al. [12] presented a numerical study of the effects of slightly soluble surfactants on the flow around a spherical bubble for a Reynolds number $Re=100$. They confirmed that the surfactants tend to slow down the flow at the rear of the bubble, leading to a dramatic increase of the drag coefficient. Zhang and Finch [50] addressed measurement of single bubble velocity in surfactant solutions (far below CMC). They reported that the bubble generation technique may influence the distance to reach a steady-state velocity. In their studies, the same steady state velocity was reached regardless of surfactant concentration which they suggested that the stagnant cap angle on the bubble was the same at steady state and was not a function of concentration. Johnson and Borhan [18] investigated the effect of bulk-soluble surfactants on the dynamics of a drop translating through a cylindrical tube under low-Reynolds-number conditions. They reported that as the equilibrium surface coverage was increased, the mechanism by which drop mobility was reduced changed from uniform retardation at low surface coverage to the formation of a stagnant cap at high surface coverage.

In many industrial applications bubbles move in confined spaces, for example in the fuel bundles of the core of nuclear reactors, pressurizer components, steam generators and so on. The effect of the presence of a wall on the motion of bubbles has been studied before. However, a majority of these studies are either confined to larger tube sizes where wall effects are negligible or to very long bubbles in cylindrical tubes. Only a few of the studies have been reported on small diameter channels of non-circular cross section or with bubble sizes comparable to the channel size. Our experiments cover the whole

range of bubble sizes from small spherical bubbles to large elongated ones. Finally, while abundant experimental data are available in the literature for the buoyancy-driven motion of air bubbles in various suspending fluids in various channel geometries, the corresponding experimental information for the same case in the presence of surfactants is scarce.

Chapter 3

EXPERIMENTAL METHODS

The goal of this thesis is to determine the effect of soluble surfactants on the buoyancy-driven dynamics of air bubbles in confined domains. The effect of surfactant concentration, fluid rheology, and the shape of the confining wall on the bubble deformation and mobility at steady state were studied. The experimental set up, the materials and their properties as well as the analysis techniques used to conduct this study are described in the following sections.

3.1 EXPERIMENTAL SET-UP

The schematic of experimental setup used to conduct this research is shown in Figure 3.1 and described briefly here. The experimental set up consisted of an acrylic tube positioned vertically in front of a monochrome CMOS digital video camera (PixeLink PL-A741 with a maximum speed of 27 frames per second at a resolution of 1280×1024). A fiberglass light source provided uniform back-illumination to capture the images of the bubbles. The digital video camera was connected to a personal computer over a FireWire (IEEE-1394) interface and the software PixeLINK Capture OEM is used to control the camera and capture a video of the rising drop / bubble. Vision Assistant software from

National Instruments was used to obtain and analyze individual frames from the recorded movie.

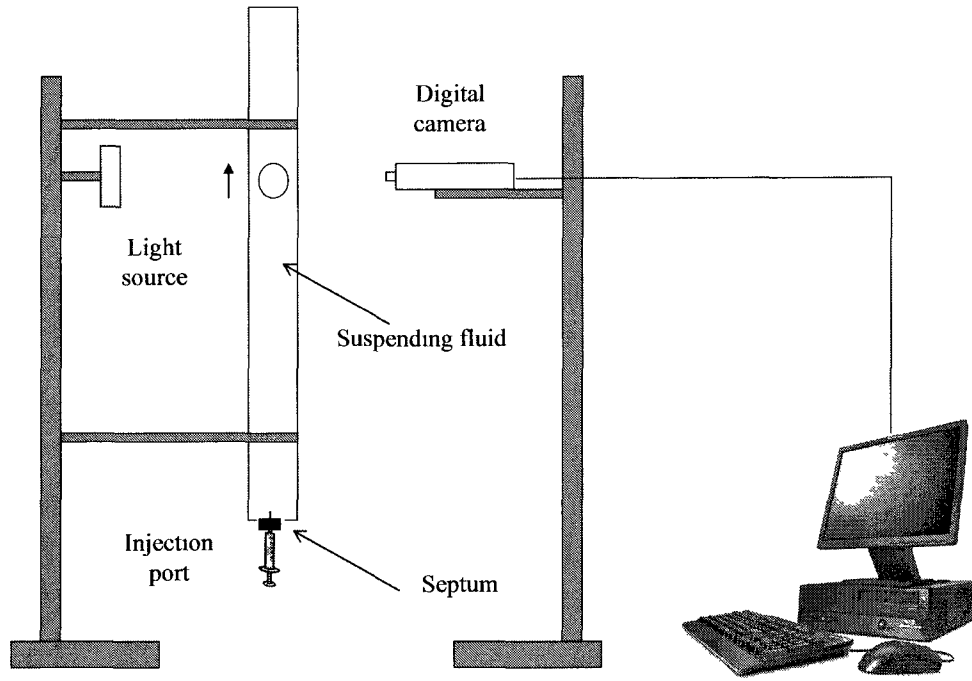


Figure 3.1: Schematic of the experimental setup used to study the buoyancy-driven motion of bubbles in channels.

Table 3.1: Channel geometries considered for studying dynamics of drops and bubbles rising in a channel filled with an immiscible fluid.

Number	Geometry	Dimensions	Hydraulic Diameter, D_H
1	Circular	Diameter, $D = 10$ mm Length = 813 mm	10 mm
2	Square	Width, $h = 10$ mm Length = 927 mm	10 mm
3	Square	Width, $h = 15$ mm Length = 950 mm	15 mm
4	Rectangular	Width, $h = 16$ mm Depth, $t = 3$ mm Length = 1232 mm	5.1 mm
5	Rectangular	Width, $h = 32$ mm Depth, $t = 3$ mm Length = 1232 mm	5.5 mm

Channels with various cross sectional geometries were used to study the dynamics of drops and bubbles over a large range of parameters and are shown in Table 3.1. The channels were made of acrylic plastic sheet purchased from TAP Plastics. Channels with square and circular cross-sections, namely, tubes 1, 2, and 3 were obtained directly from TAP Plastics. Channels with rectangular cross-sections, namely, tubes 4 and 5 were fabricated from acrylic plastic sheets (3 mm thick). The circular tube, tube number 1, was enclosed inside a 15 mm square channel filled with the corresponding suspending fluid to remove optical distortion. The length of each channel was at least thirty times its hydraulic diameter. The bottom end of each channel was sealed with an acrylic end fitted with a 11 mm diameter rubber septum (RESTEK) to serve as the injection port.

3.2 MATERIALS AND CHEMICALS

The channels were filled with a suspending fluid of either a Newtonian or non-Newtonian rheology. The Newtonian suspending fluids used in these experiments consisted of solutions of glycerol (Aldrich) in ultrapure water (Millipore Direct-Q 3 UV with resistivity of 18.2 M Ω -cm). The Newtonian fluid used was 75 wt% glycerol water solution. The non-Newtonian suspending fluids used in these experiments were prepared by mixing carboxymethyl cellulose (SIGMA-ALDRICH) or polyacrylamide (SNF) powder in ultrapure water. The three different non-Newtonian solutions studied were 2 wt% carboxymethyl cellulose solution, 0.1 wt% polyacrylamide solution, and 0.3 wt% polyacrylamide solution. Air was used as the drop fluid. Several surfactants at varying concentrations were dissolved in the suspending phase to study the effect of surfactants

on the dynamics of bubbles. In this study we used water soluble nonionic surfactants, Triton X-100 (Alfa Aesar) and Tergitol 15-S-9 (SIGMA) and water soluble ionic surfactants, Aerosol-OT (EM SCIENCE) and sodium dodecyl sulfate (EMD). The physical properties of the various chemical compounds used in the experiments are shown in Table 3.2. All solutions were prepared on per weight basis. The volume of solution needed for the experiment was determined. The required amount of the reagent, glycerol, carboxymethyl cellulose, or polyacrylamide was weighed and added to the measured amount of ultrapure water. After adding the reagent, the solution was stirred in a closed vessel for two days to ensure uniformity.

3.3 OPERATING PROCEDUR

The required amount of surfactant, reagent (glycerol or Carboxymethyl cellulose) were weighted and added to the measured volume of Millipore-Q water. Newtonian suspending fluids used in the thesis were mixed for 24 hours in a covered beaker to prevent evaporation and were placed in a vacuum degasser to remove any air bubbles from the fluid before use. Non-Newtonian fluids were mixed for at least 48 hours in a covered beaker and were degassed before use. Surfactant solutions were prepared at the highest studied concentrations as adding small amounts of surfactants to the suspending phase was difficult. To do this, the desired amount of surfactant was added to the well mixed suspending phase and allowed to mix for 24 hours in a covered beaker. The concentrated surfactant solution was then diluted with the suspending phase to obtain the required concentration. Early experiments showed that if the channels were not

pretreated, surfactants were lost during the experiment due to adsorption to the channel wall. Therefore, before each experiment, the channel was

Table 3.2: Properties of the chemicals used in the experiments for studying dynamics of drops and bubbles rising in a channel filled with an immiscible fluid.

Fluids/Materials	Properties
Bulk phase	
Glycerol	Physical State: colorless, odorless, viscous liquid Chemical Formula: $C_3H_8O_3$ Molecular Weight: 92 Density: 1260kg/m^3
Carboxymethyl cellulose	Physical State: white powder Chemical Formula: $(R_3O_4)_n$ (R=H or CH_2CO_2H) Molecular Weight: variable Density: variable
Polyacrylamide	Physical State: white granular powder Chemical Formula: $(C_3H_5NO)_n$ Molecular Weight: variable Density: 1130kg/m^3
Drop phase	
Air	Density: 1.2kg/cm^3
Surfactant	
Triton X-100	Physical State: colorless, viscous liquid Nonionic, water soluble γ_{CMC} (mN/m): 30 Chemical Formula: $C_{14}H_{22}O(C_2H_4O)_n$ (n=9-10) Average Molecular Weight: 647 Density: 1060kg/m^3
Aerosol-OT	Physical State: waxy solid Ionic, water soluble γ_{CMC} (mN/m): 30.8 Chemical Formula: $C_{20}H_{37}O_7NaS$ Average Molecular Weight: 444 Density: 963kg/m^3
Sodium dodecyl sulfate	Physical State: crystals solid Ionic, water soluble γ_{CMC} (mN/m): 40 Chemical Formula: $NaC_{12}H_{25}SO_4$ Average Molecular Weight: 288 Density: 1010kg/m^3
Tergitol 15-S-9	Physical State: pale yellow liquid Nonionic, water soluble γ_{CMC} (mN/m): 30 Chemical Formula: $C_{12-14}H_{25-29}O[CH_2CH_2O]_xH$ Average Molecular Weight: 584 Density: 1006kg/m^3

pretreated by filling them with the experimental suspending fluid at a surfactant concentration well above the CMC for 24 hours. Then the channel was cleaned with warm tap water six times and allowed to sit for 3 hours in between each wash. The process was repeated again with Millipore-Q water six times. The channel was then dried using the air supply in the lab. This ensured that surfactants were already adsorbed to the channel wall before the experiment was conducted and no excess surfactant was present that would desorb into the experimental solution. The surface tension of the experimental solution was also tested before and after the experiment to ensure that the surfactant concentration of the experimental solution did not change during the experiment.

There was no external temperature control for this system and all of the experimental data presented in this paper was collected between 21 and 22 °C. The experimental temperature was determined by a thermocouple placed near the outlet regions of the channel. To conduct the experiment, the dried channel was filled slowly with the suspending fluid to minimize bubble regeneration. Then the channel was clamped to a stand and leveled to ensure that the bubbles remained along the central axis of the channel as they rose through the channel. The channel was placed in front of a monochrome CMOS video camera and the system was allowed to equilibrate thermally before the experiments were conducted. For each run of experiments, the desired volume of the drop fluid was injected at the bottom of the channel using a micrometer syringe, which can be used to roughly measure the volume of the bubble injected. A 3 ml syringe was used to produce bubbles with nominal volumes V (as measured from the syringe)

ranging from 0.1 to 0.5 cm³, and a 5 ml syringe for bubbles with 0.5cm³ <V< 1.2 cm³. The syringe was thoroughly cleaned with warm tap water first and then Millipore-Q water, later dried in air before each new set of experiments. The bubble was injected along the symmetry axis of the channel. The motion of the bubble through the channel was recorded using the CMOS camera. The camera was placed on a leveled tripod high enough from the injection point to capture the steady shape and velocity of the bubbles. The camera was connected to a computer via FireWire (IEEE-1394) interface. The software PixeLINK Capture OEM was used to control the camera and capture the movement of the rising bubble. Exposure Time (ms), Gain, and Frame Rate (fps) were set as 1.5, 8.2, and 20, respectively from the Basic Control menu. Region of Interest was adjusted to get a good image. A ruler was fixed on the channel by tape and a calibration image was captured from the Image Capture menu to be used for calibration later. The Number of Frames was modified and the movement of the bubble was captured from the Video Capture menu. The captured images were analyzed to determine the steady shape and speed of bubbles using image analysis described in Section 3.6.

3.4 FLUID PROPTERTY MEASUREMENT

The viscosities of all the suspending fluids were measured using either the Brookfield cone and plate viscometer (LV DV-III+ with Rheocalc software) or the TA Instruments oscillatory rheometer (AR-550n) with a cone and plate geometry. In both the rheometers used, a shearing flow is imposed for a suitable time so that a steady shearing flow is obtained. The shear rate in a cone and plate geometry is given by $\dot{\gamma} = \Omega/\tan \alpha$, where Ω

is the steady angular rotation of the cone or plate, and α is the angle of the cone. The steady shear stress, τ is measured as the force that a liquid exerts on the surface per unit area of that surface and the steady-state viscosity is determined as, $\eta = \tau/\dot{\gamma}$. The equilibrium surface tension was measured using the KSV Theta optical tensiometer utilizing the pendant drop method for surface tension measurement.

3.4.1 Newtonian Rheology

For a Newtonian fluid, the steady-state shear viscosity η is often termed simply viscosity since in most situations it is the only one considered. The viscosity of the glycerol water solution was measured using the Brookfield cone and plate viscometer (LVDV-III+ with Rheocalc software). The rheometer was operated with the spindle number CPE51. Rheocalc software was used to control the rheometer and analyze the obtained data. The BEAVIS routine was used to determine the viscosity of the solution at different shear rates. This was done by increasing the shear rates in fixed increments (1 s^{-1}) and waiting a fixed amount of time (90 seconds) to obtain the steady viscosity for the specific shear rate. The shear stress versus shear rate data was fitted to a power law form to obtain the steady viscosity and the exponent as shown in Figure 3.2. The exponent obtained confirms that the fluid is indeed Newtonian. The viscosity of the 75 wt% glycerol water solution was 34 mPa.s.

3.4.2 Non-Newtonian Rheology

In a complex fluid, the rate of structural rearrangement can be determined by imposing small amplitude oscillatory shearing. In the cone and plate geometry this kind of motion is achieved by rotating the cone with an angular velocity, $\Omega(t) = \Omega_0 \cos(\omega t)$. The shear rate is also a function of time and it is given by $\dot{\gamma}(t) = \Omega(t)/\tan \alpha$ and hence the shear

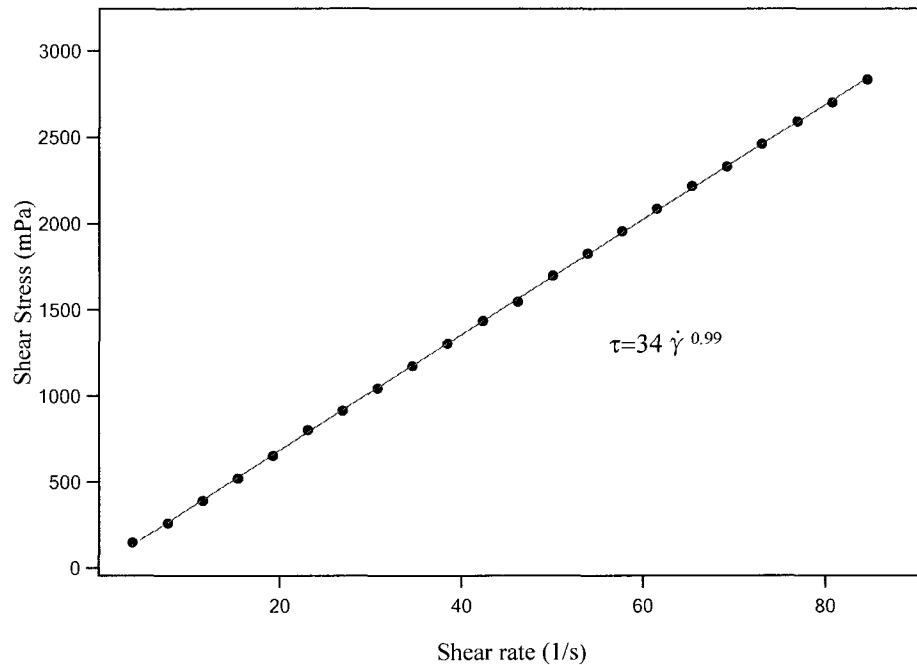


Figure 3.2: Shear stress as a function of shear rate for 75 wt % glycerol-water solution.

strain, given as the time integral of shear rate, is given by $\gamma = \Omega_0 \sin(\omega t) / \omega \tan \alpha$. The number Ω_0 / ω is defined as the amplitude of angular deflection and $\gamma_0 = \Omega_0 \tan \alpha / \omega$ is defined as the strain amplitude. If γ_0 is very small then the fluid is not disturbed by the oscillations and the stress is controlled by the rearrangement of the fluid. The shear stress

is the response and it can be split into “in phase” and “out of phase” with the input deformation. The viscoelastic behavior of the system at different frequency is characterized by the storage modulus, G' , and the loss modulus, G'' , which respectively characterize the solid-like and fluid-like contributions to the measured stress response. The storage modulus G' , can be determined from the “in phase” component of the response and loss modulus, G'' , can be determined from the “out of phase” component of the response. For liquid-like fluids the storage modulus, G' is much less than the loss modulus, G'' (i.e. $G' \ll G''$) and $G' \propto \omega$ and $G'' \propto \omega^2$. The frequency dependence of G' and G'' can be obtained by applying Oscillatory Frequency Sweep (the TA Instruments oscillatory rheometer AR-550n). Figure 3.3 shows frequency dependence of G' and G'' for 2 wt% carboxymethyl cellulose solution. From Figure 3.3 we can see that at the lower frequencies the response is viscous-like with a loss modulus that is much larger than the storage modulus, while at the highest frequencies, the difference between the loss modulus and storage modulus becomes smaller indicating more solid-like behavior. Figures 3.4 and 3.5 show the frequency dependence of G' and G'' for 0.1 wt% polyacrylamide solution and 0.3 wt% polyacrylamide solution respectively. From Figures 3.4 and 3.5 we can see that at the lower frequencies the response is liquid-like with a storage modulus that is less than the loss modulus, while at the highest frequencies, the storage modulus dominates the response indicating solid-like behavior.

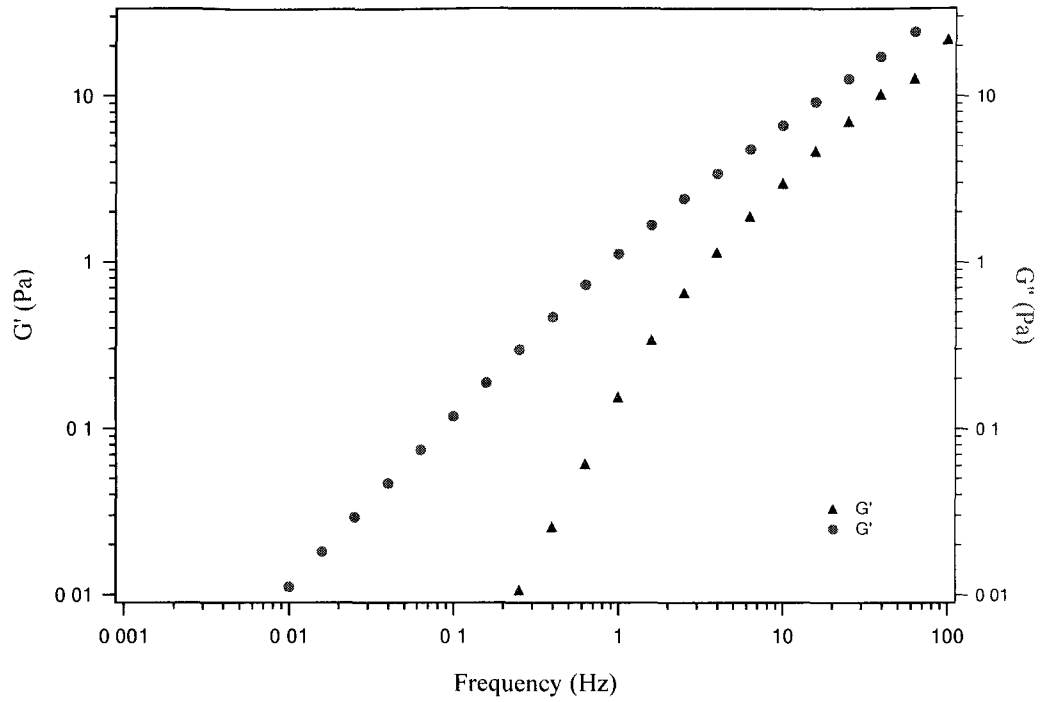


Figure 3.3: Frequency dependence of G' and G'' for 2 wt% carboxymethyl cellulose solution.

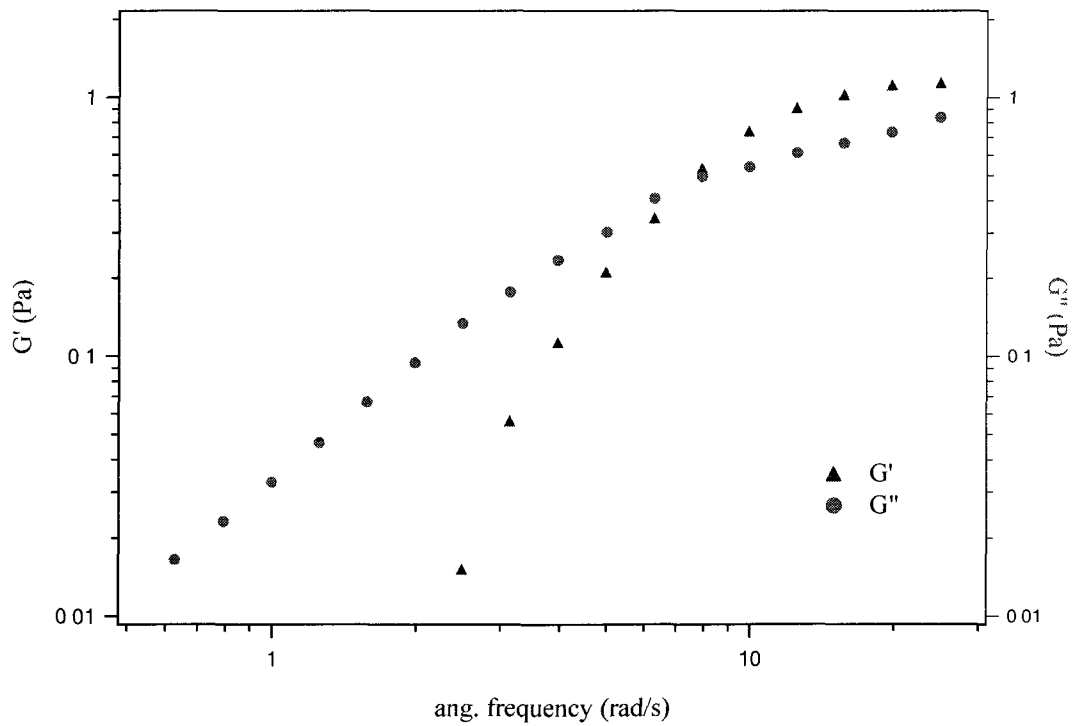


Figure 3.4: Frequency dependence of G' and G'' for 0.1 wt% polyacrylamide solution.

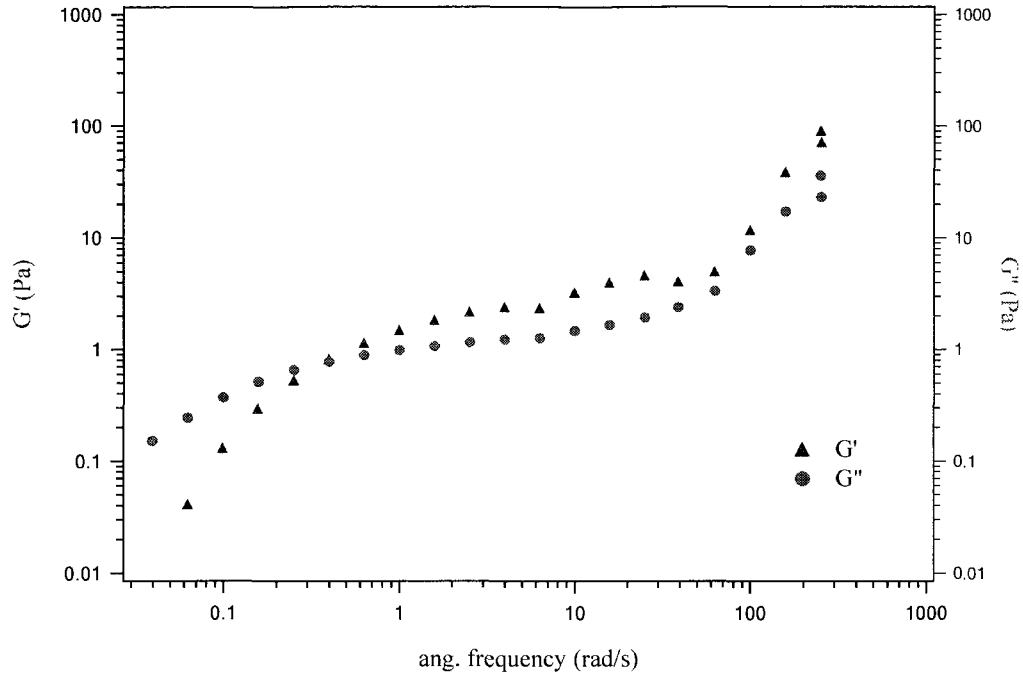


Figure 3.5: Frequency dependence of G' and G'' for 0.3 wt% polyacrylamide solution.

The steady-state shear viscosity of 2 wt% carboxymethyl cellulose, 0.1 wt% polyacrylamide, and 0.3 wt% polyacrylamide solutions were measured using the TA Instruments oscillatory rheometer (AR-550n). The experiments were conducted at 25°C. The rheometer was operated with an air supply system that provides the required pressure (37.5 psi.), a spindle (cone angle of 2°) and a pump and tank system to control the temperature. The AR Instrument control software was used to control the rheometer and analyze the obtained data. In order to evaluate the rheological properties of an unknown material, the Pseudo-Linear Viscoelastic Region (LVR) needed to be determined first by an Oscillatory Stress Sweep or Strain Sweep (OSS) experiment. Steady State Flow procedure was applied to determine the steady state shear viscosity. Figure 3.6 shows the

steady shear viscosity as a function of shear rate for 2 wt% carboxymethyl cellulose, 0.1 wt% polyacrylamide, and 0.3 wt% polyacrylamide solutions, respectively. The low shear rate plateau is known as the zero shear viscosity and is designated as η^0 . The zero shear viscosities were found to be 1810 mPa.s for 2 wt% carboxymethyl cellulose solution, 2570 mPa.s for 0.1 wt% polyacrylamide solution, and 21670 mPa.s for 0.3 wt% polyacrylamide solution. From Figure 3.6 we can also see that the viscosities for all solutions decrease with increasing shear rate, which indicates that 2 wt% carboxymethyl cellulose, 0.1 wt% polyacrylamide, and 0.3 wt% polyacrylamide solutions are all shear-thinning fluids. While the zero shear viscosity for the 2 wt% carboxymethyl cellulose solution is lower than either of the polyacrylamide solutions, the 2 wt% carboxymethyl solution exhibits a higher viscosity compared to the polyacrylamide solutions at shear rates greater than $\sim 2/s$.

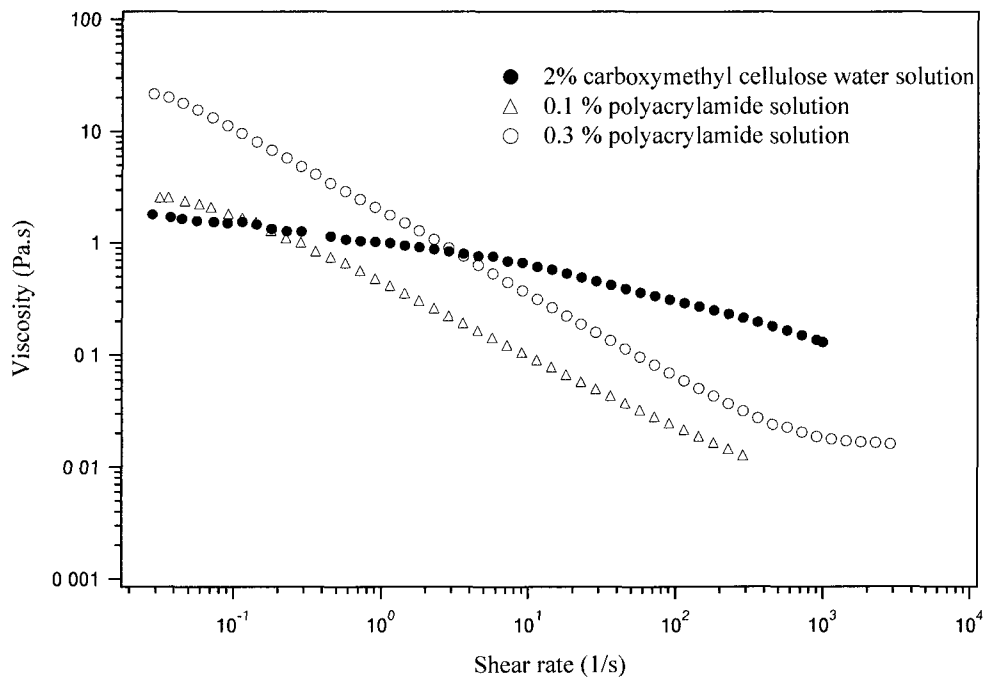


Figure 3.6: Steady shear viscosity as a function of shear rate for 2 wt% carboxymethyl cellulose, 0.1 wt% polyacrylamide, and 0.3 wt% polyacrylamide solutions.

3.4.3 Surface Tension

Surface tension is a property of the surface of a fluid that allows it to resist an external force. The surface tension of the two phase systems in the presence of different surfactants was measured as a function of surfactant concentration by pendant drop method. In the pendant drop method, drop of one liquid is generated at the tip of a needle and allowed to reach mechanical equilibrium. At equilibrium, the profile of the drop is determined by a balance between gravity and interfacial forces given by the Young-Laplace equation. The surface tension of the liquid is determined as the parameter that gives the best fit of the drop profile to the Young-Laplace equation. The KSV Theta optical tensiometer (Attension Theta) was used to obtain the equilibrium surface tension data and consisted of a light source, a camera, and a syringe clamp. First, the image was calibrated with a 4mm diameter smooth steel ball. Then, the liquid was loaded in the syringe (or cuvet) forming a nicely shaped pendant drop. In order to obtain a good video image, the magnification was adjusted to let the drop occupy about 60% of the total area of the image since small drops did not provide enough pixels for good accuracy. A standard solution (ultrapure water from Millipore Direct-Q 3 UV with resistivity of 18.2 M Ω •cm) was measured first to ensure the instrument was working accurately and then the analyte was measured. The next step was to take a movie over a relatively long time to ensure stability. If surfactants were present in the fluid, a time variation in surface tension with interface age would be expected; otherwise a stable measurement with only variations from noise would be found. Surface tension was determined by fitting the shape of the drop (in a captured video image) to the Young-Laplace equation which relates surface tension to drop shape.

In Figures 3.7-3.13, we plot the equilibrium surface tension versus bulk surfactant concentration for all the surfactants and suspending fluid combinations used in our experiments. Figures 3.7-3.13 clearly showed that surface tension is greatly affected by the presence of surfactants. When a small amount of surfactant was added to a suspending solution, the equilibrium surface tension was not affected. With the increase of surfactant concentration, the equilibrium surface tension decreased monotonically until it reached a lower plateau value, which is called the critical micelle concentration (CMC) point and remained more or less constant thereafter. Below CMC, surfactants only appear in monomer form while above CMC, surfactants start to aggregate and form micelles. Apparent CMC values of all the surfactants were calculated from the sharp change in the slope in the surface tension versus surfactant concentration plots. The apparent CMC values of TX-100 in 75 wt% glycerol water solution, Aerosol-OT in 75 wt% glycerol water solution, sodium dodecyl sulfate in 75 wt% glycerol water solution, TX-100 in 2 wt% carboxymethyl cellulose solution, and Tergitol 15-S-9 in 2 wt% carboxymethyl cellulose solution, 0.1 wt% polyacrylamide solution, and 0.3 wt% polyacrylamide solution occurred at 450ppm, 3000ppm, 6000ppm, 200ppm, 200ppm, 200 ppm, and 300 ppm, respectively.

The various two-phase systems for Newtonian and Non-Newtonian cases used in our experiments, and their corresponding physical properties are listed in Table 3.3 and Table 3.4, respectively. The physical properties of the prepared solutions in Table 3.3 and Table 3.4 were determined at the same temperature at which the experiments were conducted. In order to help the presentation of the experimental results, each two-phase

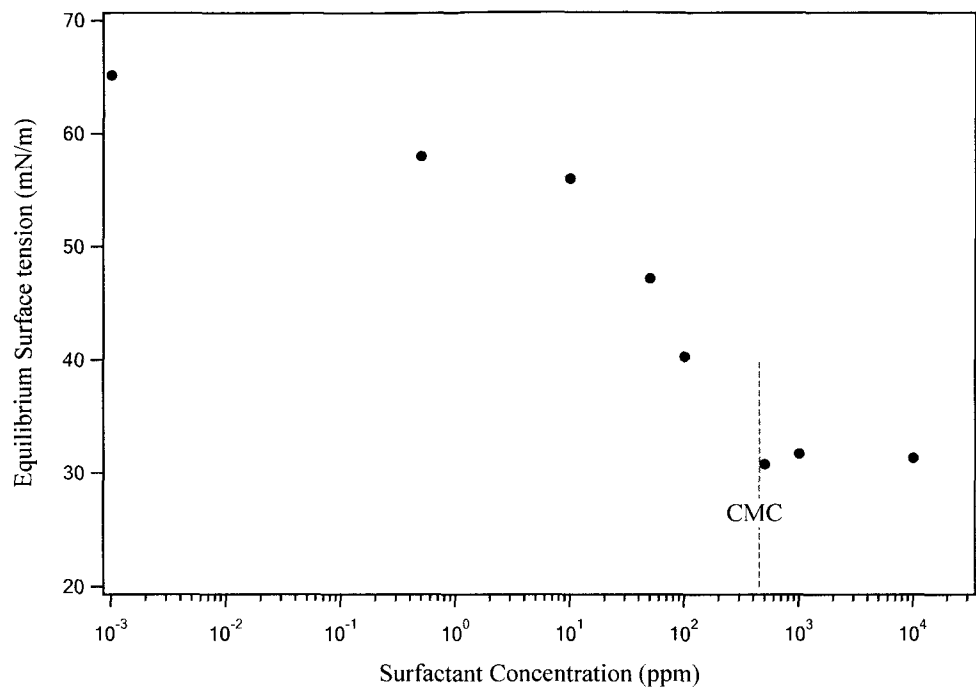


Figure 3.7: Surface tension of Triton X-100 in 75 wt% glycerol water solution.

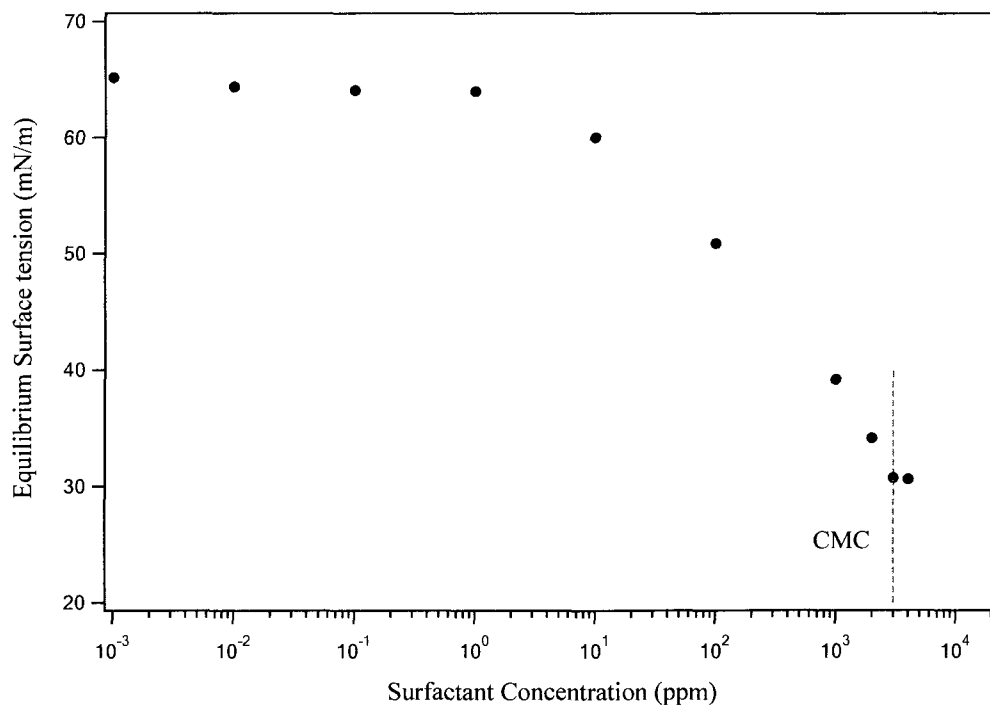


Figure 3.8: Surface tension of Aerosol-OT in 75 wt% glycerol water solution.

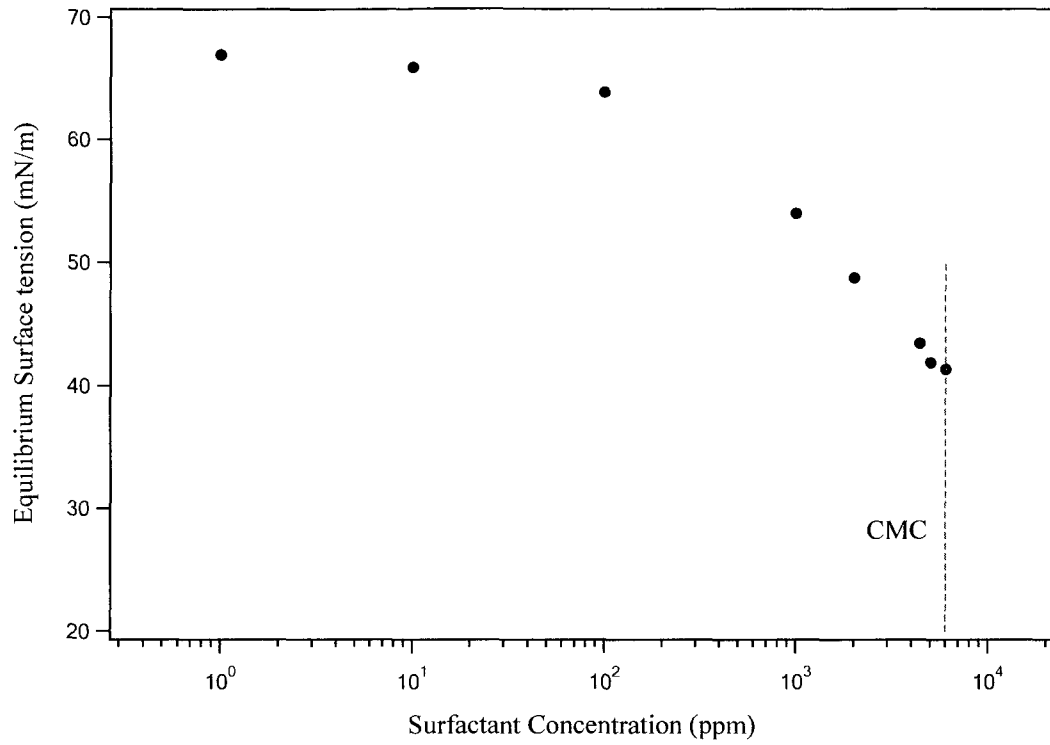


Figure 3.9: Surface tension SDS in 75 wt% glycerol water solution.

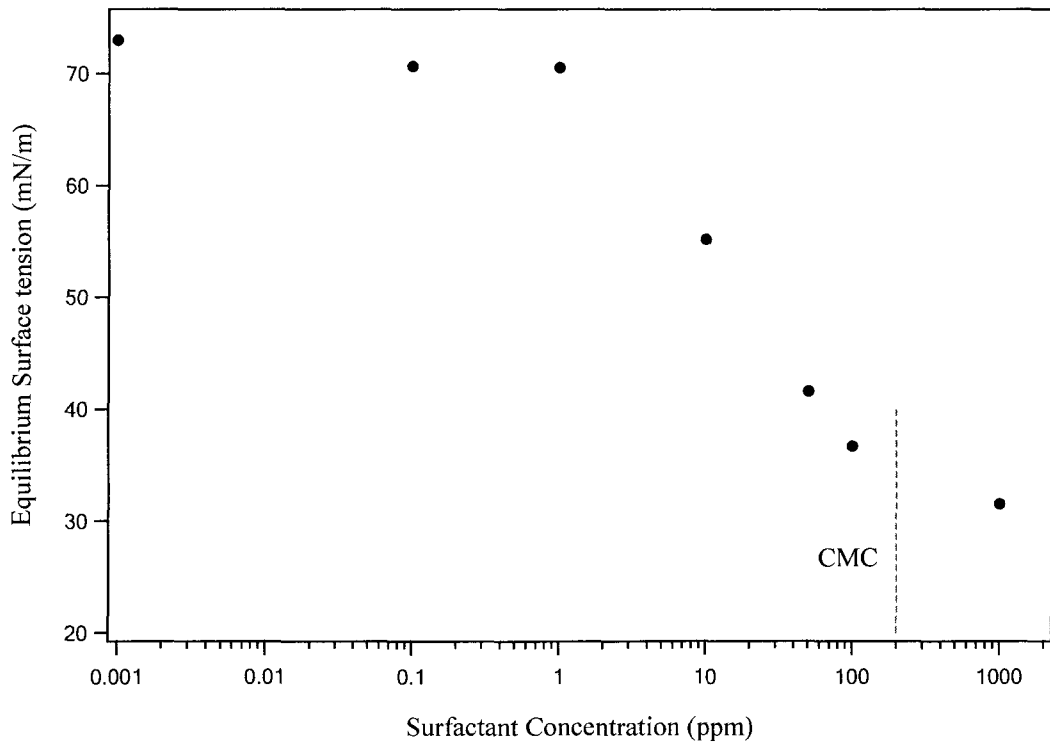


Figure 3.10: Surface tension of Triton X-100 in 2 wt% carboxymethyl cellulose solution.

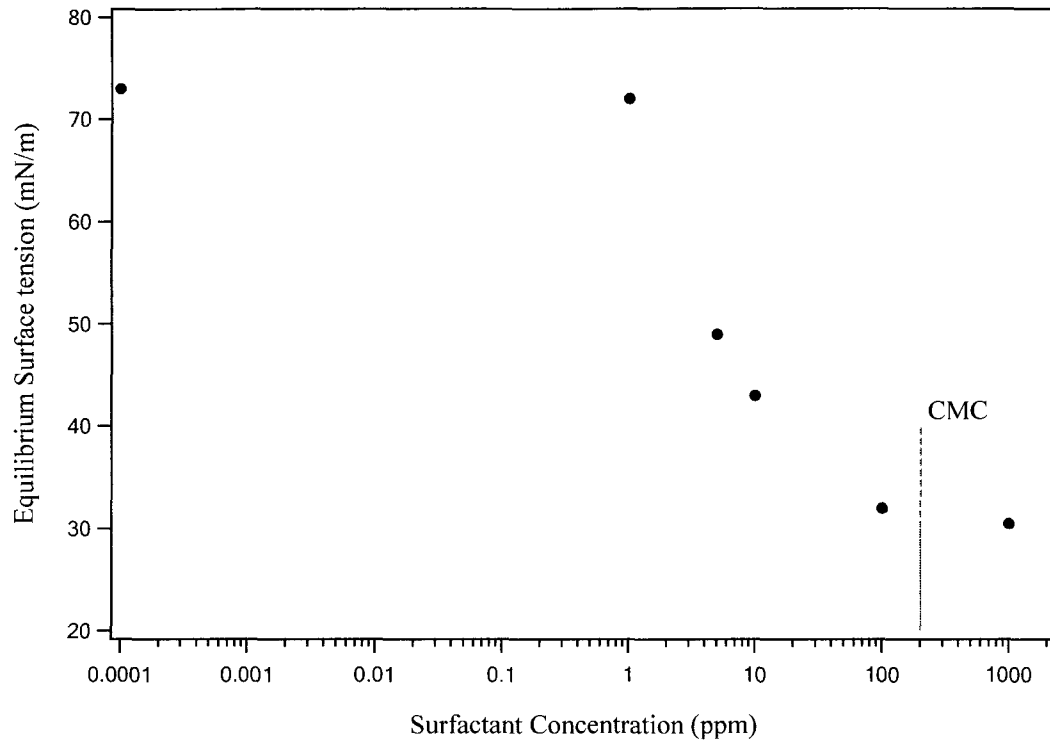


Figure 3.11: Surface tension of Tergitol 15-S-9 in 2 wt% carboxymethyl cellulose solution.

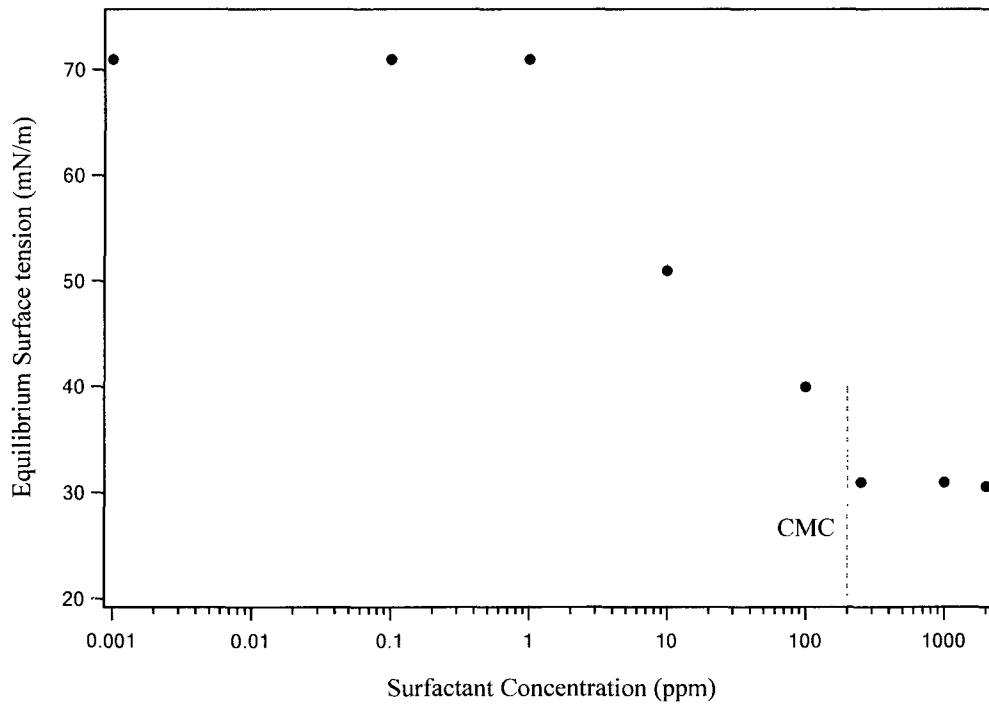


Figure 3.12: Surface tension of Triton X-100 in 0.1 wt% polyacrylamide solution.

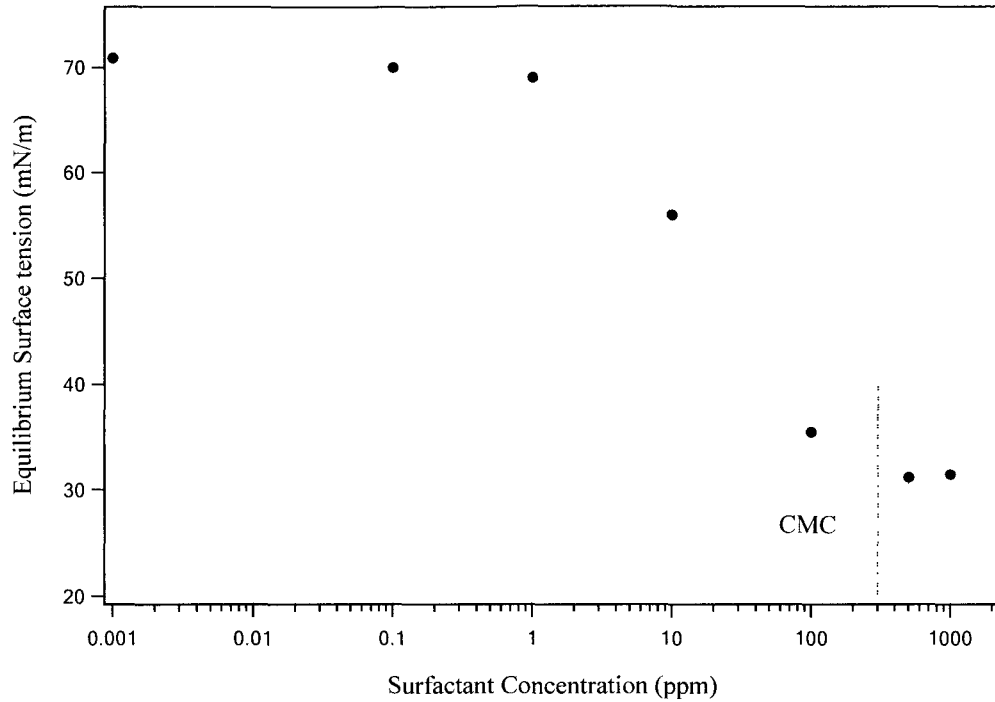


Figure 3.13: Surface tension of Triton X-100 in 0.3 wt% polyacrylamide solution.

system is designated a number identifying the geometry of the channel (1 for 10mm circular channel, 2 for 10×10mm square channel, 3 for 15×15mm square channel, 4 for 16×3mm rectangular channel, and 5 for 32×3mm rectangular channel). The channel geometry is followed by a symbol specifying the surfactant and bulk solution. For Newtonian systems, G was used for clean 75 wt% glycerol water solution, TG represented Triton X-100 in 75 wt% glycerol water solution, AG referred to Aerosol-OT in 75 wt% glycerol water solution, and SG was used for sodium dodecyl sulfate in 75 wt% glycerol water solution. For Non-Newtonian clean systems, C represented clean 2 wt% glycerol water solution. For Non-Newtonian clean systems, C represented clean 2 wt% carboxymethyl cellulose solution, P for clean 0.1 wt% polyacrylamide solution, and PP for clean 0.3 wt% polyacrylamide solution. As for non-Newtonian systems with surfactants, TC was used for Triton X-100 in 2 wt% carboxymethyl cellulose solution, TeC referred to Tergitol 15-S-9 in 2 wt% carboxymethyl cellulose solution, TP was used

for Triton X-100 in 0.1 wt% polyacrylamide solution, and TPP was used for Triton X-100 in 0.3 wt% polyacrylamide solution. The last letter represented surfactant concentration (a for 0.1ppm, b for 0.5ppm, c for 1ppm, d for 5 ppm, e for 10ppm, f for 50ppm, g for 100ppm, h for 250ppm, i for 500ppm, j for 750ppm, k for 1000ppm, and l for 2200ppm).

3.5 MODEL PROBLEM

Figure 3.14 shows the schematic of a bubble rising in a vertical channel of hydraulic diameter, D_H . The density and viscosity of the bulk phase is designated as ρ and η^0 , respectively. The density and viscosity of the drop phase is represented as ρ_d and η_d^0 , respectively. The drop velocity reaches a steady state, U_d along the axis of the channel. The equilibrium surface tension between the bulk phase and the drop phase is represented by σ_{eq} . The size of the drop is characterized by the radius of a spherical drop of the same volume. Therefore, $a=(3V_d/4\pi)^{1/3}$, where V_d is the volume of the drop. The dynamics of drops and bubbles in square and rectangular channels are different from that in cylindrical tubes due to the non-uniform fluid film surrounding the fluid particles. For the three channel geometries studied, the drop profile in the cross-sectional view may either be axisymmetric as seen in Figure 3.2 (a), (b) and (d) or non-axisymmetric as seen in Figure 3.14 (c) and (e). Kolb and Cerro conducted an experimental study ([19]) and a numerical study ([20]) at intermediate to high Capillary and Bond numbers. Their

Table 3.3: Material properties of Newtonian systems studied
 Drop fluid: Air ($\rho_d=1.2\text{kg/m}^3$, $\eta_d=0.02\text{mPa}\cdot\text{s}$), Bulk fluid: G($\eta^0=33\text{mPa}\cdot\text{s}$)

System	Channel size	Surfactant	$\rho(\text{kg/m}^3)$	$\sigma(\text{mN/m})$
1-G	D10mm	0ppm TX	1180	65.2
1-TG-e	D10mm	10ppm TX	1195	56.0
1-TG-g	D10mm	100ppm TX	1200	40.3
2-G	10×10mm	0ppm TX	1180	65.2
2-TG-c	10×10mm	1ppm TX	1185	58.0
2-TG-e	10×10mm	10ppm TX	1195	56.0
2-TG-g	10×10mm	100ppm TX	1200	40.3
2-TG-k	10×10mm	1000ppm TX	1203	31.4
3-G	15×15mm	0ppm TX	1180	65.2
3-TG-c	15×15mm	1ppm TX	1185	58.0
3-TG-e	15×15mm	10ppm TX	1195	56.0
3-TG-g	15×15mm	100ppm TX	1200	40.3
3-TG-k	15×15mm	1000ppm TX	1203	31.4
4-G	16×3mm	0ppm TX	1180	65.2
4-TG-c	16×3mm	1ppm TX	1181	58.0
4-TG-e	16×3mm	10ppm TX	1195	56.0
4-TG-g	16×3mm	100ppm TX	1200	40.3
4-TG-h	16×3mm	250ppm TX	1200	40.0
4-TG-i	16×3mm	500ppm TX	1200	30
4-TG-j	16×3mm	750ppm TX	1200	31.0
4-TG-k	16×3mm	1000ppm TX	1200	31.4
5-G	32×3mm	0ppm TX	1180	65.2
5-TG-b	32×3mm	0.5ppm TX	1181	59.0
5-TG-e	32×3mm	10ppm TX	1195	56.0
2-AG-c	10×10mm	1ppm AOT	1182	64.0
2-AG-e	10×10mm	10ppm AOT	1185	60.0
2-AG-g	10×10mm	100ppm AOT	1186	50.9
2-AG-k	10×10mm	1000ppm AOT	1192	39.2
2-SG-e	10×10mm	10ppm SDS	1191	65.0
2-SG-g	10×10mm	100ppm SDS	1199	63.9
2-SG-h	10×10mm	500ppm SDS	1200	58.0
2-SG-k	10×10mm	1000ppm SDS	1204	54.0
2-SG-l	10×10mm	2200ppm SDS	1208	48.8

experimental results showed that the bubble was non-axisymmetric for $Ca < 0.1$ and axisymmetric for $Ca > 0.1$ [19]. In our case, the Ca numbers were all larger than 0.1 for long and large bubbles rising in square channels. The bubbles, whose Ca number was less than 0.1 were small bubbles. These small bubbles were far away from the tube wall and hence axisymmetric. Therefore, we assumed that all the bubbles in square channels

were axisymmetric as shown in Figure 3.14(b). In rectangular channels, small bubbles were expected to be axisymmetric while the large bubbles were expected to be non-axisymmetric with a pancake-like shape. Since there was no camera installed along the depth of the channel, it was not possible to determine the thickness of the large bubbles. Hence, in analyzing the bubbles rising through rectangular channels, bubble area was used instead of bubble volume to characterize the bubble size. The size of the bubble is thus characterized by the radius of a circular bubble of the same area. Therefore, for rectangular channels, $a = (A_d/\pi)^{1/2}$, where A_d is the area of the bubble.

The bubble shape is characterized by the bubble length, L , the width, B and the deformation parameter, Δ . L and B are defined as the maximum axial and radial length of the steady bubble profile. The deformation parameter is defined as:

$$\Delta = \frac{(L - B)}{(L + B)} \quad (3.1)$$

Equation 3.1 indicates that Δ equals to zero for spherical bubbles with $L = B$. The deformation parameter is positive if the bubbles are elongated along the flow direction, i.e. $\Delta > 0$ and if the bubbles are elongated perpendicular to the flow direction, $\Delta < 0$. We define the film thickness, δ as the minimum distance between the bubble edge and the confining wall as shown in Figure 3.14.

3.6 DATA ANALYSIS

The videos of the experiment captured using PixelINK Capture OEM were analyzed by National Instruments Vision Assistant software. The images were first calibrated using

Table 3.4: Material properties and range of dimensionless parameters of systems studied
 Bulk fluid: $C(\eta^0=1811\text{mPa}\cdot\text{s})$, $P(\eta^0=2570\text{mPa}\cdot\text{s})$, and $PP(\eta^0=21670\text{mPa}\cdot\text{s})$.

System	Channel size	Suspending fluid	Surfactant	$\rho(\text{kg/m}^3)$	$\sigma(\text{mN/m})$
1-C	D10mm	2% carboxymethyl cellulose solution	0ppm TX	1007	74.0
1-TC-e	D10mm	2% carboxymethyl cellulose solution	10ppm TX	1012	54.5
1-TC-g	D10mm	2% carboxymethyl cellulose solution	100ppm TX	1015	34.2
2-C	10×10mm	2% carboxymethyl cellulose solution	0ppm TX	1007	74.0
2-TC-c	10×10mm	2% carboxymethyl cellulose solution	1ppm TX	1007	70.5
2-TC-e	10×10mm	2% carboxymethyl cellulose solution	10ppm TX	1012	54.5
2-TC-f	10×10mm	2% carboxymethyl cellulose solution	50ppm TX	1013	43.0
2-TC-g	10×10mm	2% carboxymethyl cellulose solution	100ppm TX	1015	34.2
2-TC-k	10×10mm	2% carboxymethyl cellulose solution	1000ppm TX	1016	32.2
3-C	15×15mm	2% carboxymethyl cellulose solution	0ppm TX	1007	74.0
3-TC-e	15×15mm	2% carboxymethyl cellulose solution	10ppm TX	1012	54.5
3-TC-g	15×15mm	2% carboxymethyl cellulose solution	100ppm TX	1015	34.2
3-TC-k	15×15mm	2% carboxymethyl cellulose solution	1000ppm TX	1016	32.2
4-C	16×3mm	2% carboxymethyl cellulose solution	0ppm TX	1007	74.0
4-TC-a	16×3mm	2% carboxymethyl cellulose solution	0.1ppm TX	1007	70.7
4-TC-c	16×3mm	2% carboxymethyl cellulose solution	1ppm TX	1007	70.5
4-TC-e	16×3mm	2% carboxymethyl cellulose solution	10ppm TX	1012	54.5
4-TC-f	16×3mm	2% carboxymethyl cellulose solution	50ppm TX	1013	41.6
4-TC-g	16×3mm	2% carboxymethyl cellulose solution	100ppm TX	1015	34.2
4-TC-k	16×3mm	2% carboxymethyl cellulose solution	1000ppm TX	1016	32.2
5-C	32×3mm	2% carboxymethyl cellulose solution	0ppm TX	1007	74.0
5-TC-a	32×3mm	2% carboxymethyl cellulose solution	0.1ppm TX	1012	70.7
5-TC-c	32×3mm	2% carboxymethyl cellulose solution	1ppm TX	1015	70.5
5-TC-e	32×3mm	2% carboxymethyl cellulose solution	10ppm TX	1016	54.5
1-TeC-c	D10mm	2% carboxymethyl cellulose solution	1ppm TER	1007	72.0
1-TeC-g	D10mm	2% carboxymethyl cellulose solution	100ppm TER	1009	32.0
1-TeC-k	D10mm	2% carboxymethyl cellulose solution	1000ppm TER	1009	30.5
2-TeC-c	10×10mm	2% carboxymethyl cellulose solution	1ppm TER	1007	72.0
2-TeC-d	10×10mm	2% carboxymethyl cellulose solution	5ppm TER	1007	49.0
2-TeC-e	10×10mm	2% carboxymethyl cellulose solution	10ppm TER	1008	43.0
2-TeC-g	10×10mm	2% carboxymethyl cellulose solution	100ppm TER	1009	32.0
2-TeC-k	10×10mm	2% carboxymethyl cellulose solution	1000ppm TER	1009	30.5
3-TeC-c	15×15mm	2% carboxymethyl cellulose solution	1ppm TER	1007	72.0
3-TeC-d	15×15mm	2% carboxymethyl cellulose solution	5ppm TER	1007	49.0
3-TeC-e	15×15mm	2% carboxymethyl cellulose solution	10ppm TER	1008	43.0
3-TeC-g	15×15mm	2% carboxymethyl cellulose solution	100ppm TER	1009	31.0
3-TeC-k	15×15mm	2% carboxymethyl cellulose solution	1000ppm TER	1009	30.0
4-TeC-c	16×3mm	2% carboxymethyl cellulose solution	1ppm TER	1007	72.0
4-TeC-e	16×3mm	2% carboxymethyl cellulose solution	10ppm TER	1008	49.0
4-TeC-g	16×3mm	2% carboxymethyl cellulose solution	100ppm TER	1009	32.0
4-TeC-k	16×3mm	2% carboxymethyl cellulose solution	1000ppm TER	1009	30.5
2-P	10×10mm	0.1 % polyacrylamide solution	0ppm TX	993	71.0
2-TP-e	10×10mm	0.1 % polyacrylamide solution	10ppm TX	993	51
2-TP-g	10×10mm	0.1 % polyacrylamide solution	100ppm TX	993	40.0
2-TP-k	10×10mm	0.1 % polyacrylamide solution	1000ppm TX	993	31.0
2-PP	10×10mm	0.3 % polyacrylamide solution	0ppm TX	997	70.9
2-TPP-e	10×10mm	0.3 % polyacrylamide solution	10ppm TX	997	56
2-TPP-g	10×10mm	0.3 % polyacrylamide solution	100ppm TX	997	35.5
2-TPP-k	10×10mm	0.3 % polyacrylamide solution	1000ppm TX	997	31.5

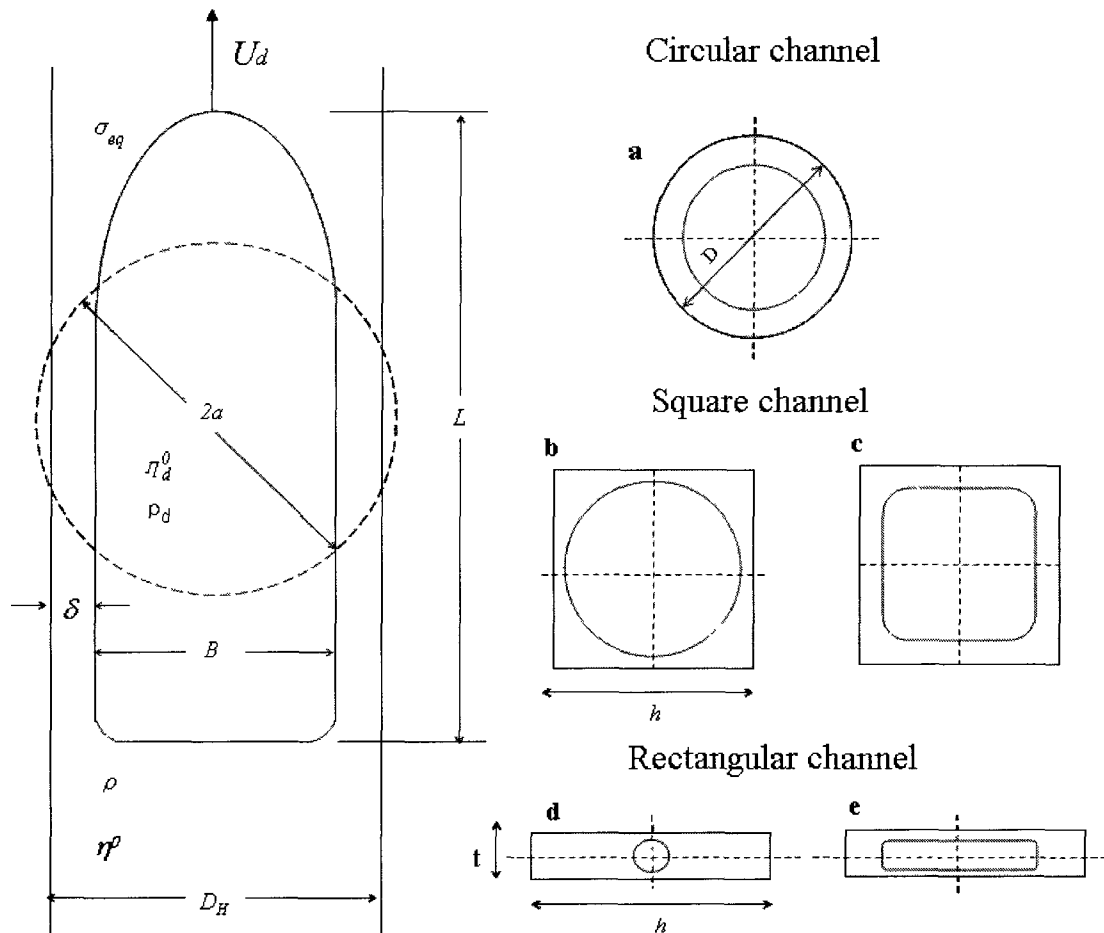


Figure 3.14: Schematic of the front view and the cross-sectional view of a bubble or drop rising through a channel. This bubble may be (a), (b) and (d) axisymmetric or (c) and (e) non-axisymmetric in the cross-sectional view.

the calibration image captured earlier to perform measurements in real-world units. The coordinates of the edge of the bubble were determined using the Edge Detection routine applied on the calibrated image as shown in Figure 3.15. A color threshold was applied to the three planes of the color image and placed the result into an 8-bit image shown in Figure 3.15(b). In Figure 3.15(c) a Sobel filter was applied to obtain the edge of the bubble. Finally, the contour of the bubble was marked to record the x and y positions for several points along the edge of the bubble (Figure 3.15(d)).

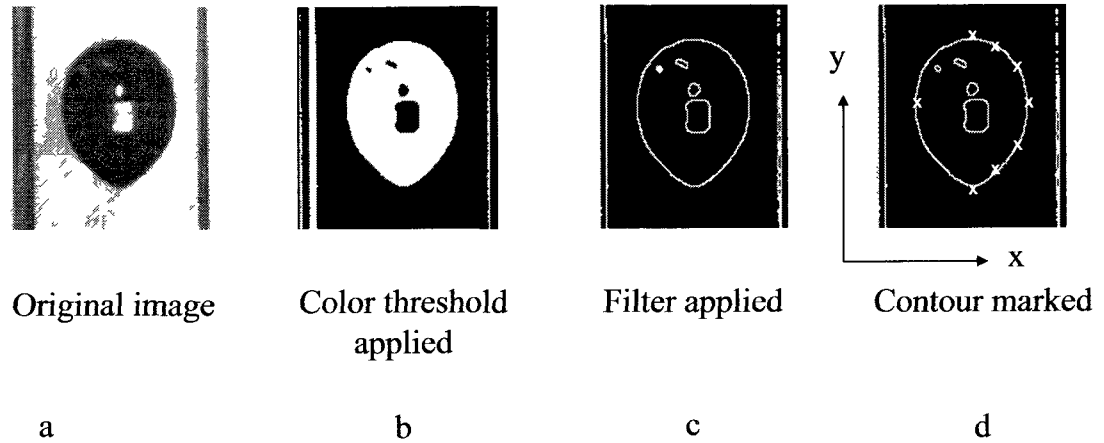


Figure 3.15: Schematic of the data analysis using National Instruments Vision Assistant.

Based on the x and y coordinate information, the maximum axial ($L=y_{\max}-y_{\min}$), the maximum equatorial dimensions ($B=x_{\max}-x_{\min}$), the film thickness ($\delta=0.5\times(D_H-B)$) of the bubble were calculated. In square and circular channels, the bubble or drop volume is calculated by the volume of evolution method shown in Figure 3.16. In rectangular channels, the bubble area was calculated by the procedure shown in Figure 3.17. The bubble velocity was calculated by evaluating the displacement of the top of the bubble between a specified number of frames at the known frame rate. For each experiment, three independent velocity measurements over different regions within the region of interest were made to check for any unsteadiness in the motion of the drop. The geometric deformation obtained for the drop shapes at axial positions within those regions were also used to detect unsteady drop behavior in the experiments, and to ensure that the shape and velocity measurements were indeed steady.

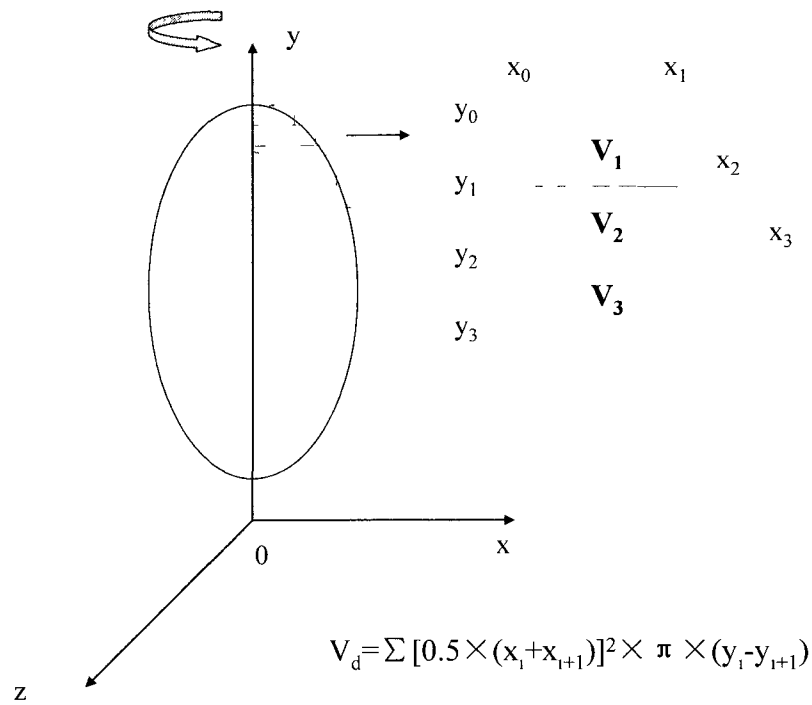


Figure 3.16. Volume calculation for square and circular channels: Volume of evolution

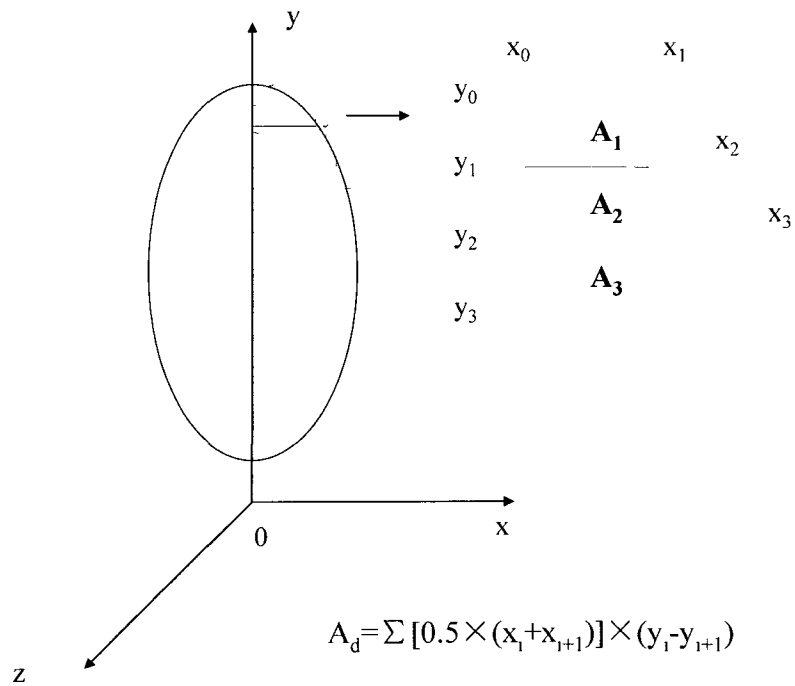


Figure 3.17: Area calculation for rectangular channels

3.7 DIMENSIONLESS PARAMETER SPACE

To non-dimensionalize the system variables, the drop velocity, U_d is selected as the characteristic velocity scale. The characteristic length scale, R_c , is chosen as half of the hydraulic diameter, D_H . For a cylindrical tube, $R_c=R$, the radius of the tube and $R_c=h/2$ for a square channel of side h . For a rectangular channel, $R_c =h \times t/(h+t)$. The dimensionless drop size is defined as,

$$\kappa = \frac{a}{R_c} \quad (3.2)$$

The viscosity ratio is given by

$$\lambda = \frac{\eta_d^0}{\eta^0} \quad (3.3)$$

The density ratio is given by

$$\gamma = \frac{\rho_d}{\rho} \quad (3.4)$$

The dynamic parameters that affect the dynamics of drops in tubes and channels are Reynolds number, Bond number, Capillary number and Weber number. Reynolds number (Re) is the ratio of inertial forces to viscous forces and is given by the formula:

$$Re = \frac{\rho U_d R_c}{\eta^0} \quad (3.5)$$

Bond number is the ratio of gravitational forces to interfacial forces and is given by the formula:

$$Bo = \frac{(\rho - \rho_d)gR_c^2}{\sigma} \quad (3.6)$$

Capillary number is the ratio of viscous forces to interfacial forces and is given by the formula:

$$Ca = \frac{\eta^0 U_d}{\sigma} \quad (3.7)$$

Weber number (We_T) measures the relative importance of the fluid inertia compared to its surface tension, which is shown in equation 3.5.

$$We_T = \frac{\rho U_T^2 R_c}{\sigma} \quad (3.8)$$

U_T is the steady velocity of a long bubble rising in the channel. The range of dimensionless numbers of the various two-phase systems for Newtonian and Non-Newtonian cases used in our experiments are listed in Table 3.5 and Table 3.6, respectively.

Table 3.5: The range of dimensionless parameters of Newtonian systems studied
Bulk fluid: $G(\lambda=0.00055)$.

System	Bo	Re	Ca	We_T	$\gamma = \rho_d / \rho$
1-G	0.04	8.60-16.32	0.02-0.05	0.29	0.00102
1-TG-e	0.05	5.92-13.35	0.02-0.04	0.36	0.00100
1-TG-g	0.07	4.18-11.04	0.02-0.05	0.42	0.00100
2-G	4.43	5.89-19.24	0.02-0.05	0.49	0.00102
2-TG-c	5.01	4.79-17.64	0.02-0.06	0.55	0.00101
2-TG-e	5.23	4.75-15.11	0.02-0.05	0.57	0.00100
2-TG-g	7.30	3.60-15.00	0.02-0.07	0.77	0.00100
2-TG-k	9.39	7.35-15.50	0.004-0.08	1.06	0.00100
3-G	9.98	20.16-44.72	0.04-0.08	2.38	0.00102
3-TG-c	11.26	10.03-43.76	0.02-0.09	2.60	0.00101
3-TG-e	11.76	8.48-40.16	0.02-0.09	2.65	0.00100
3-TG-g	16.41	13.18-37.51	0.04-0.11	3.72	0.00100
3-TG-k	21.12	15.59-37.20	0.06-0.14	4.98	0.00100
4-G	1.13	2.79-6.68	0.02-0.06	0.19	0.00102
4-TG-c	1.28	2.22-6.28	0.01-0.04	0.20	0.00102
4-TG-e	1.30	1.45-6.28	0.01-0.04	0.21	0.00100
4-TG-g	1.71	3.25-6.52	0.03-0.05	0.29	0.00100
4-TG-h	1.75	0.33-5.59	0.02-0.05	0.27	0.00100
4-TG-i	2.50	1.55-4.24	0.02-0.05	0.20	0.00100
4-TG-j	2.42	1.74-5.86	0.02-0.07	0.31	0.00100
4-TG-k	2.39	2.02-6.02	0.02-0.07	0.33	0.00100
5-G	1.28	1.32-8.36	0.01-0.04	0.34	0.00102
5-TG-b	1.57	1.17-8.84	0.01-0.05	0.42	0.00102
5-TG-e	1.51	2.43-7.87	0.01-0.05	0.37	0.00100
2-AG-c	4.53	2.54-17.23	0.01-0.05	0.50	0.00102
2-AG-e	4.84	5.55-15.38	0.02-0.05	0.51	0.00101
2-AG-g	5.71	1.89-13.95	0.01-0.05	0.53	0.00101
2-AG-k	7.45	2.47-16.21	0.01-0.08	0.88	0.00101
2-SG-e	4.49	2.54-18.34	0.01-0.05	0.48	0.00101
2-SG-g	4.59	3.33-18.00	0.01-0.05	0.50	0.00100
2-SG-h	5.07	5.75-15.60	0.02-0.05	0.56	0.00100
2-SG-k	5.46	1.38-15.24	0.005-0.05	0.63	0.00100
2-SG-l	6.06	4.37-15.77	0.02-0.06	0.74	0.00099

Table 3.6: The range of dimensionless parameters of Non-Newtonian systems studied
 Bulk fluid: C ($\lambda = 0.001$), P ($\lambda = 8 \times 10^{-6}$), and PP ($\lambda = 9 \times 10^{-7}$).

System	Bo	Re	Ca	We_T	$\gamma = \rho_d / \rho$
1-C	0.13	0.001-0.09	0.05-0.39	0.01	0.00119
1-TC-e	0.18	0.01-0.07	0.05-0.40	0.01	0.00119
1-TC-g	0.29	0.03-0.04	0.24-0.39	0.01	0.00118
2-C	3.33	0.01-0.06	0.05-0.55	0.013	0.00119
2-TC-c	3.50	0.003-0.05	0.03-0.50	0.013	0.00119
2-TC-e	4.55	0.02-0.05	0.21-0.54	0.013	0.00119
2-TC-f	5.77	0.01-0.04	0.15-0.56	0.02	0.00118
2-TC-g	7.27	0.003-0.04	0.07-0.77	0.03	0.00118
2-TC-i	7.73	0.02-0.07	0.33-1.45	0.10	0.00118
3-C	7.50	0.04-0.36	0.21-2.12	0.74	0.00119
3-TC-e	10.23	0.04-0.32	0.34-2.53	0.77	0.00119
3-TC-g	16.36	0.10-0.30	1.31-3.77	1.12	0.00118
3-TC-i	17.34	0.08-0.35	1.12-4.66	1.56	0.00118
4-C	0.83	0.003-0.02	0.06-0.37	0.008	0.00119
4-TC-a	0.93	0.01-0.02	0.24-0.36	0.007	0.00119
4-TC-c	0.77	0.003-0.02	0.06-0.35	0.006	0.00119
4-TC-e	1.13	0.005-0.02	0.11-0.41	0.007	0.00119
4-TC-f	1.58	0.006-0.02	0.17-0.56	0.01	0.00118
4-TC-g	1.61	0.002-0.01	0.10-0.48	0.005	0.00118
4-TC-i	1.71	0.005-0.03	0.20-1.14	0.03	0.00118
5-C	1.07	0.0002-0.004	0.03-0.55	0.02	0.00119
5-TC-a	1.12	0.006-0.03	0.10-0.56	0.02	0.00119
5-TC-c	1.12	0.004-0.03	0.07-0.57	0.02	0.00119
5-TC-e	1.46	0.003-0.04	0.07-0.77	0.03	0.00119
1-TeC-c	0.14	0.01-0.06	0.05-0.27	0.008	0.00119
1-TeC-g	0.31	0.03-0.04	0.33-0.44	0.02	0.00119
1-TeC-i	0.32	0.02-0.09	0.20-0.97	0.08	0.00119
2-TeC-c	3.43	0.02-0.05	0.21-0.49	0.01	0.00119
2-TeC-d	5.03	0.02-0.06	0.27-0.78	0.02	0.00119
2-TeC-e	5.74	0.02-0.05	0.37-0.79	0.03	0.00119
2-TeC-g	7.72	0.01-0.04	0.22-0.73	0.02	0.00119
2-TeC-i	8.10	0.02-0.06	0.33-1.26	0.07	0.00119
3-TeC-c	7.71	0.07-0.32	0.42-1.95	0.62	0.00119
3-TeC-d	11.33	0.03-0.33	0.26-2.95	0.95	0.00119
3-TeC-e	12.92	0.03-0.35	0.28-3.58	1.21	0.00119
3-TeC-g	17.38	0.04-0.31	0.54-4.22	1.31	0.00119
3-TeC-i	18.23	0.05-0.38	0.71-5.36	1.95	0.00119
4-TeC-c	0.87	0.003-0.01	0.05-0.19	0.002	0.00119
4-TeC-e	1.47	0.001-0.01	0.03-0.31	0.004	0.00119
4-TeC-g	1.97	0.002-0.009	0.08-0.34	0.002	0.00119
4-TeC-i	2.07	0.003-0.02	0.15-0.77	0.01	0.00119
2-P	3.43	0.10-0.23	1.91-4.29	0.36	0.00001
2-TP-e	4.77	0.01-0.22	0.28-5.81	0.41	0.00001
2-TP-g	6.08	0.01-0.17	0.05-0.56	0.59	0.00001
2-TP-i	7.85	0.10-0.22	4.46-9.29	0.90	0.00001
2-PP	3.44	0.004-0.01	5.29-10.52	0.06	0.00120
2-TPP-e	4.36	0.001-0.01	1.00-13.41	0.08	0.00120
2-TPP-g	6.88	0.001-0.006	3.42-16.75	0.06	0.00120
2-TPP-i	7.75	0.001-0.01	4.37-28.74	0.23	0.00120

Chapter 4

RESULTS AND DISCUSSION

The experimental results for the motion of bubbles rising in Newtonian and Non-Newtonian fluids in the absence and presence of surfactants are presented in the following sections. For all the experiments conducted, data are reported only for the bubbles that were rising at the centerline of the channels. The edges of the images presented in this thesis do not correspond to the edge of the channel wall. We first discuss the results for bubbles rising in a Newtonian bulk fluid and then the results for bubbles rising in a Non-Newtonian bulk fluid. For each experimental fluid combination, we conducted a steady state test on at least five bubbles ranging from the smallest to the largest to ensure that the deformations and velocities obtained were indeed steady. In order to measure the variation of bubble volume, bubble width, bubble length, deformation parameter, film thickness, and bubble velocity, we conducted error analysis on the results for the surfactant-free Newtonian and non-Newtonian fluid cases. To do this, four different frames in the “Region of Interest” were analyzed for each bubble to obtain the average, maximum, and minimum values of the desired parameter. The results are presented as error bars in Figures 4.1 - 4.5 for the Newtonian bulk fluid case and in Figures 4.33 - 4.37 for the non-Newtonian bulk fluid case.

4.1 NEWTONIAN BULK FLUID

4.1.1 Surfactant-free System

In this sub-section, the clean results for bubbles rising in a 10 mm square channel filled with 75 wt% glycerol water solution (2-G) are presented to aid in comparison with the results for bubbles rising in surfactant solutions. The dimensional terminal velocity, U_d , of the rising bubbles with error bars is shown in Figure 4.1. The shapes of the bubbles corresponding to some of the data points, marked with open circular symbols, are also presented as insets within Figure 4.1. Bubbles at small bubble volumes are nearly spherical in shape. As the bubble volume increases, the bubbles become oblate losing fore and aft symmetry. As the bubble size becomes comparable to the tube, the bubble becomes more elongated with higher positive curvature at the front of the bubble. Beyond a critical bubble volume, any increase in the volume of the bubble results in increasing the length of the bubble without affecting the shape of the front and rear ends of the bubble. The terminal velocity of small bubbles increases linearly with increasing bubble volume because of the increased buoyancy force. As the bubble size becomes comparable to the channel size, the drag force due to the confining walls increases resulting in a decrease in the terminal velocity. Beyond a critical bubble volume, the bubble velocity reaches a constant plateau value, U_T , where the bubble velocity is independent of the bubble volume. This trend has been observed in earlier experiments by Bretherton [7] and Borhan and Pallinti [6] for bubbles in cylindrical tubes and by Li et al. [23] for bubbles in square channels. As seen in Figure 4.1, the choice of frame within the “Region of Interest” does not affect the velocity or volume of the bubble significantly.

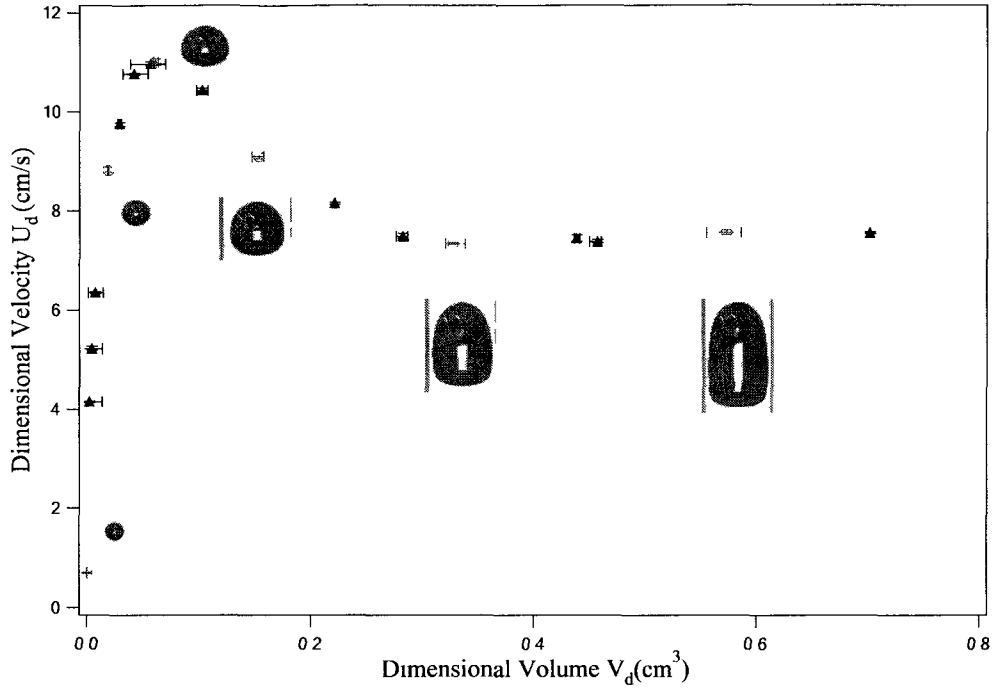


Figure 4.1: Terminal velocity of steady bubbles as a function of bubble size for bubbles rising in 75 wt% glycerol water solution in 10×10 mm square channel (2-G). The open symbols correspond to the bubbles presented in the figure.

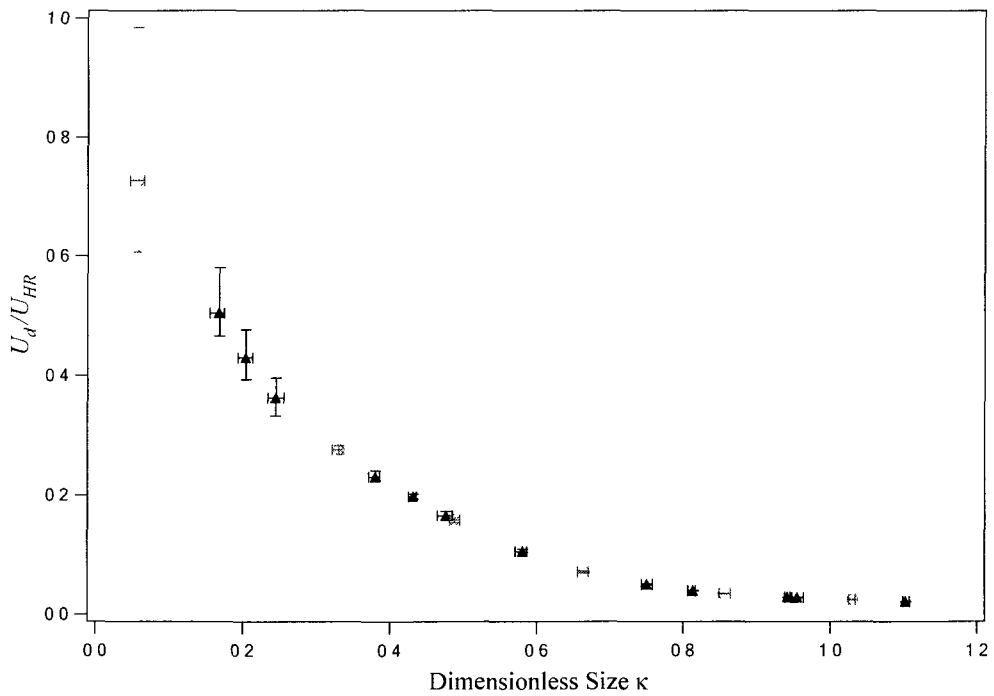


Figure 4.2: Terminal velocity of steady bubbles normalized with the Hadamard-Rybczynski velocity as a function of dimensionless bubble size for bubbles rising in 75 wt% glycerol water solution in 10×10 mm square channel (2-G).

Larger variation of volume is seen for larger bubble sizes. However, since the velocity of these bubbles reaches a constant value, the shape and location of the velocity-volume curve remains unaffected. The velocity of the bubble normalized with the Hadamard-Rybczynski velocity, $U_{HR} = (\rho - \rho_d)g R_{eq}^2 / 3\eta^0$ for a spherical bubble of the same volume rising in an unbounded fluid as a function of the dimensionless bubble size, κ is shown in Figure 4.2. Even for the smallest bubble size studied, $\kappa \approx 0.15$ for which the bubble is nearly spherical, the bubble velocity is much less than the bubble velocity expected for the same bubble in unbounded flow (average $U_d/U_{HR} = 0.73$). This may be attribute to the additional drag force due to the confining walls. For large bubble volumes, the steady bubble volume is only a fraction of its velocity in an unbounded flow ($U_d/U_{HR} \approx 0.02$). From Figure 4.2 we can see that there is very large error in the non-dimensional velocity at smaller bubble sizes because of its dependence on the Hadamard-Rybczynski velocity which in turn depends on the equivalent bubble radius, a . As the bubble size increases, this error reduces sharply.

The shape of the bubble is quantified by the non-dimensional maximum axial and equatorial length of the bubble, L and B , respectively and the deformation parameter, Δ . The bubble width, B versus the bubble length, L is shown in Figure 4.3 and the deformation parameter Δ , as a function of the dimensionless bubble size for bubbles rising in 75 wt% glycerol water solution in 10mm square channel (2-G) are shown in Figure 4.4. Small bubbles are nearly spherical as seen in Figures 4.3 and 4.4 where $L = B$ and $\Delta = 0$. For small bubble volumes, the bubble length and width increase almost

linearly with bubble size. As the bubble volume increases, the width of the bubble reaches an upper bound less than the size of the channel and any further increase in the bubble volume does not change the width of the bubble. However, the bubble length increases linearly at a much faster rate with increasing bubble volume. As seen in Figure 4.4, the bubbles change shape from spherical ($\kappa < 0.3$) to oblate ($0.3 < \kappa < 0.7$) to prolate

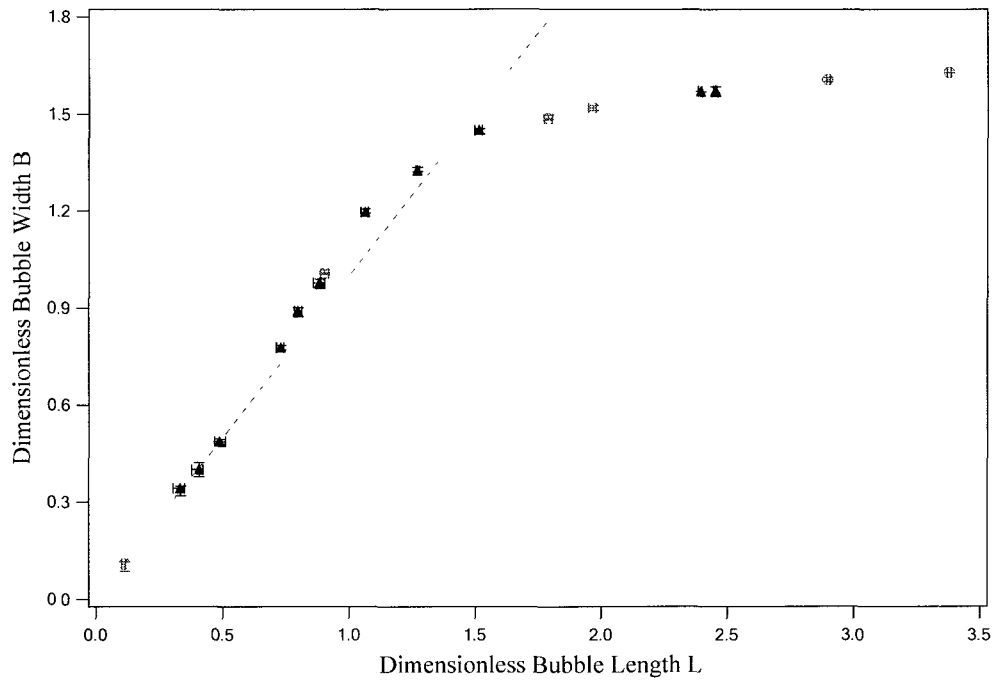


Figure 4.3: Length versus width for bubble rising in 75 wt% glycerol water solution in 10×10 mm square channel (2-G). The dashed line represents $L = B$ line. The open symbols correspond to the bubble shapes presented in Figure 4.1.

($\kappa > 0.7$) ones with increasing bubble sizes in agreement with Bhaga and Weber [4]. Figure 4.5 displays the dimensionless film thickness, δ , as a function of bubble size for results shown in Figures 4.1 - 4.4. As seen in Figure 4.5, the film thickness decreases with increase in bubble size and seems to reach a constant value for long bubbles consistent with the results of Bretherton [7]. Figures 4.3 - 4.5 show that the error in

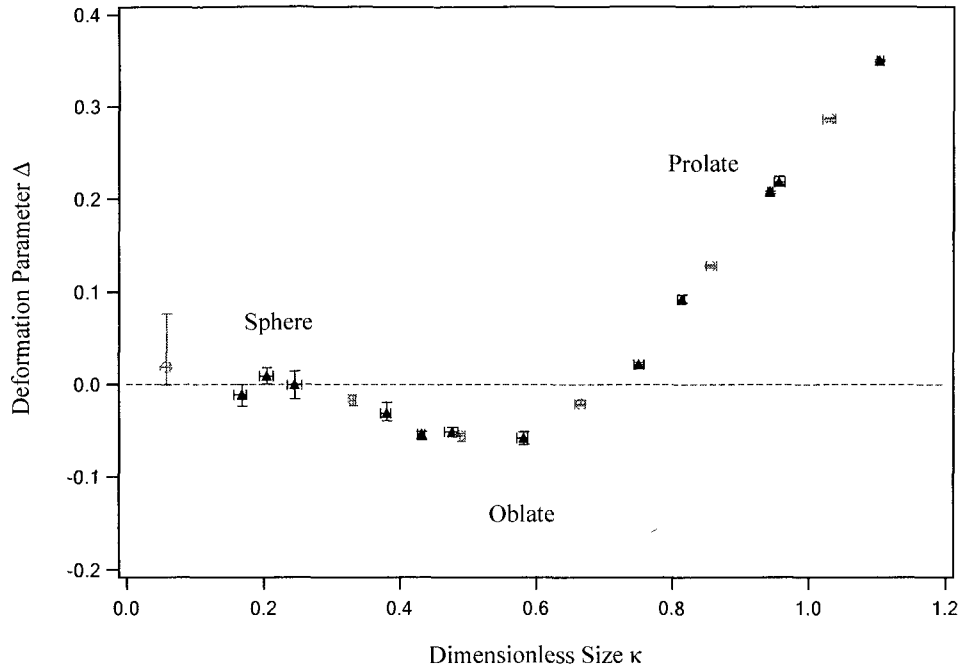


Figure 4.4: Deformation parameter as a function of dimensionless bubble size for bubble rising in 75 wt% glycerol water solution in 10×10 mm square channel (2-G). The open symbols correspond to the bubble shapes presented in Figure 4.1.

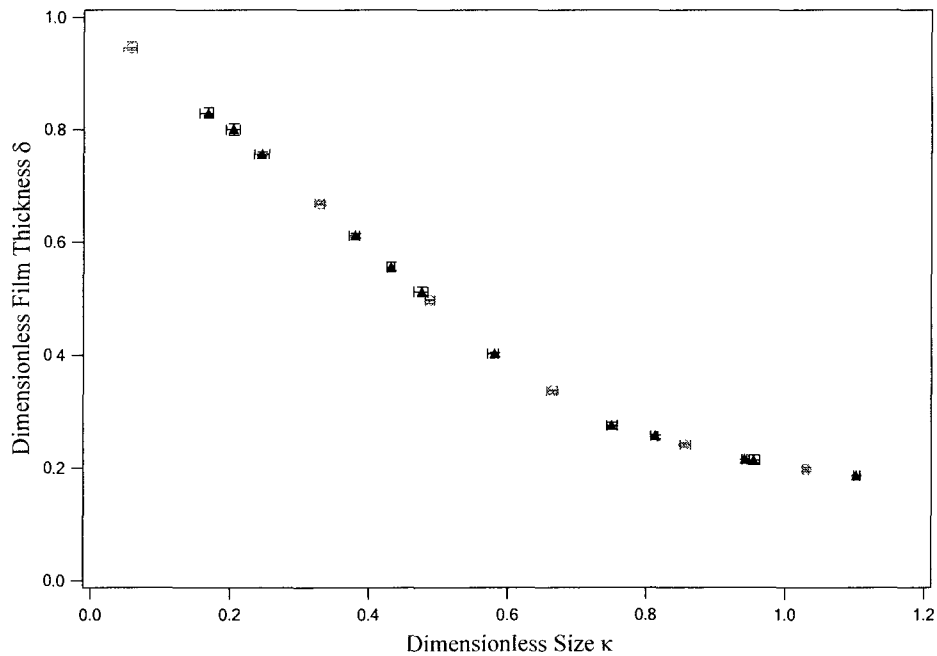


Figure 4.5: Dimensionless film thickness as a function of dimensionless bubble size for bubble rising in 75 wt% glycerol water solution in 10×10mm square channel (2-G). The open symbols correspond to the bubble shapes presented in Figure 4.1.

measuring the shape parameters and the film thickness is small for the entire range of bubble sizes.

The effect of a non-uniform film surrounding the bubble is presented in Figure 4.6 where we compare the dimensionless terminal velocity as a function of dimensionless bubble size obtained for steady bubbles rising in a square and a circular channel with a hydraulic diameter, $D_H = 10\text{mm}$ in the absence of any surfactants. The dimensionless terminal velocity is defined as $U = U_d/U_c$ where $U_c = \Delta\rho g R_c^2 / 3\eta^0$ is the characteristic buoyancy rise velocity. It should be noted that the cross sectional area of a square channel with 10mm side length is larger than the cross sectional area of a circular tube with 10mm diameter. The trend of the velocity-volume curve for the bubbles rising in a square channel is similar to that of the velocity-volume curve for a circular channel. However, the terminal velocities for all bubbles moving in square channel are larger than those in circular channel due to leakage flux at the corners of the channel. The terminal velocity of a long bubble rising in a circular channel is $\approx 23\%$ lower than the velocity of a long bubble rising in a square channel with the same hydraulic radius. A comparison of the shape, the deformation parameter Δ , and the film thickness δ as a function of the bubble size for bubbles rising in 75 wt% glycerol water solution in a circular and square channel with $D_H = 10\text{ mm}$ is shown in Figures 4.7, 4.8, and 4.9 respectively. For small bubble sizes, the bubbles are nearly spherical and unaffected by the shape of the confining walls. For larger bubbles, however, the bubbles in a circular channel are more prolate than bubbles in the square channel as seen in Figures 4.7 and 4.8. Because of the extra cross-

sectional area near the corners of a square channel, the air bubble expands more radially outward in a square channel. As seen in Figure 4.9, the minimum film thickness in a circular channel near the channel walls is larger than that in a square channel. These results are consistent with the experimental observations of Li et al. [23] for bubbles rising in square channels.

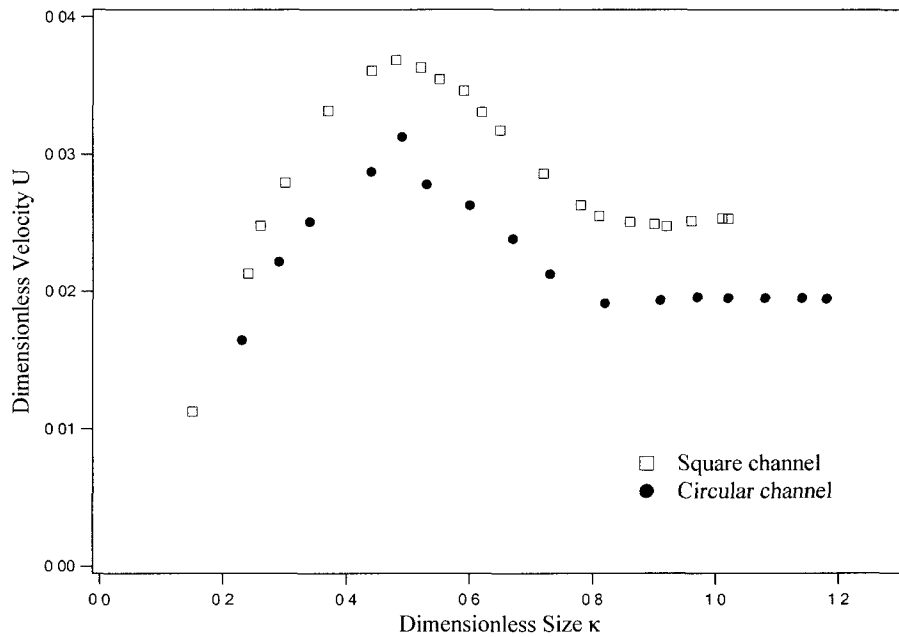


Figure 4.6: Comparison of terminal velocity as a function of bubble size for steady bubbles rising in 75 wt% glycerol water solution in a circular tube (1-G) and square channel (2-G) with $D_H=10\text{mm}$.

4.1.2 Surfactant-laden System

The effects of adding surfactant on the motion and deformation of rising bubbles in Newtonian solution are presented in this section. In the Newtonian bulk solution of 75 wt% glycerol-water solution, various surfactants including nonionic surfactants, Triton X-100

(TX-100) and ionic surfactants, sodium dodecyl sulfate (SDS) and Aerosol-OT (AOT) were added at different concentrations. These surfactants are all water soluble surfactants.

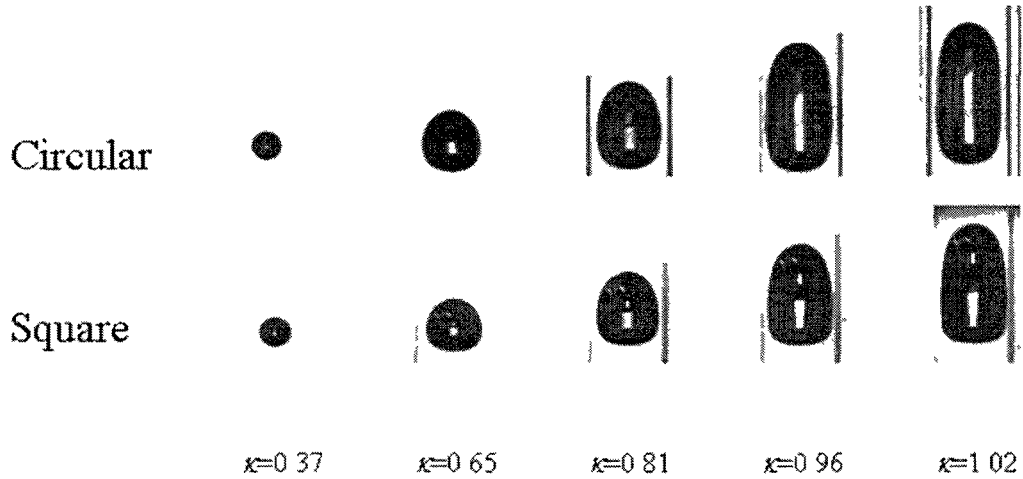


Figure 4.7: The bubble shapes corresponding to different bubble terminal velocity as a function of bubble size for 75 wt% glycerol water solution in a circular tube (1-G) and square channel (2-G) with $D_H=10\text{mm}$.

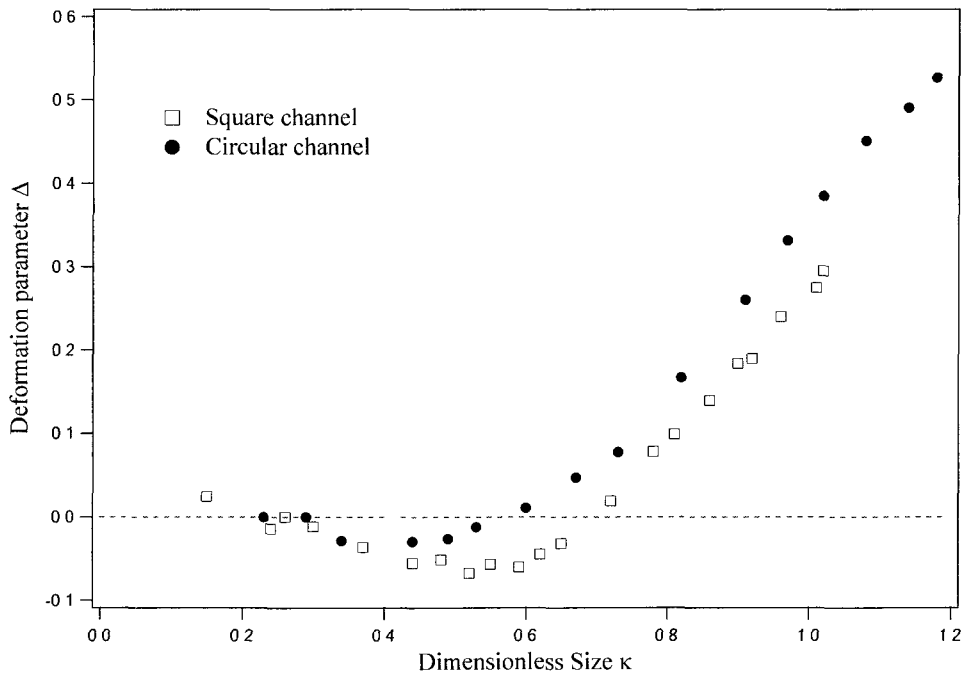


Figure 4.8: Comparison of deformation parameter for steady bubbles rising in 75 wt% glycerol water solution in a circular tube (1-G) and square channel (2-G) with $D_H=10\text{mm}$.

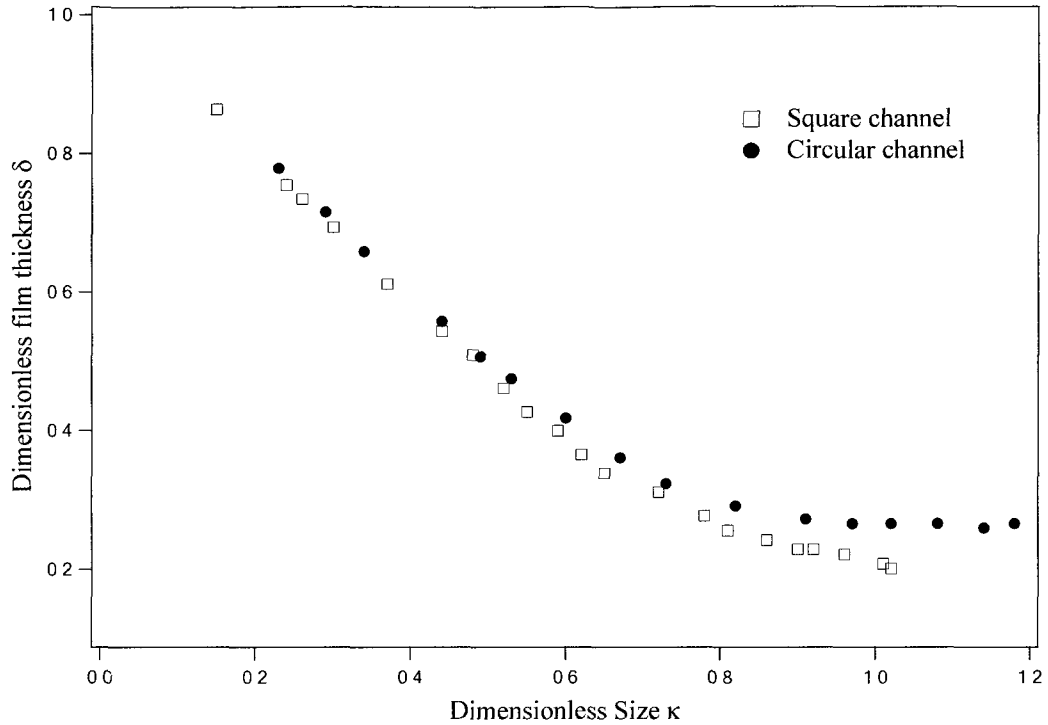


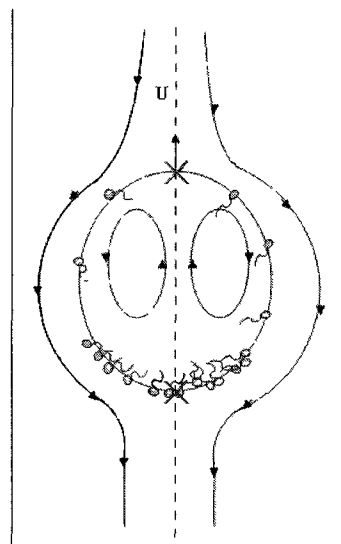
Figure 4.9: Comparison of film thickness as a function of bubble size for steady bubbles rising in 75 wt% glycerol water solution in a circular tube (1-G) and square channel (2-G) with $D_{ff}=10\text{mm}$.

While most of the experiments were conducted at bulk concentrations below the critical micellar concentration (CMC), experiments were also conducted above CMC for Triton X-100 and this section is divided into two subsections: results below CMC and results above CMC.

4.1.2.1 Surfactant Concentrations Below CMC

For the results presented in this section, the concentrations used here are all below critical micelle concentration (CMC), which indicates that all surfactant molecules are present in the monomer forms. A schematic of the flow around a rising bubble in the presence of

surfactants is shown in Figure 4.10. In the absence of surfactants and at low bubble speeds, the flow around the bubble diverges at the leading end of the bubble and then converges at the trailing end of the bubble. The bubble interface moves from the front end of the bubble to the trailing end of the bubble. There are two stagnation points on the bubble surface at the front and rear of the bubbles as shown in Figure 4.10. The magnitude of the surface velocity determines the overall terminal velocity of the bubble.



×:Stagnation point

Figure 4.10: Schematic of a bubble rising in a channel in the presence of surfactants.

In surfactant-contaminated systems, surfactants adsorb at the front end of the bubble, are transported along the interface due to surface convection and diffusion, and desorb at the rear end of the bubble. Adsorbed surfactants tend to accumulate near the stagnation point at the trailing pole as there is converging flow at this end as shown in Figure 4.10. At steady state, a surface tension gradient is established along the interface due to the

nonuniform distribution of surfactants. The surface tension is higher at the leading end and lower at the trailing end of the bubble. The interface pulls toward the high tension region at the front end of bubble, exerting a Marangoni stress along the interface and retarding the surface velocity of the bubble. This in turn lowers the terminal velocity of the rising bubble [15].

For very small quantities of surfactants added to the fluid system, the equilibrium surface tension remains essentially unchanged. For example, the equilibrium surface tension does not change after adding 1ppm AOT (from 65 to 64 mN/m) and 1 ppm TX-100 (from 65 to 58 mN/m) in 75 wt% glycerol water solution (see Figures 3.7 and 3.8). However, as bubbles move through these low concentration surfactant solutions, their terminal velocity can change due to non-equilibrium effects. Figure 4.11 shows the dimensionless terminal velocity as a function of dimensionless bubble size for bubble rising in 75 wt% glycerol water solution with 1 and 10 ppm of AOT in 10mm × 10mm square channel. For comparison, the corresponding velocity-volume curve in the absence of surfactants is also shown on the same graph. As seen in Figure 4.11, the general shape of the velocity-volume curve in the presence of surfactants is similar to the velocity-volume curve for surfactant-free system. However, the terminal velocities of small bubbles in low concentration surfactant solutions is lower than similar sized bubbles in surfactant-free solutions due to Marangoni effect as described earlier. The terminal velocity for long bubbles does not seem to be affected by the presence of small amounts of surfactants. A similar reduction in mobility is seen for small additions of the nonionic surfactant, TX-100 in the same channel geometry (see Figure 4.12) as well as in a rectangular geometry

(see Figure 4.13). Further increase of the surfactant concentration but below CMC value enhances the Marangoni effect as seen in Figure 4.11. As the bulk concentration of AOT in the 75 wt% glycerol-water solution is increased to 10 ppm, the terminal velocity of small as well as large bubbles reduces.

Increasing the AOT concentration further to 100 ppm in the 10 mm square channel filled with 75 wt% glycerol water solution results in a velocity volume curve as shown in Figure 4.14. The velocity-volume curves for 0 ppm and 10 ppm AOT concentrations are shown for comparison. The dimensionless terminal velocity for small bubbles in 100 ppm AOT solution is lower than the corresponding bubbles in 0 ppm and 10 ppm AOT solutions as expected due to the increased Marangoni effect. The terminal velocity increases with bubble volume initially, reaches a peak at $\kappa \sim 0.5$ and then starts decreasing again till $\kappa \sim 0.57$. Beyond this bubble size, the bubble velocity increases again, reaches a second peak at $\kappa \sim 0.75$ and then reduces again to reach the terminal velocity for long bubbles. The long bubble velocity in the 100 ppm AOT solution is less than the long bubble velocities in 0 ppm and 10 ppm AOT solutions. To the best of our knowledge, the existence of two peaks in the velocity-volume curve has not been reported to date. The deformation parameter, Δ as a function of drop size, κ for the bubbles rising in 0 ppm, 10 ppm, and 100 ppm AOT solutions in 10 mm square channel is shown in Figure 4.15. For small bubble sizes ($\kappa < 0.9$), the bubbles become more prolate as the surfactant concentration increases. This can also be seen in the comparison of bubble shapes in the three surfactant solutions for $\kappa_{\text{avg}} \sim 0.26, 0.63, \text{ and } 0.76$ in

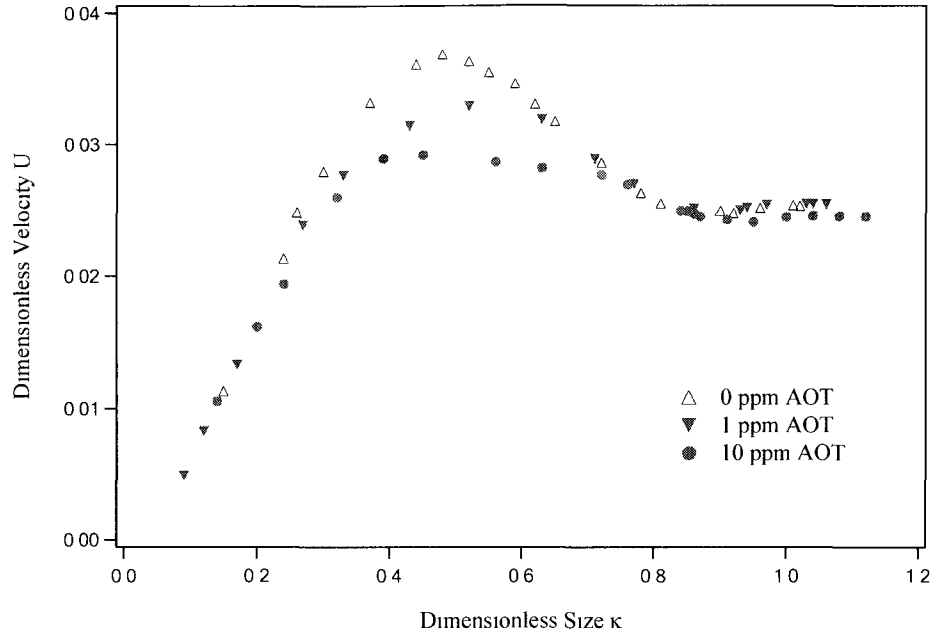


Figure 4.11: The terminal velocity as a function of bubble size for bubble rising in 75 wt% glycerol water solution at low concentrations of AOT in 10mm \times 10 mm square channel.

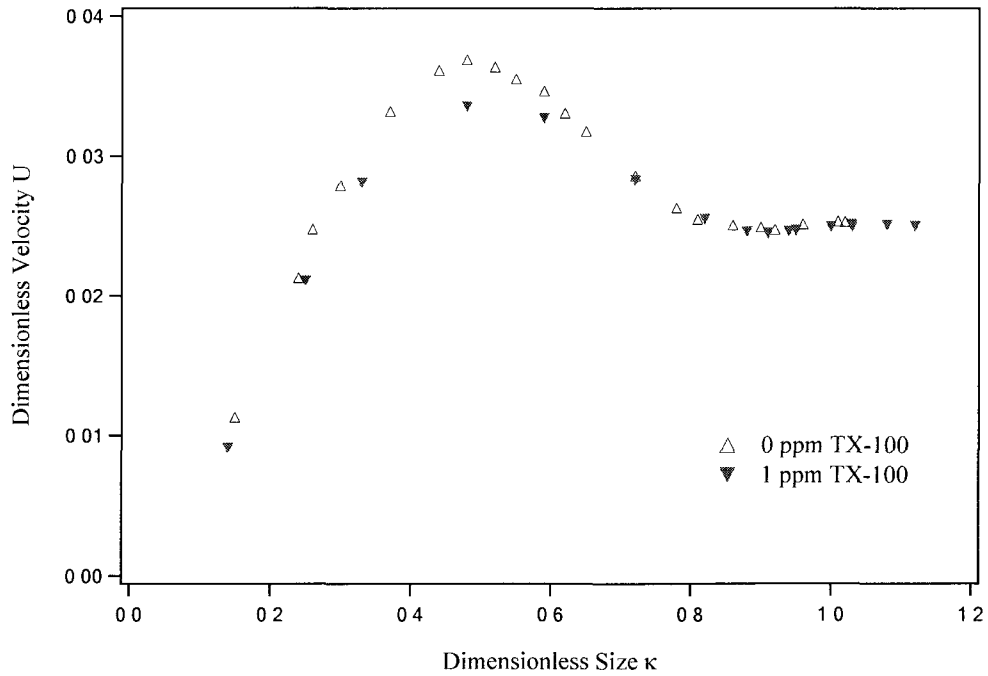


Figure 4.12: The terminal velocity as a function of bubble size for bubble rising in 75 wt% glycerol water solution with tiny amount of TX-100 in 10mm \times 10 mm square channel.

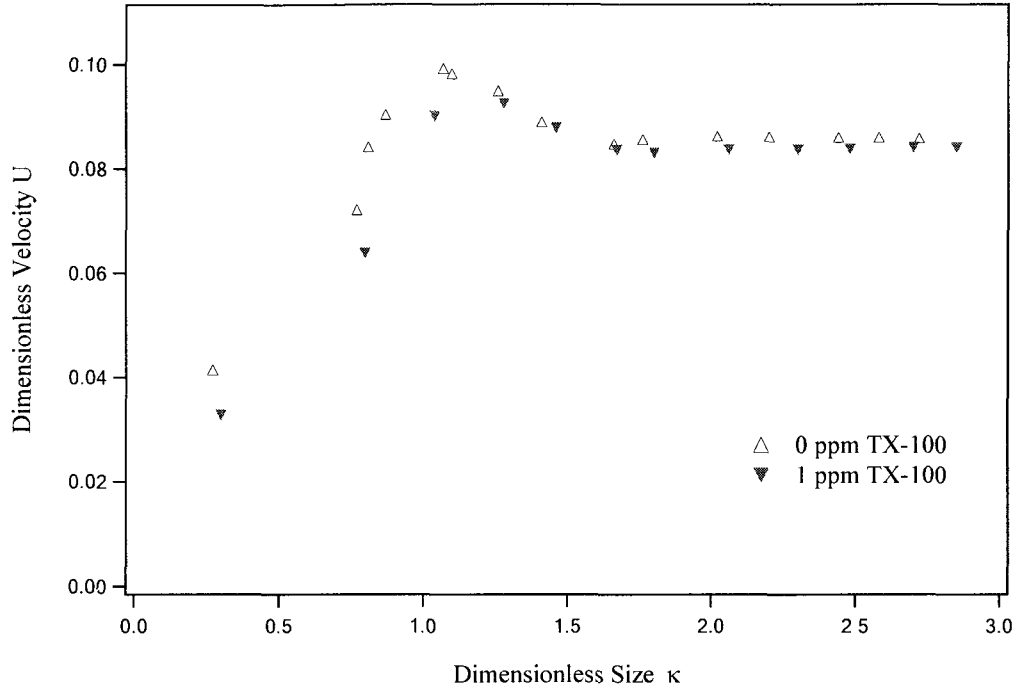


Figure 4.13: The terminal velocity as a function of bubble size for bubble rising in 75 wt% glycerol water solution with tiny amount of TX-100 in 16mm \times 3 mm rectangular channel.

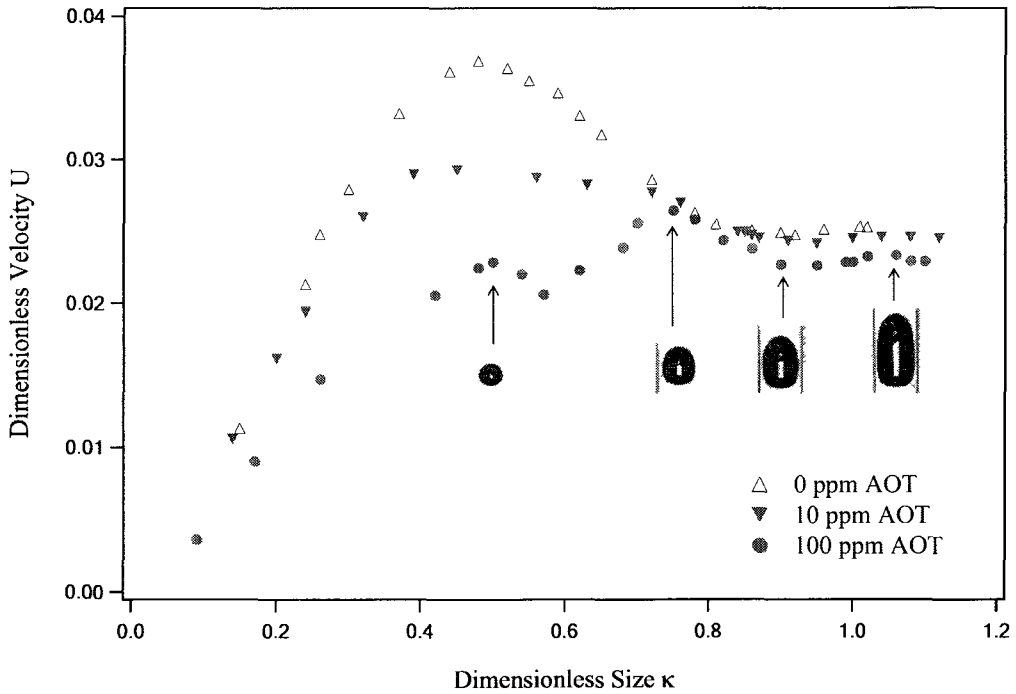


Figure 4.14: The terminal velocity as a function of bubble size for bubbles rising in 75 wt% glycerol water solution with various concentration (below CMC) of AOT in 10mm \times 10 mm square channel.

Figure 4.16. Please note that the volumes of the bubbles for the three surfactant concentration solutions are not identical and variation of upto ± 0.02 in κ exists. The shape of the front of the bubble is nearly identical for all the bubbles in different AOT concentration solutions. The rear of the bubbles is more flat for bubbles in the 0 ppm solution as compared to the 100 ppm solutions. It is interesting that the more prolate bubbles at the higher surfactant concentrations rise at lower speeds as compared to less prolate bubbles at the lower concentrations. This is due to the presence of surfactants that accumulate at the rear of the bubble as shown in Figure 4.10. Increased surfactant concentration at the rear of the bubble reduces the surface tension locally. A normal stress jump across the interface requires that as the surface tension decreases, the curvature must increase locally to maintain the same pressure drop across the interface. Thus, the bubbles moving through higher concentration surfactant solutions have a more curved interface at the rear compared to bubbles travelling in solutions in the absence of surfactants resulting in more prolate shapes. However, the accumulation of surfactants at the rear of the interface also renders the interface immobile in this region reducing the circulation within the bubble and the terminal velocity of the bubble. The deformation parameter for larger bubbles ($\kappa > 0.9$) at different concentrations are similar. Double peaks in the velocity-volume curve at relatively high concentrations of surfactants (below CMC) were observed in our experiments for drops rising in solutions containing Triton-X100 in 10 mm square channels (see Figure 4.17), 15 mm square channels (see Figure 4.18), and 16 mm x 3 mm rectangular channels (see Figure 4.19). For bubbles rising in TX-100 solutions in a 16 mm x 3 mm rectangular channel (Figure 4.19), the terminal

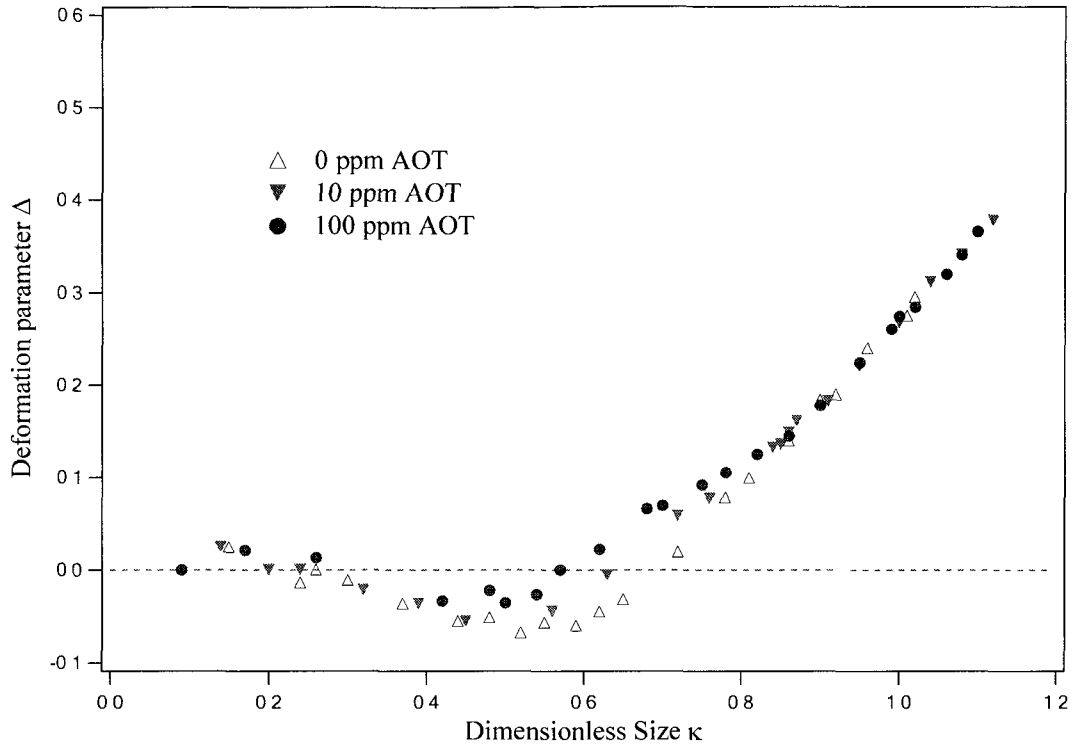


Figure 4.15: Comparison of deformation parameter for steady bubbles rising in 75 wt% glycerol water solution with various concentration (below CMC) of AOT in a square channel with $D_H=10\text{mm}$.

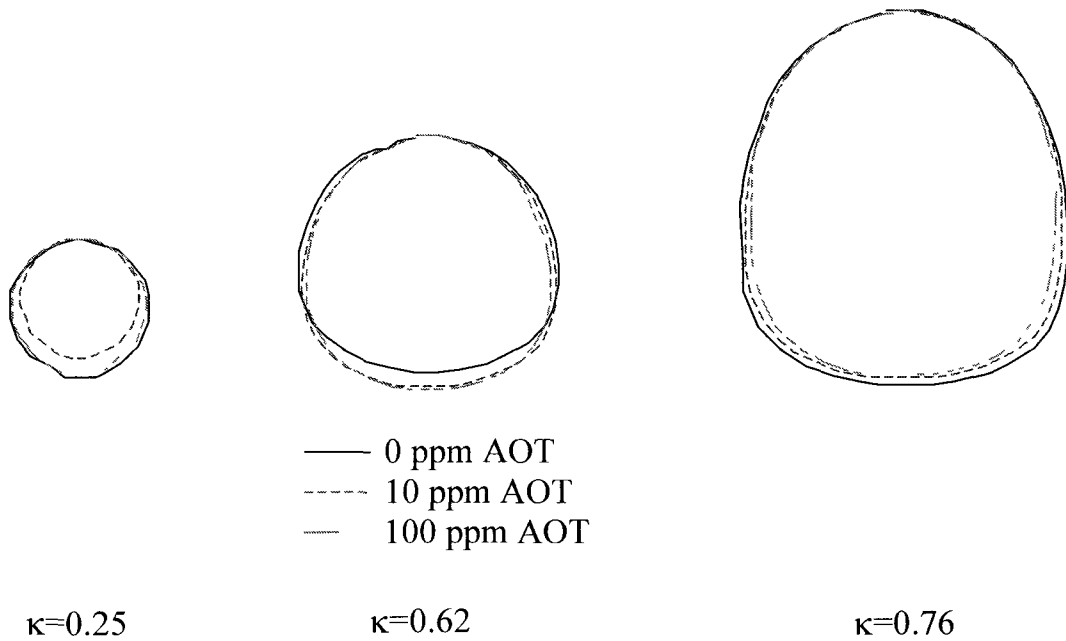


Figure 4.16: Shape comparison for steady bubbles rising in 75 wt% glycerol water solution with various concentration (below CMC) of AOT in a square channel with $D_H=10\text{mm}$.

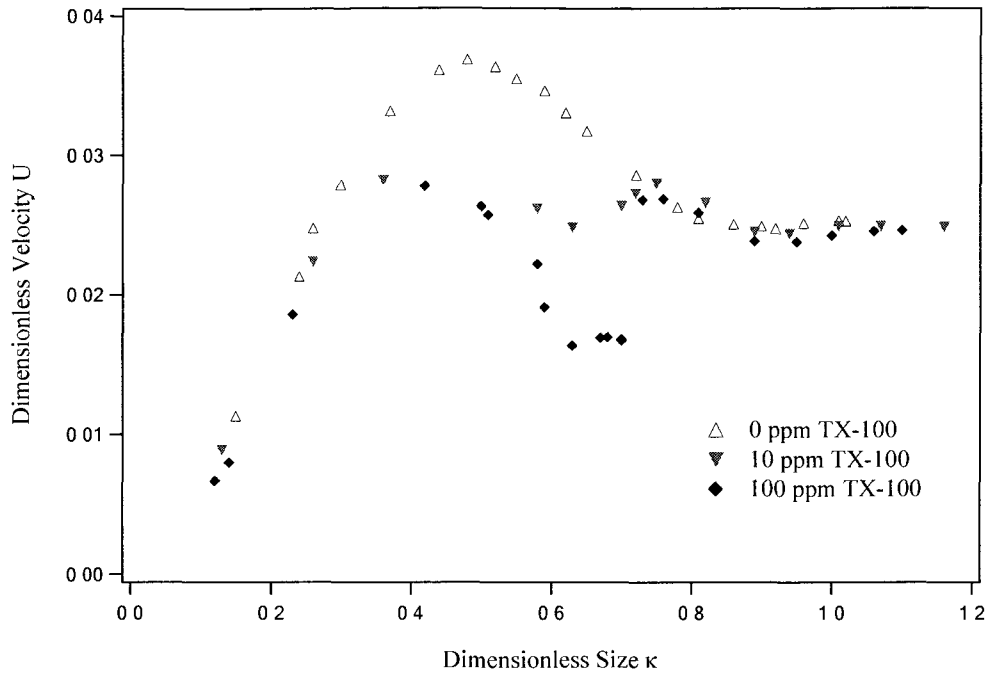


Figure 4.17: The terminal velocity as a function of bubble size for bubbles rising in 75 wt% glycerol water solution with various concentration (below CMC) of TX-100 in 10mm \times 10 mm square channel.

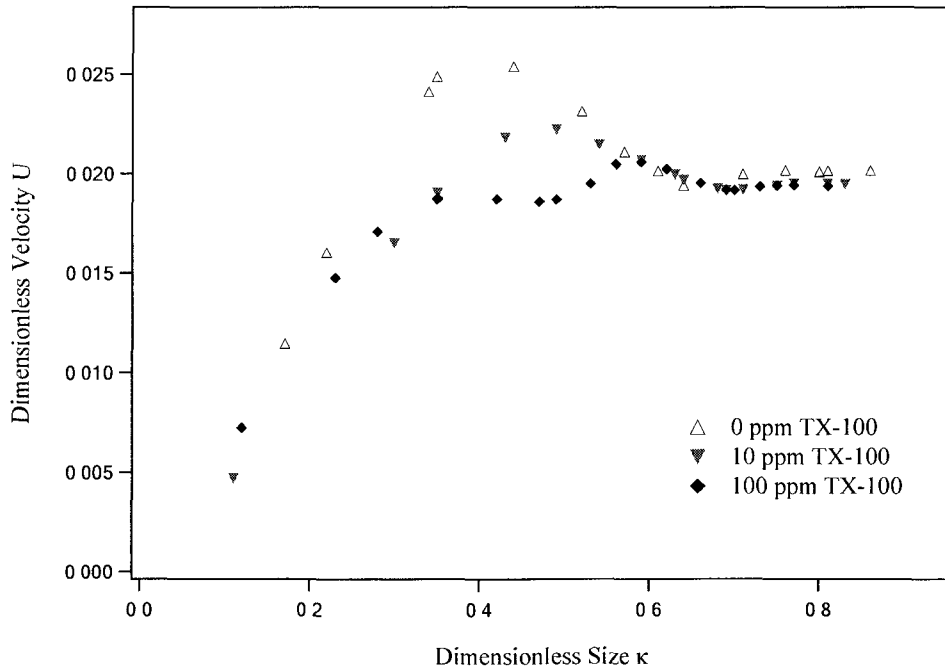


Figure 4.18: The terminal velocity as a function of bubble size for bubbles rising in 75 wt% glycerol water solution with various concentration (below CMC) of TX-100 in a 15 mm square channel.

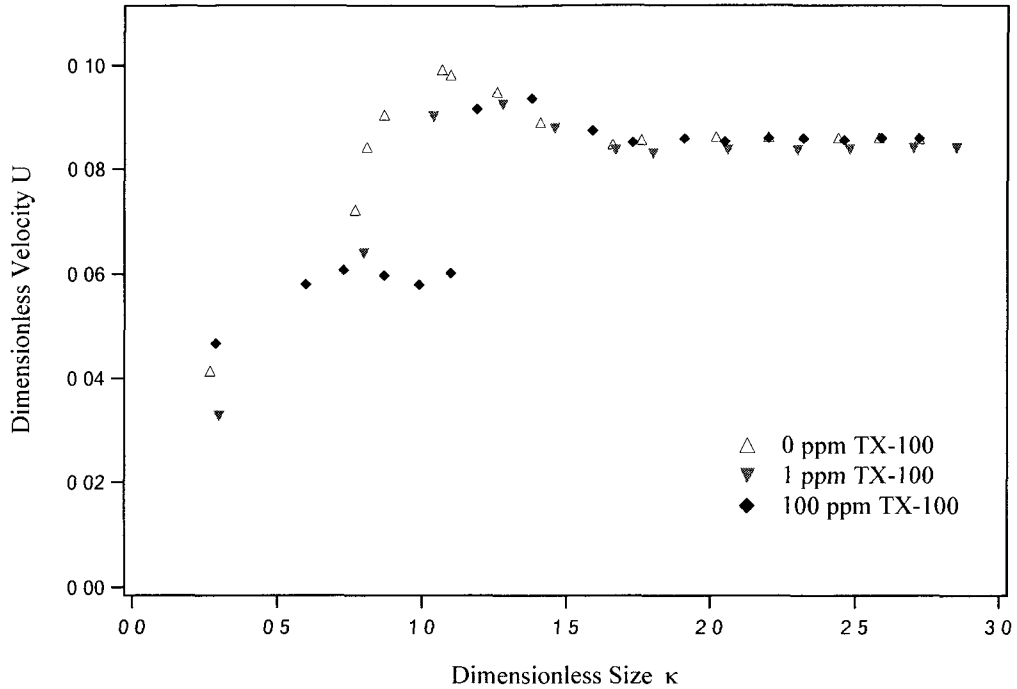


Figure 4.19: The terminal velocity as a function of bubble size for bubbles rising in 75 wt% glycerol water solution with various concentration (below CMC) of TX-100 in 16mm \times 3 mm rectangular channel.

velocity of long bubbles in the 100 ppm TX-100 solution is the same as the terminal velocity of long bubbles in the 0 ppm solution.

The effect of a non-uniform film surrounding the bubble on the velocity and shape of the rising bubbles with surfactants is presented in Figures 4.19 – 4.22 for a 16 mm \times 3 mm rectangular channel and in Figures 4.23 and 4.24 for a square and circular channel with $D_H = 10$ mm. In a rectangular channel, the bubble takes on a pancake like shape as shown in the schematic in Figure 3.14(e). As the bubble rises through the channel, fluid flows along the sides of the bubble as well as in the thin fluid film separating the bubble from the walls as shown in Figure 4.19. The bubble shape is not axisymmetric and the

distribution of surfactant at the rear of the bubble depends on the magnitude of the flow along the sides and the thin film. As a result, the shapes of bubbles as bubble size increases shows trends not seen in bubbles rising through square and circular channels where the bubble shapes are axisymmetric. Figures 4.21 and 4.22 show the deformation parameter as a function of bubble size and images of shapes realized in a 16 mm \times 3 mm rectangular channel for 0 ppm, 1 ppm, and 100 ppm TX-100 solutions. In the absence of surfactants, the bubbles are nearly spherical and as the bubble size increases ($\kappa > 1.5$) the bubbles become prolate. As small amount of surfactant (1 ppm TX-100) is added, the bubbles become prolate up to $\kappa \sim 1.0$ beyond which the bubbles become more spherical in shape till $\kappa \sim 1.5$. For larger bubbles ($k > 1.5$), the bubbles again become prolate in shape. However, even in the presence of very small amount of surfactant, bubble shapes are more prolate in the surfactant solution than in the clean solution. The effect of increased curvature in the presence of surfactants is enhanced at low surfactant concentrations due to the stronger flow in the thin film region across the depth of the channel. As the surfactant concentration is increased to 100 ppm TX-100, the bubble shapes become oblate for bubbles with $\kappa < 1.1$ where the bubble shape suddenly becomes very prolate and then continues to remain prolate for long bubbles similar to the surfactant-free case. It is not clear why the bubble shape changes suddenly and more detailed data need to be taken in this region to draw any conclusions.

Figure 4.23 compares the velocity-volume curve obtained for steady bubbles rising in a square and a circular channel with hydraulic diameter, $D_H = 10\text{mm}$ filled with 10ppm

Triton X-100 in 95 wt% glycerol-water solution (1-TG-e and 2-TG-e). The cross sectional area of a square channel with 10mm side length is larger than the cross sectional area of a circular tube with 10mm diameter. The shape of the velocity-volume curve for bubbles rising in a square and circular channel is similar showing the presence of two peaks. However, as seen in the absence of surfactants, the terminal velocity of long bubbles rising in a circular channel is $\approx 21\%$ lower than the velocity of long bubbles rising in a square channel with the same hydraulic radius. This is due to the leakage flux at the corners of the square channels, which allows the bubbles to expand more radially outward. As a result, the bubbles are more elongated in circular channels as compared to square channels (see Figure 4.24).

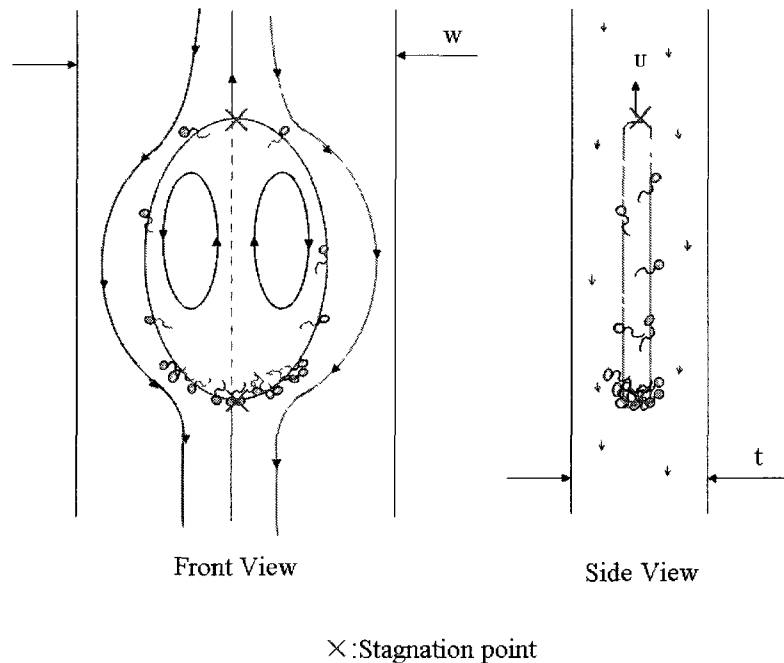


Figure 4.20: Schematic of the flow pattern around a bubble rising in a rectangular channel with width w and depth t .

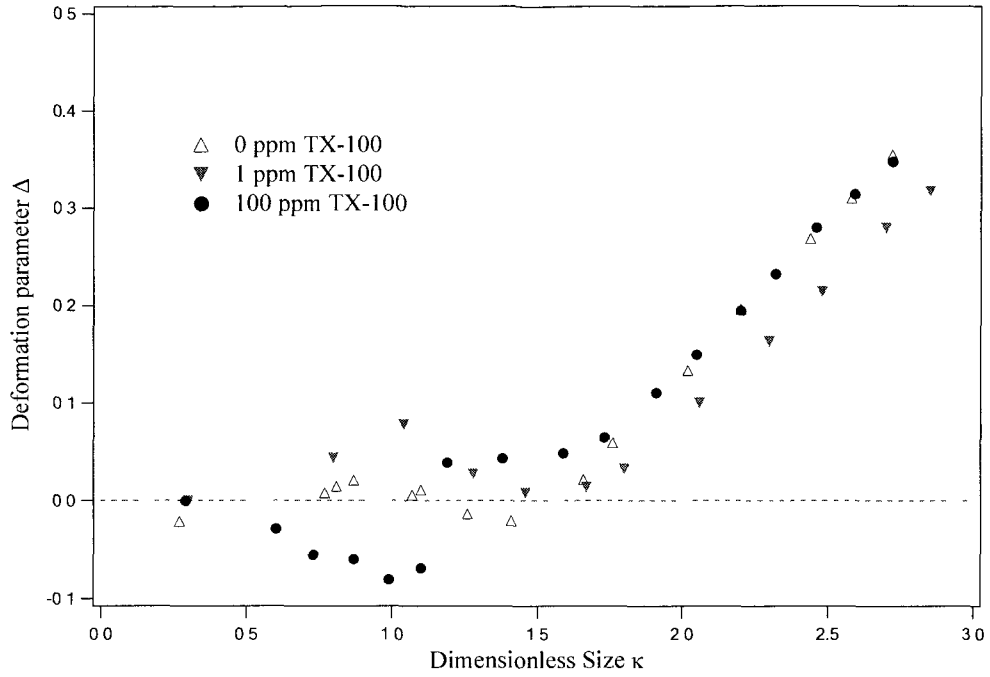


Figure 4.21: Comparison of deformation parameter for steady bubbles rising in 75 wt% glycerol water solution with various concentration (below CMC) of TX-100 in a 16mm \times 3mm rectangular channel.

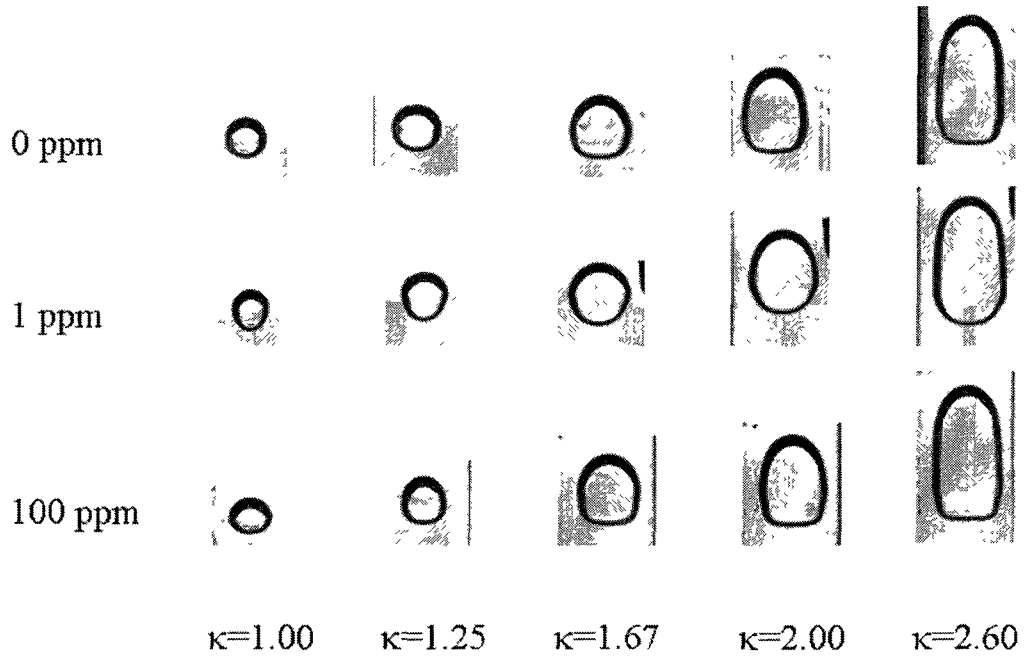


Figure 4.22: Shape comparison for steady bubbles rising in 75 wt% glycerol water solution with various concentration (below CMC) of TX-100 in a 16mm \times 3mm rectangular channel.

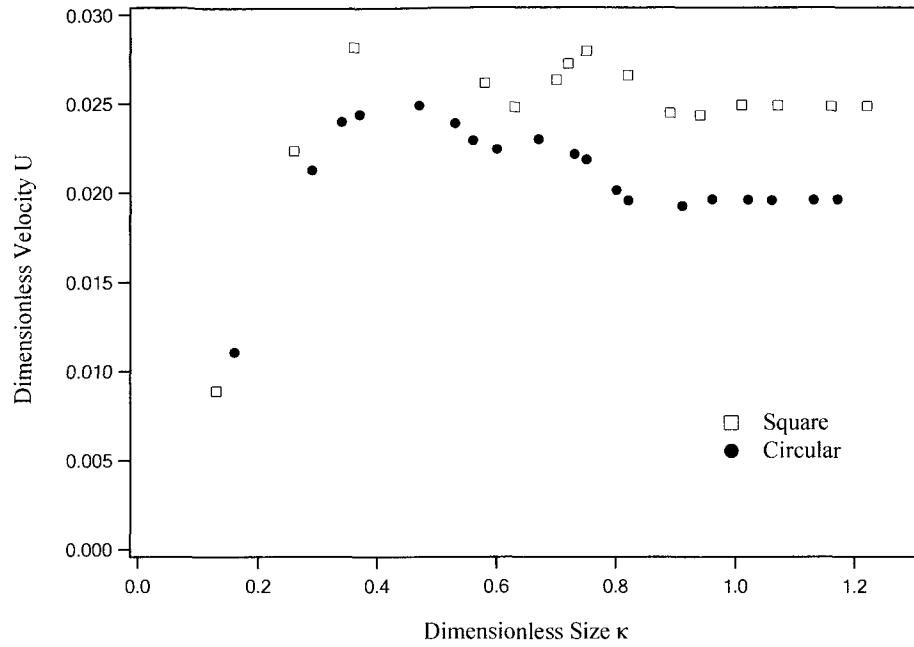


Figure 4.23: The terminal velocity as a function of bubble size for bubble rising in 75 wt% glycerol water solution with 10 ppm Triton X-100 in a circular tube (1-TG-e) and square channel (2-TG-e) with $D_H=10\text{mm}$.

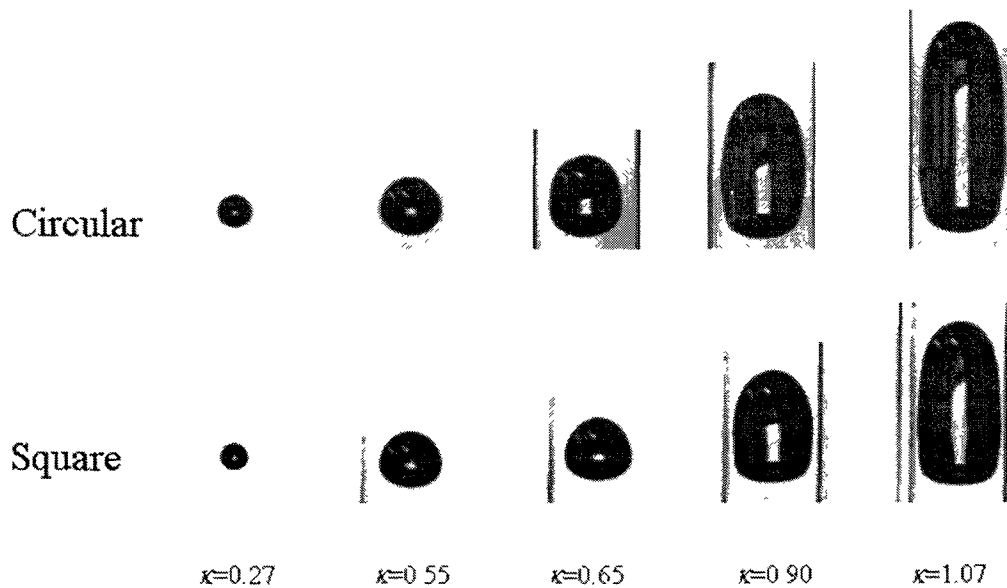


Figure 4.24: The bubble shapes corresponding to different bubble terminal velocity as a function of bubble size for 75 wt% glycerol water with 10 ppm of TX-100 in a circular tube (1-TG-e) and square channel (2-TG-e) with $D_H=10\text{mm}$.

4.1.2.2 Surfactant Concentrations Above CMC

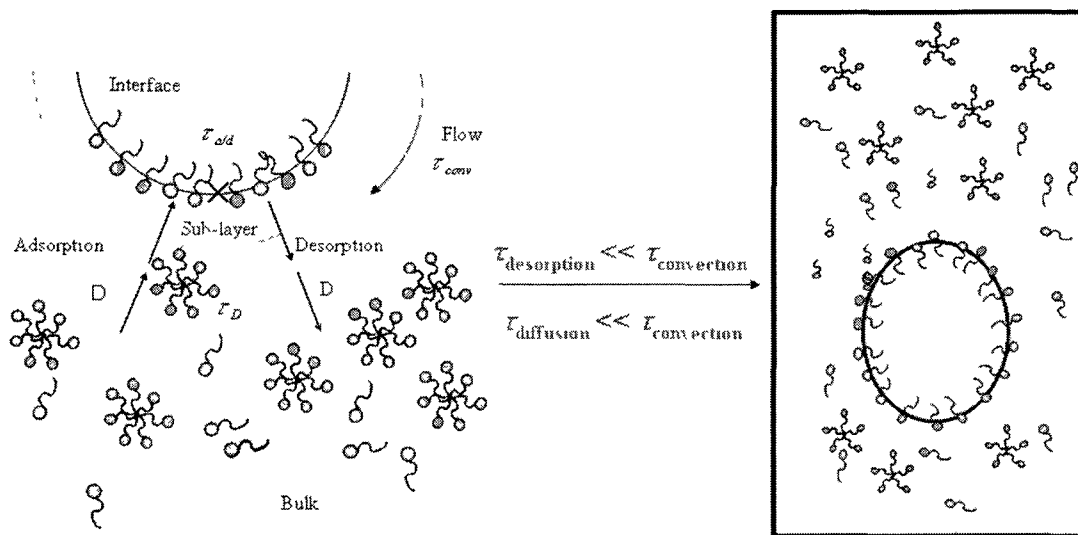


Figure 4.25: Schematic of surfactant concentration above CMC

When surfactants are present at concentrations above the critical micellar concentration (CMC), surfactant molecules self assemble to form aggregates (micelles) in solution. As the bulk concentration of the surfactant is increased, the concentration of the aggregates increases while the monomer concentration in equilibrium with the micelles remains the same and any added surfactant is mostly added to the micelles [28]. The equilibrium is a dynamic one in that as the monomer concentration changes, aggregates either break down or reassemble to return to the critical micellar concentration. Even above the CMC concentration, surfactants adsorb at the interface in monomer form. The surfactants adsorbed on the moving bubble interface accumulate at the rear end of the bubble due to convection. This increases the surfactant concentration at the rear of the bubble. Surfactants get desorbed from the interface to the sublayer from where the surfactant

diffuses away to the bulk. In the bulk, the monomer - micelle equilibrium is disturbed and aggregates form to restore the monomer concentration. Stebe et al. [9, 40] reported that the movement of the interface can remain unretarded if, relative to the convective rate along the interface, desorption rate of the surface-active molecules is fast and the bulk concentration is high enough so that diffusion away from the interface is fast. In this manner, a uniform surface concentration of surfactant is maintained and surface tension gradients are removed, restoring interfacial mobility, which is shown in Figure 4.25.

When surfactant concentration is raised to values above the CMC, remobilization of the interface is observed. This is seen clearly in Figure 4.26 where the terminal velocity is plotted as a function of bubble size for bubble rising in 75 wt% glycerol-water solution with concentration of TX-100 above CMC (1000ppm) in a 10 mm × 10 mm square channel. For comparison, the velocity-volume curve in the absence of surfactant (0 ppm) and 100 ppm TX-100 is also plotted on the same graph. As seen in Figure 4.26, the terminal velocity of long bubbles with 1000 ppm TX-100 is the same as that for long bubbles rising in a clean 75 wt% glycerol water solution. For small bubbles, however, complete remobilization is not seen. The velocity-volume curve for bubbles rising in 1000 ppm TX-100 solution shows two peaks but are more mobile than the bubbles rising in the 100 ppm TX-100 solution. The bubbles rising in the 1000 ppm TX-100 solution are more oblate than the bubbles rising in a 0 ppm solution at small bubble sizes as seen in Figure 4.27. This is opposite to all our observations in surfactant solutions below CMC where bubbles became more prolate with the addition of surfactants. A look at the

shape of the bubbles rising in the 1000 ppm solution (see Figure 4.28) shows a distinct bell-like shape at the rear of the bubble, specifically for bubbles with $\kappa < 0.8$ rising in the 1000 ppm TX-100 solution. The shape and deformation of long bubbles remains largely unaffected by the presence of surfactants above CMC. A similar remobilization of long bubbles is seen in Figure 4.29 for bubbles rising in a 15 mm x 15 mm channel with TX-100 solutions above CMC.

For bubbles rising in a TX-100 solutions in a 16 mm x 3 mm rectangular channel remobilization of long bubbles is seen for bubbles rising in a 1000 ppm TX-100 solution (above CMC). This is seen clearly in Figure 4.30 where the dimensionless velocity is plotted as a function of bubble size for bubbles rising in 0 ppm and 1000 ppm TX-100 solutions. However, for bubbles rising in a 500 ppm TX-100 solution (above CMC), the bubble terminal velocity is retarded for the entire range of bubble sizes studied. It is not clear whether this is a feature seen only in a rectangular channel geometry as we do not have data for bubbles rising in 500 ppm TX-100 solution in a 10 mm x 10 mm square channel. A comparison of the deformation parameter as a function of bubble size for bubbles rising in 0 ppm, 500 ppm, and 1000 ppm TX-100 solution is seen in Figure 4.31. For bubbles rising in a 500 ppm TX-100 solution, the bubbles are oblate at small bubble sizes and then become prolate at large bubble sizes. The bubbles in 500 ppm TX-100 solution are more prolate than bubbles in the absence of surfactants. This is also seen clearly in Figure 4.32 where bubbles in 500 ppm TX-100 solution have a more curved interface at the rear of the bubble. As the surfactant concentration increases to 1000 ppm,

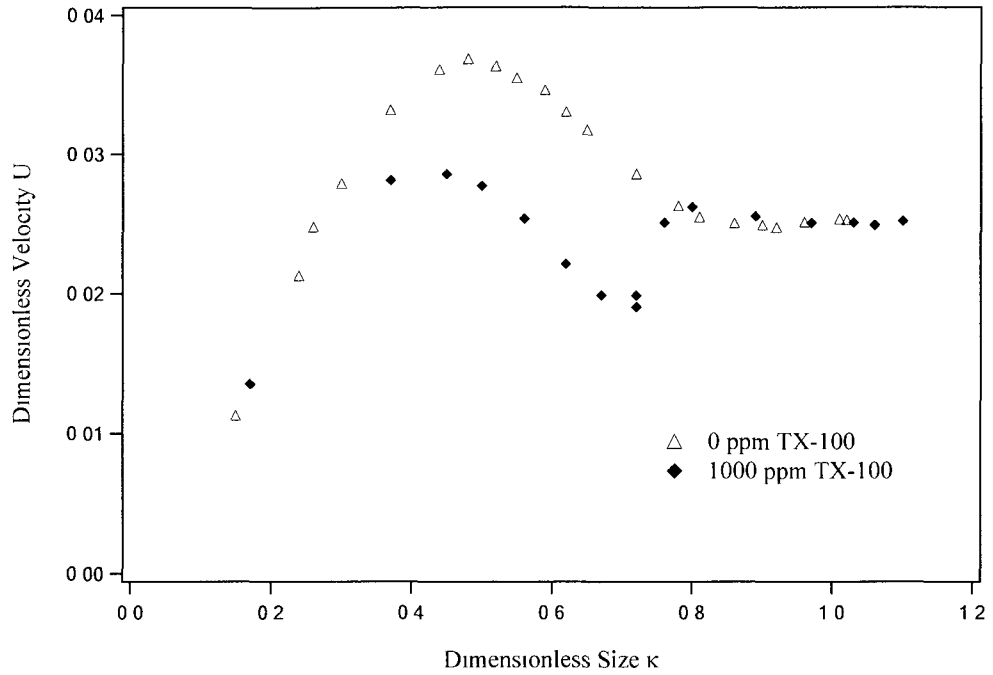


Figure 4.26: The terminal velocity as a function of bubble size for bubbles rising in 75 wt% glycerol water solution with various concentration (below CMC) of TX-100 in 10mm \times 10 mm square channel.

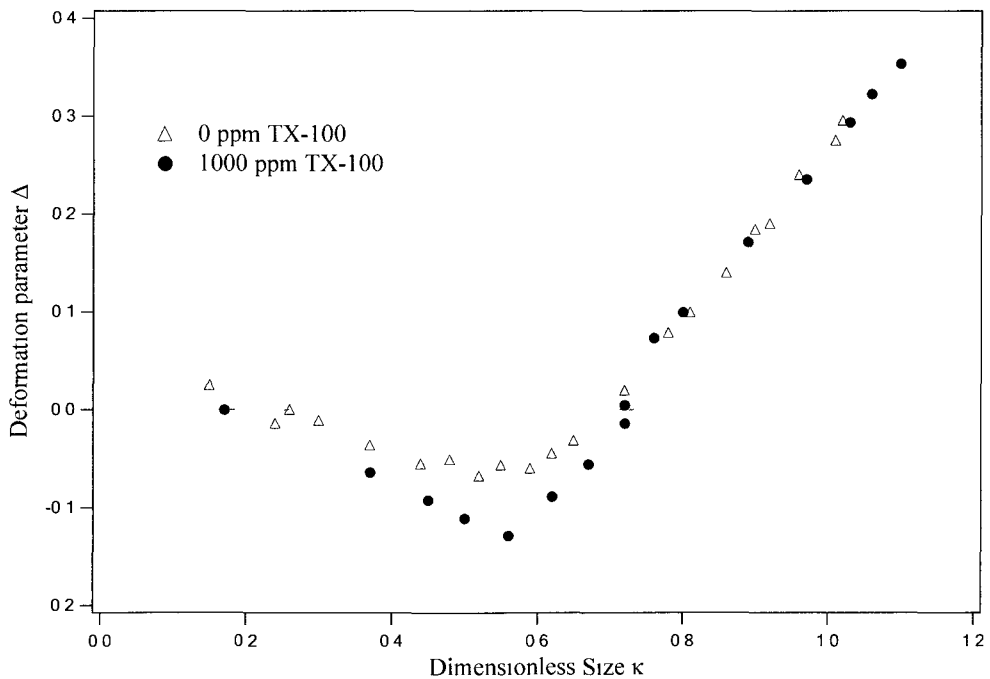


Figure 4.27: Comparison of deformation parameter for steady bubbles rising in 75 wt% glycerol water solution with various concentration (below CMC) of TX-100 in a square channel with $D_H=10\text{mm}$.

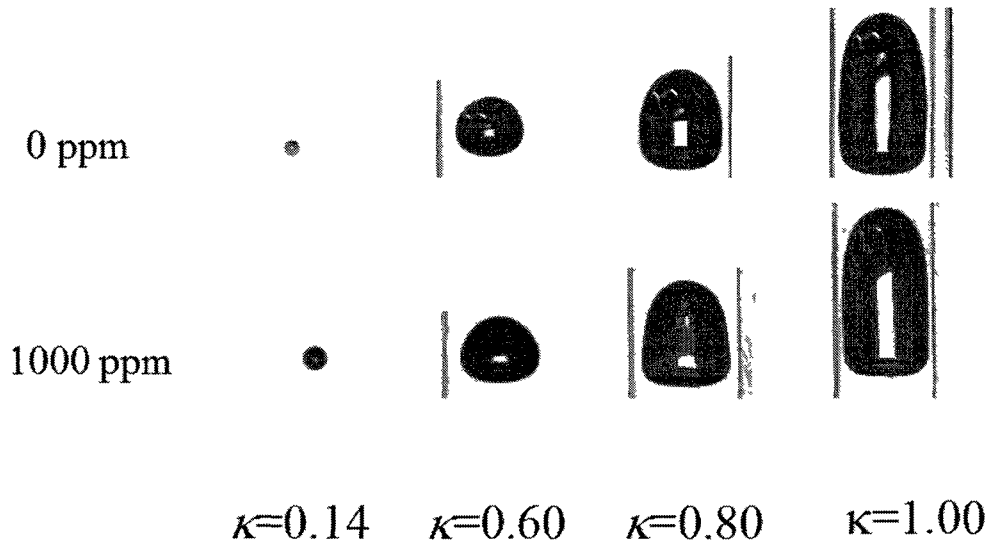


Figure 4.28: The bubble shapes corresponding to different bubble terminal velocity as a function of bubble size for 75 wt% glycerol water with 10 ppm of TX-100 in a square channel with $D_H=10\text{mm}$.

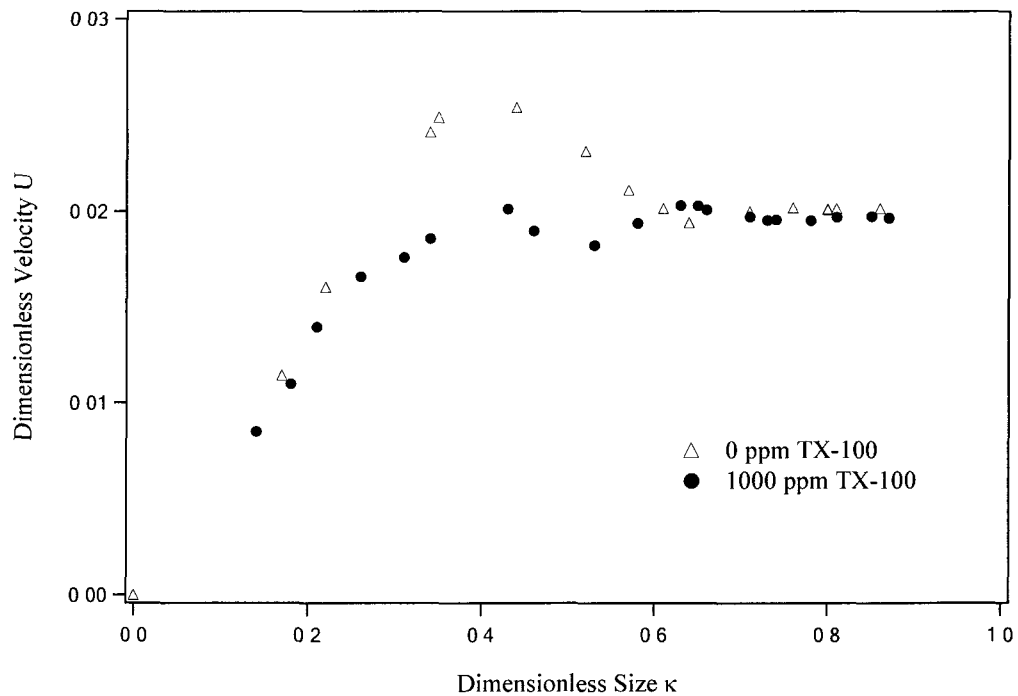


Figure 4.29: The terminal velocity as a function of bubble size for bubble rising in 75 wt% glycerol water solution with various concentration of TX-100 in $15\text{ mm} \times 15\text{ mm}$ square channel.

the bubbles again become flat at the rear end. Very small as well as very large bubbles in a 1000 ppm surfactant solution are more oblate than bubbles rising in a clean solution. Based on our discussion in Section 4.1.2.1 we expect the bubble behavior in a rectangular channel to be different from dynamics in a square and circular channel due to the non-axisymmetric shape of the bubble. However, more experiments are necessary to confirm the changes in trends observed in Figures 4.30 - 4.32.

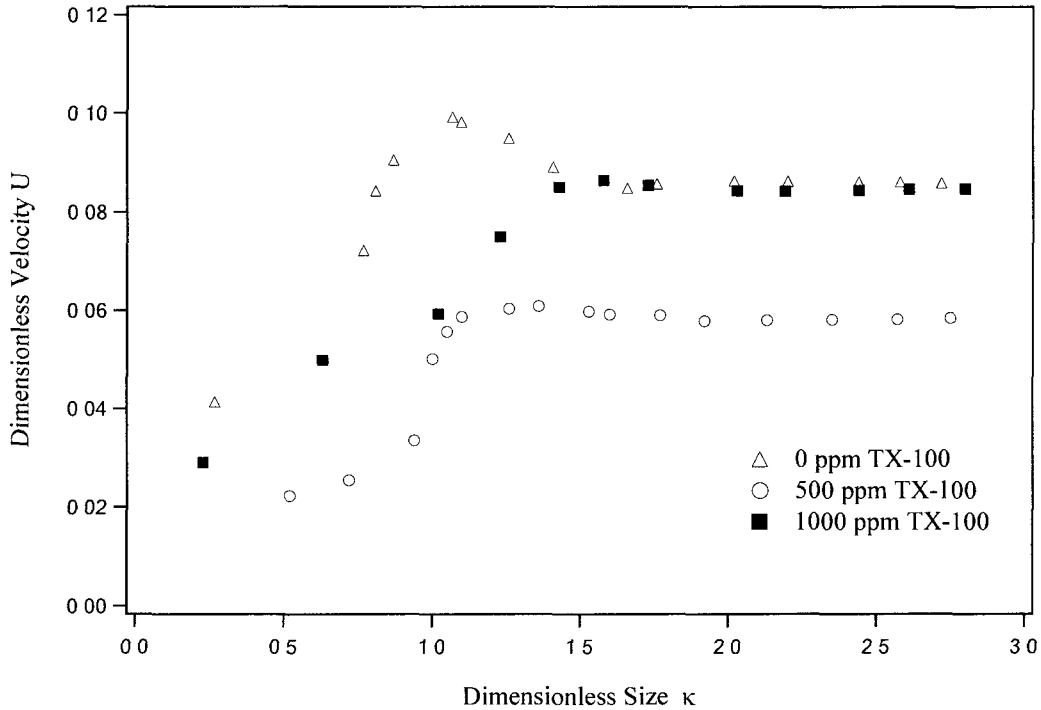


Figure 4.30: The terminal velocity as a function of bubble size for bubble rising in 75 wt% glycerol water solution with various concentration of TX-100 in a 16mm \times 3 mm rectangular channel.

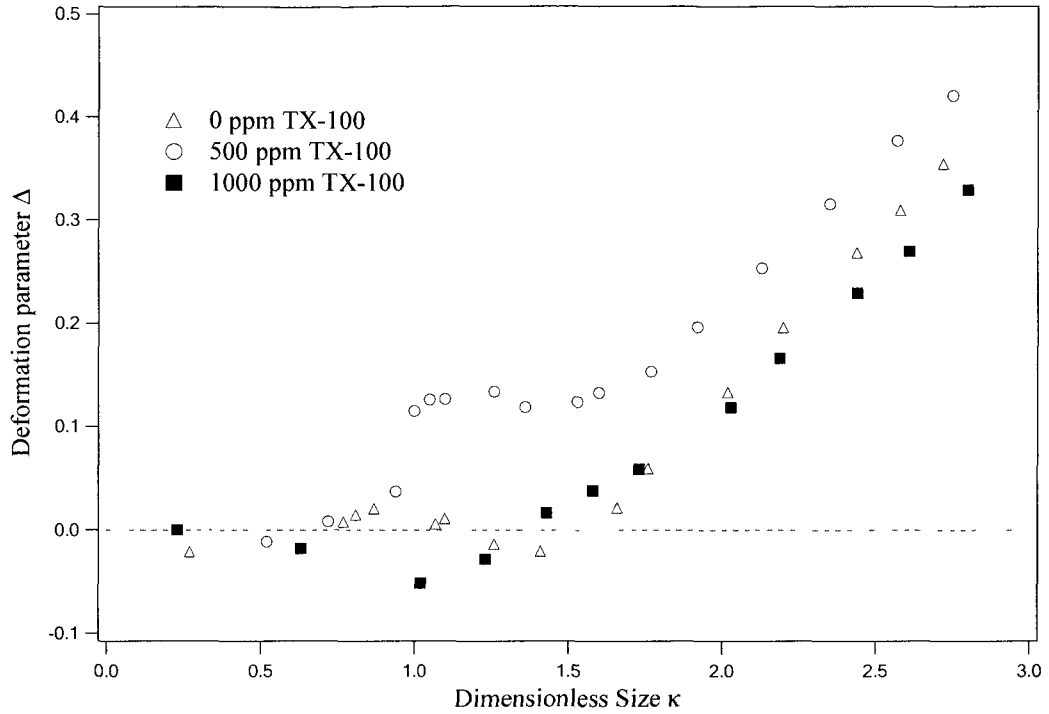


Figure 4.31: Comparison of deformation parameter for steady bubbles rising in 75 wt% glycerol water solution with various concentration (below CMC) of TX-100 in a 16×3 rectangular channel.

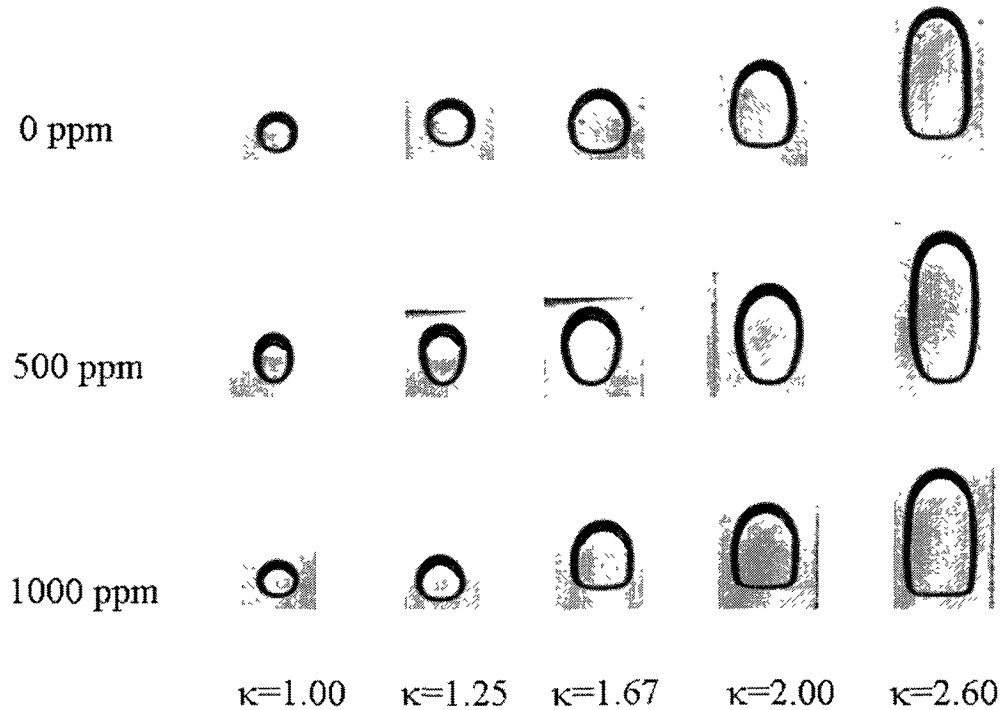


Figure 4.32: Shape comparison for steady bubbles rising in 75 wt% glycerol water solution with various concentration (around CMC) of TX-100 in a 16×3 rectangular channel.

4.2 NON-NEWTONIAN BULK FLUID

4.2.1 Surfactant-free System

In this section, the clean results for bubble rising in a 10mm square channel filled with 2 wt% carboxymethyl cellulose solution (2-C) are shown to aid in comparison with the results for bubbles rising in surfactant solutions. The dimensional terminal velocity, U_d , of the rising bubbles with error bars is shown in Figure 4.33. The shapes of the bubbles corresponding to some of the data points, marked with open circular symbols, are also presented as insets within Figure 4.33. Bubbles at small bubble volumes are nearly spherical in shape. As the bubble volume increases, the bubbles become prolate in the flow direction. As the bubble size becomes comparable to the tube, the bubble becomes more elongated with higher positive curvature at the front of the bubble. For moderate bubble sizes, a distinct cusp is seen instead of flat rear end in viscoelastic fluids. A cusp is formed due to a balance between the extra normal force exerted by the suspending fluid and surface tension. If the extra normal force is larger than the surface tension, a cusp will appear. We did not see a velocity jump for any of the volumes studied. Beyond a critical bubble volume, any increase in the volume of the bubble results in increasing the length of the bubble without affecting the shape of the front and rear ends of the bubble. The terminal velocity of small bubbles increases linearly with increasing bubble volume because of the increased buoyancy force. As the bubble size becomes comparable to the channel size, the drag force due to the confining walls increases resulting in a decrease in the terminal velocity. Beyond a critical bubble volume, the bubble velocity reaches a constant plateau value, U_T , where the bubble velocity is independent of the bubble volume. As seen in Figure 4.33, the choice of frame does not

affect the velocity or volume of the bubble significantly. Larger variation of volume is seen for larger bubble sizes. However, since the velocity of these bubbles reaches a constant value, the shape and location of the velocity-volume curve remains unaffected.

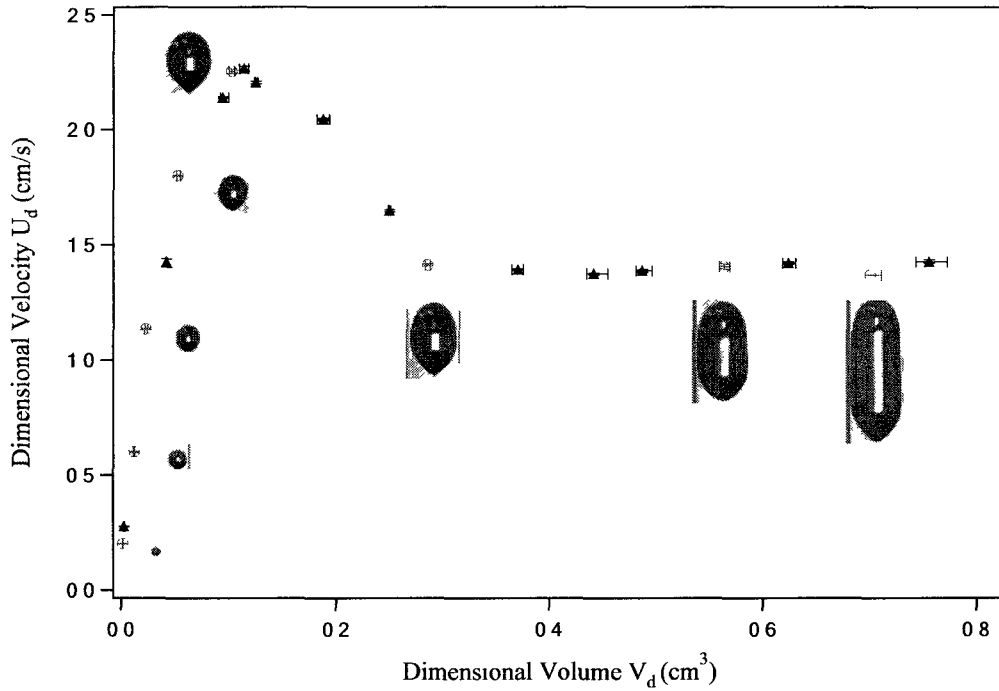


Figure 4.33: Shapes and dimensional terminal velocity of steady bubbles as a function of dimensionless bubble size for bubble rising in 2 wt% carboxymethyl cellulose solution in 10×10mm square channel (2-C). The open symbols correspond to the bubbles presented in the figure.

The velocity of the bubble normalized with the Hadamard-Rybczynski velocity, $U_{HR} = (\rho - \rho_d)g R_{eq}^2 / 3\eta^0$ for a spherical bubble of the same volume rising in an unbounded fluid as a function of the dimensionless bubbles size, κ is shown in Figure 4.34. For small bubble sizes studied ($\kappa < 0.7$) for which the bubble is nearly spherical, the bubble velocity is much faster than the bubble velocity expected for the same bubble in unbounded flow. In the case of Newtonian fluids, the wall effects were seen for very

small bubbles. In calculating the Hadamard-Rybczynski velocity, the zero shear viscosity of the fluid is used. Since carboxymethyl cellulose is a shear-thinning fluid, the actual viscosity of the fluid in the fluid film separating the bubble and the wall is much lower than the zero shear viscosity. Hence, the increased bubble velocity for the bubbles translating in elastic fluids may be attributed to the shear-thinning behavior of the fluids. For large bubble volumes, the steady bubble velocity is only a fraction of its velocity in an unbounded flow ($U_d/U_{HR} \approx 0.25$). From Figure 4.34 we can see that there is very large error in the non-dimensional velocity at smaller bubble sizes because of its dependence on the Hadamard-Rybczynski velocity which in turn depends on the equivalent bubble radius, a . As the bubble size increases, this error reduces sharply.

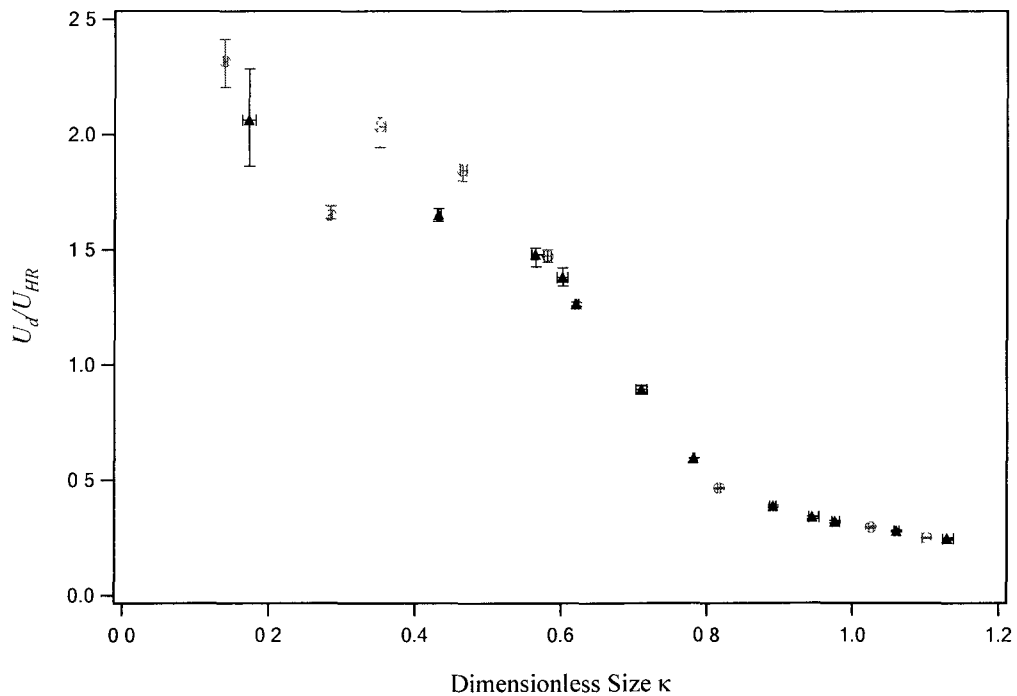


Figure 4.34: Dimensionless terminal velocity of steady bubbles as a function of dimensionless bubble size for bubble rising in 2 wt% carboxymethyl cellulose solution in 10×10 mm square channel (2-C). The open symbols correspond to the bubble shapes presented in Figure 4.34.

The shape of the bubble is quantified by the non-dimensional maximum axial and equatorial length of the bubble, L and B , respectively and the deformation parameter, Δ . The bubble width, B versus the bubble length, L is shown in Figure 4.35 and the deformation parameter Δ , as a function of the dimensionless bubble size for bubbles rising in 2 wt% carboxymethyl cellulose solution in 10mm square channel (2-C) is shown in Figure 4.36. Very small bubbles are nearly spherical as seen in Figures 4.35 and 4.36 where $L = B$ and $\Delta \approx 0$. Even for relatively small bubble sizes compared to the channel size, prolate bubble shapes are seen with $B < L$ and $\Delta > 0$. As the bubble volume increases, the width of the bubble reaches an upper bound less than the size of the channel and any further increase in the bubble volume does not change the width of the bubble. However, the bubble length increases linearly at a much faster rate with increasing bubble volume. As seen in Figure 4.36, the bubbles change shape from spherical ($\kappa < 0.3$) to prolate ($\kappa > 0.3$) with increasing bubble sizes. Figure 4.37 displays the dimensionless film thickness, δ , as a function of bubble size for results shown in Figures 4.33 - 4.36. As seen from the figure, the film thickness thins with the increase of bubble size and seems to reach a constant value for long bubbles similar to the Taylor bubbles in Newtonian bulk fluids. Figures 4.35 - 4.37 show that the error in measuring the shape parameters and the film thickness is small for the entire range of bubble sizes.

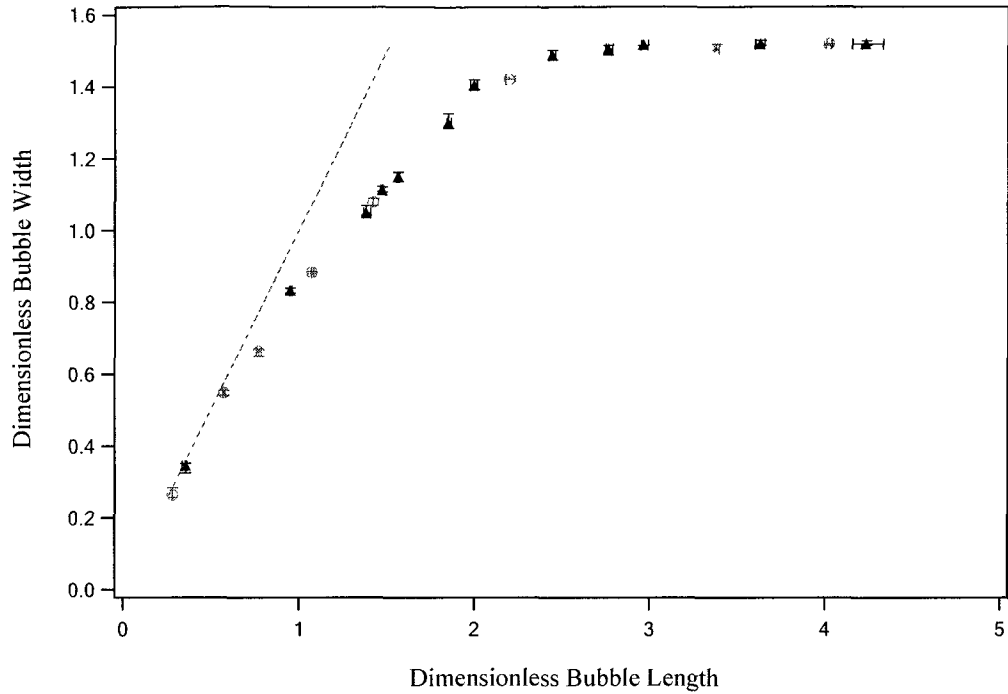


Figure 4.35: The dimensionless bubble width as a function of dimensionless bubble length for bubble rising in 2 wt% carboxymethyl cellulose solution in 10×10mm square channel (2-C). The dashed line represents $L = B$ curve. The open symbols correspond to the bubble shapes presented in Figure 4.34.

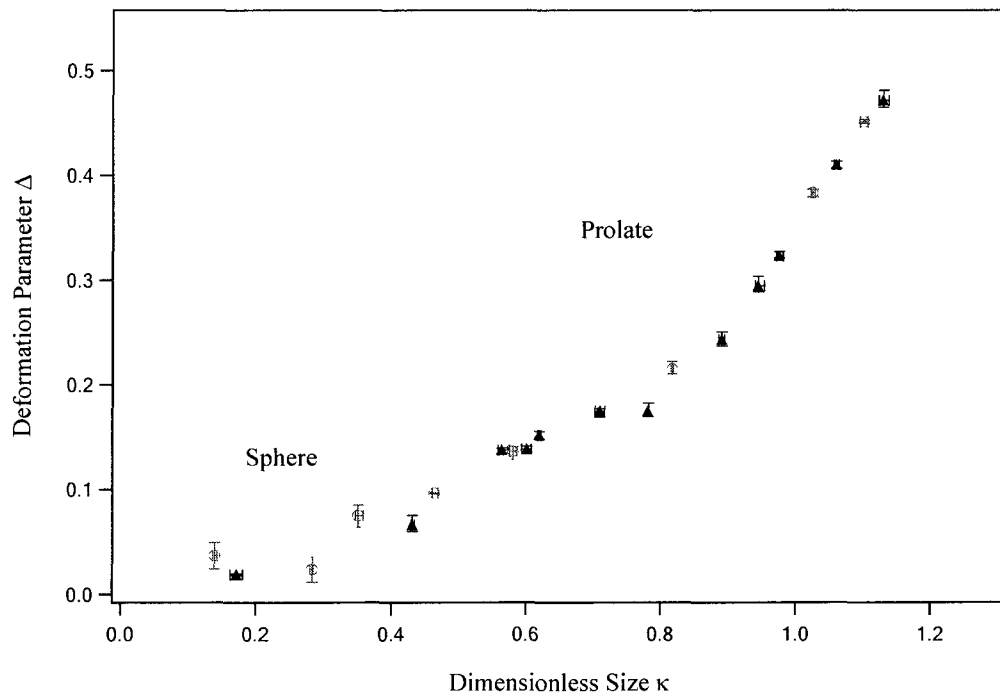


Figure 4.36: Deformation parameter as a function of dimensionless bubble size for bubble rising in 2 wt% carboxymethyl cellulose solution in 10×10 mm square channel (2-C). The open symbols correspond to the bubble shapes presented in Figure 4.34.

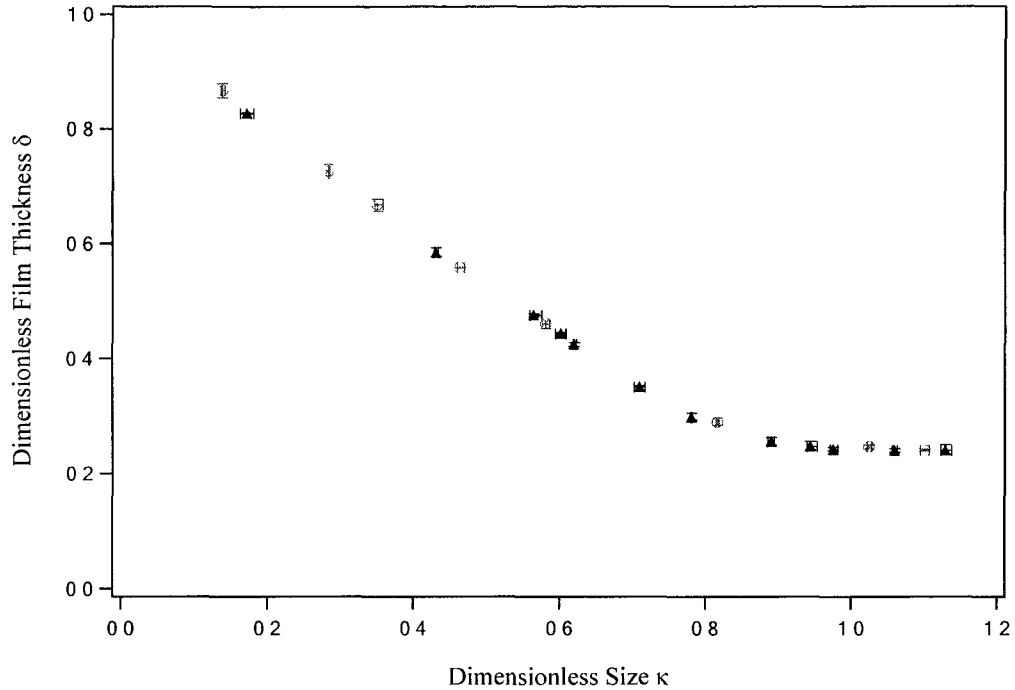


Figure 4.37: The dimensionless film thickness as a function of dimensionless bubble size for bubble rising in 2 wt% carboxymethyl cellulose solution in 10×10mm square channel (2-C). The open symbols correspond to the bubble shapes presented in Figure 4.34.

The dimensional terminal velocity, U_d , as a function of bubble volume, V_d for the rising bubbles in 0.1 wt% polyacrylamide solution and 0.3 wt% polyacrylamide solution in a 10mm square channel is shown in Figure 4.38. As seen in Figure 3.6, both the 0.1 wt% polyacrylamide and 0.3 wt% polyacrylamide solutions show a shear-thinning behavior with zero shear viscosities of 2570 cP and 21670 cP respectively. For both the bulk solutions, the velocity-volume curve for steady bubble motion are similar in shape to that seen for a Newtonian fluid or carboxymethyl cellulose except for the motion of long bubbles. Unlike glycerol-water and carboxymethyl cellulose solutions, instead of reaching a constant plateau value beyond a critical bubble volume, the bubble velocity starts to increase slightly with increasing bubble size. Since the zero shear viscosity of

the 0.3 wt% polyacrylamide solution is nearly eight times as large as that of 0.1 wt% polyacrylamide solution, we expect the terminal velocity of bubbles in the 0.3 wt% polyacrylamide solution to be much smaller than the terminal velocity of bubbles in the 0.1 wt% polyacrylamide solution due to the increased drag force.

The shape comparison for bubbles rising in 0.1 wt% polyacrylamide and 0.3 wt% polyacrylamide solutions in 10mm × 10mm square channel is shown in Figure 4.39. The corresponding deformation parameters and dimensionless film thickness as a function of bubble size are seen in Figures 4.40 and 4.41 respectively. Since both solutions exhibit elasticity, cusps are seen at the rear end of all moderately sized bubbles in the two solutions. The rising bubbles have to cut harder through the more viscous 0.3 wt% polyacrylamide solution compared to the less viscous 0.1 wt% polyacrylamide solution. Thus, the bubbles in the 0.3 wt% polyacrylamide solution have a more prolate shape (see Figure 4.40) with a larger film thickness (see Figure 4.41) as compared to bubbles in the 0.1 wt% polyacrylamide solution. The cusps became less pronounced in 0.3 wt% polyacrylamide solution compared with that in 0.1 wt% polyacrylamide solution.

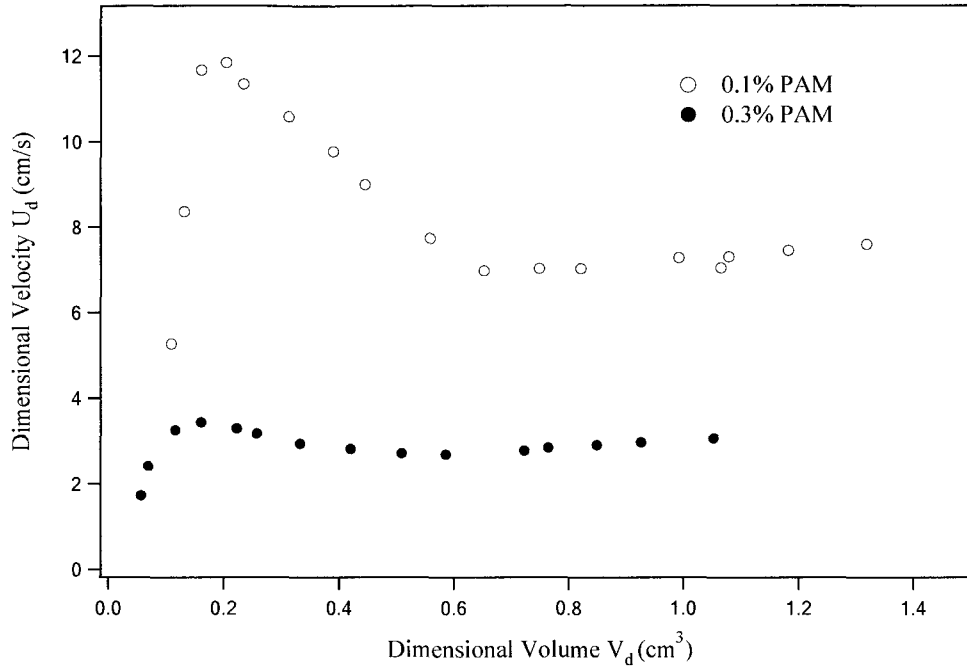


Figure 4.38: Comparison of dimensional terminal velocity of steady bubbles as a function of dimensionless bubble size for bubble rising in 0.1 wt% polyacrylamide solution and 0.3 wt% polyacrylamide solution in 10×10mm square channel, respectively.

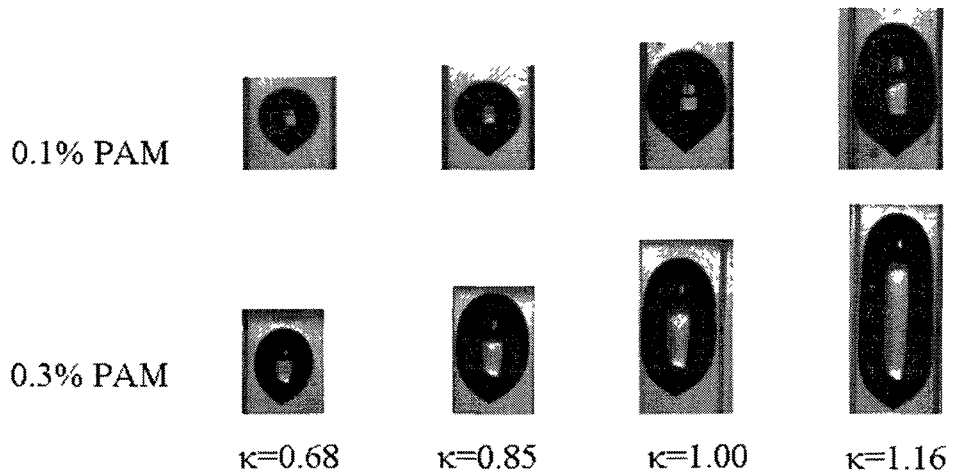


Figure 4.39: Shape comparison for bubble rising in 0.1 wt% polyacrylamide solution and 0.3 wt% polyacrylamide solution in 10×10mm square channel, respectively.

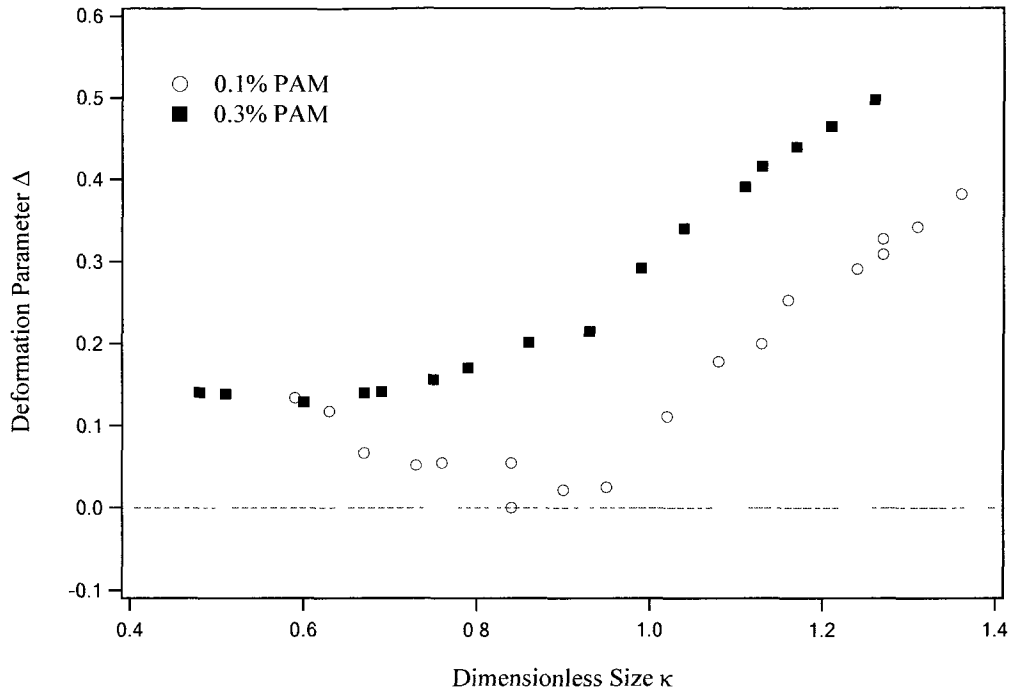


Figure 4.40: Deformation parameter as a function of dimensionless bubble size for bubbles rising in 0.1 wt% polyacrylamide solution (2-P) and 0.3 wt% polyacrylamide solution (2-PP) in 10×10mm square channel.

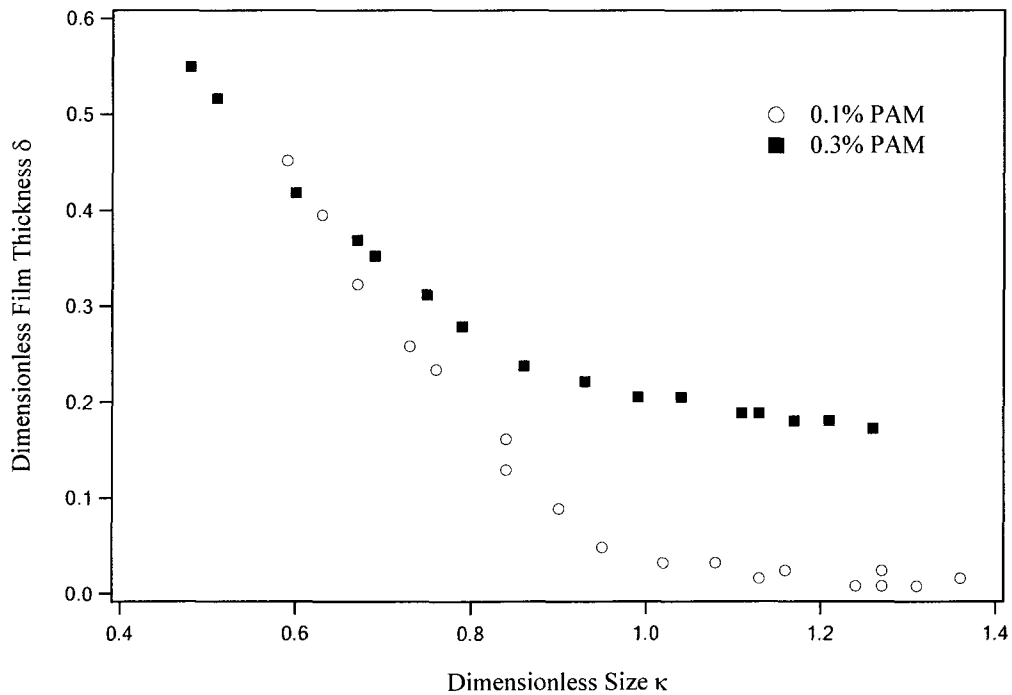


Figure 4.41: Dimensionless film thickness as a function of dimensionless bubble size for bubbles rising in 0.1 wt% polyacrylamide solution (2-P) and 0.3 wt% polyacrylamide solution (2-PP) in 10×10mm square channel.

4.2.2 Surfactant-laden System

The effects of adding surfactant on the motion and deformation of rising bubbles in non-Newtonian solution are presented in this section. In the non-Newtonian bulk solution of 2 wt% carboxymethyl cellulose solution, 0.1 wt% polyacrylamide solution, and 0.3 wt% polyacrylamide solution, Triton X-100 and Tergitol 15-S-9 were added at different concentrations. These surfactants are all water soluble surfactants. While most of the experiments were conducted at bulk concentrations below the critical micellar concentration, experiments were also conducted above CMC for Triton X-100 and Tergitol and this section is divided into two subsections: results below CMC and results above CMC.

4.2.2.1 Surfactant Concentrations Below CMC

For the results presented in this section, the concentrations used here are all below critical micelle concentration (CMC), which indicates that all surfactant molecules are present in the monomer forms. As we mentioned in the Newtonian section, the equilibrium surface tension remains essentially unchanged after adding very small quantities of surfactants to the fluid system. As seen from Figure 3.10, the equilibrium surface tension does not change after adding 1ppm TX-100 (from 73 to 70.5 mN/m) in 2 wt% carboxymethyl cellulose solution. However, the velocity-volume curves are affected due to the non-equilibrium effects which is induced by Marangoni stresses. Figure 4.42 shows the dimensionless terminal velocity as a function of dimensionless bubble size for bubbles rising in 2 wt% carboxymethyl cellulose solution with 1 ppm TX-100 in 10mm × 10mm

square channel. For comparison, the corresponding velocity-volume curve in the absence of surfactants is also shown on the same graph. As seen in Figure 4.42, the general shape of the velocity-volume curve in the presence of small quantities of surfactants (1ppm TX-100) is similar to the velocity-volume curve for surfactant-free system. However, the terminal velocities of small bubbles in low concentration surfactant solutions is lower than similar sized bubbles in surfactant-free solutions due to Marangoni effect as described earlier. The terminal velocities for long bubbles were also slightly affected by the presence of small amounts of surfactants. As the bulk concentration of TX-100 in the 2 wt% carboxymethyl cellulose solution is increased to 100 ppm (see Figure 4.42), the terminal velocity of small as well as large bubbles reduces due to the increased Marangoni effect. The shape of the velocity-volume curve in the presence of 100ppm of surfactants is different from the velocity-volume curve for surfactant-free system. The terminal velocity increases with bubble volume initially, reaches a peak at $\kappa \sim 0.58$ and then starts decreasing again till $\kappa \sim 0.63$. Beyond this bubble size, the bubble velocity increases again, reaches a constant value at $\kappa \sim 0.90$ for long bubbles. The presence of double peaks is similar to the results at higher surfactant concentrations in Newtonian systems (Figures 4.14, 4.17 - 4.19) but the retardation of long bubbles is much larger in the non-Newtonian solutions. Figure 4.43 shows the shape comparison and Figure 4.44 shows the dimensionless film thickness as a function of bubble size for the experiments shown in Figure 4.42. As the surfactant concentration increases from 1 ppm to 100 ppm, the bubbles become more prolate and the film thickness surrounding the bubble increases. The cusp is formed as the normal stresses at the rear of the bubble tends to form a cusp while surface tension forces tend to counter the cusp formation. When surfactant

concentration at the rear of the bubble increases, it weakens the surface tension force resisting the cusp formation. Thus, the bubbles stretch out more forming more pronounced cusps. As a consequence the film thickness surrounding the bubble increases. Since the mobility of the bubble is reduced due to Marangoni stresses and the film thickness increases, the shear rate in the film surrounding the bubble reduces. As a result the apparent viscosity of the shear-thinning fluid also increases, which in turn further lowers that velocity of the rising bubble as it experiences increased drag. A similar reduction in mobility of long bubbles is seen for additions of the nonionic surfactant, Tergitol in 16 mm \times 3 mm rectangular channel with the same bulk fluid (see Figure 4.45).

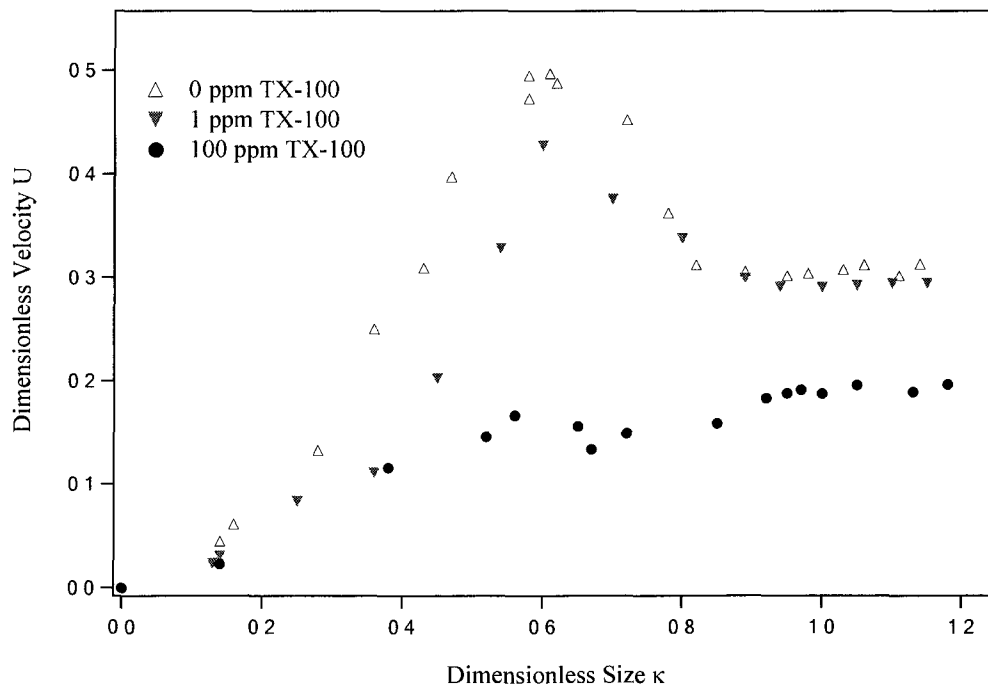


Figure 4.42: The terminal velocity as a function of bubble size for bubbles rising in 2 wt% carboxymethyl cellulose solution with various concentration (below CMC) of TX-100 in a 10mm \times 10 mm square channel.

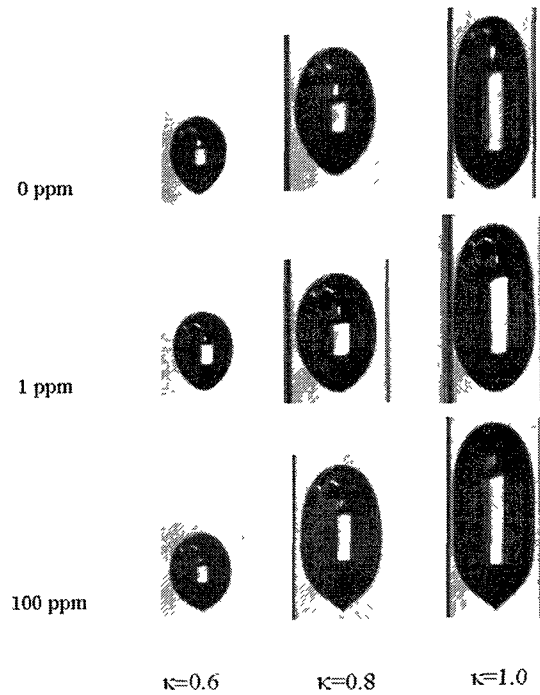


Figure 4.43: Shape comparison for bubbles rising in 2 wt% carboxymethyl cellulose solution with various concentration (below CMC) of TX-100 in a 10mm \times 10 mm square channel.

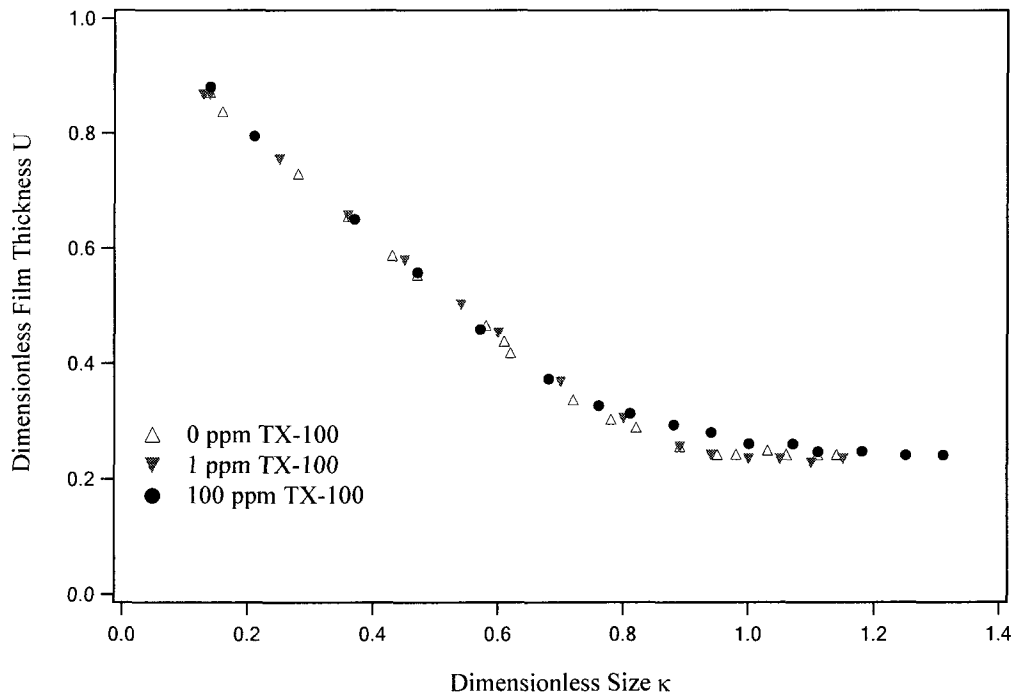


Figure 4.44: Dimensionless film thickness as a function of bubble size for bubbles rising in 2 wt% carboxymethyl cellulose solution with various concentration (below CMC) of TX-100 in a 10mm \times 10 mm square channel.

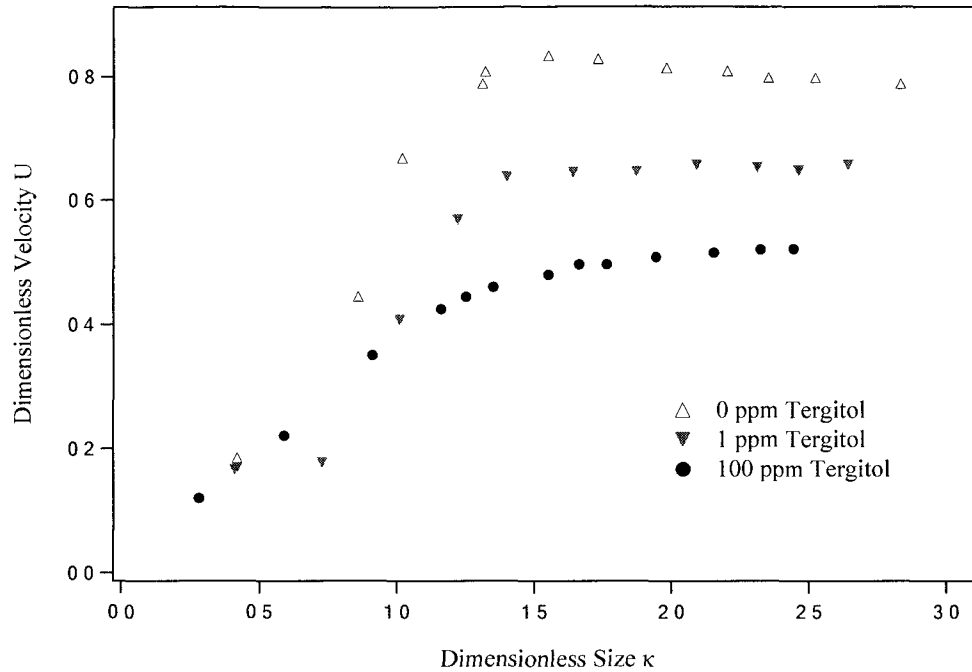


Figure 4.45: The terminal velocity as a function of bubble size for bubble rising in 2 wt% carboxymethyl cellulose solution with various concentration of Tergitol in a 16mm \times 3 mm rectangular channel.

Figure 4.46 presents the dimensionless terminal velocity as a function of dimensionless bubble size for bubble rising in 0.1 wt% polyacrylamide solution with 1 and 100 ppm of TX-100 in a 10mm \times 10mm square channel. For comparison, the corresponding velocity-volume curve in the absence of surfactants is also shown on the same graph. As seen in Figure 4.46, the general shape of the velocity-volume curve in the presence of 1ppm and 100ppm of surfactants is similar to the velocity-volume curve for surfactant-free system. However, the terminal velocities of small bubbles in 1 ppm surfactant solutions is faster than similar sized bubbles in surfactant-free solutions until $\kappa \sim 0.62$. After this critical value, the terminal velocities of the bubbles in 1 ppm surfactant solutions is lower than similar sized bubbles in surfactant-free solutions due to Marangoni effect. As the bulk concentration of TX-100 in the 0.1 wt% polyacrylamide

solution is increased to 100 ppm, when $\kappa < 0.55$, the terminal velocity of small bubbles is larger than similar sized bubbles in surfactant-free and 1 ppm surfactant solutions. When $\kappa > 0.55$, the terminal velocities of bubbles in 100 ppm surfactant solutions is lower than similar sized bubbles in surfactant-free and 1 ppm surfactant solutions due to enhanced Marangoni effect. It appears that the entire curve moves to the left (smaller bubble sizes) with increase in surfactant concentration.

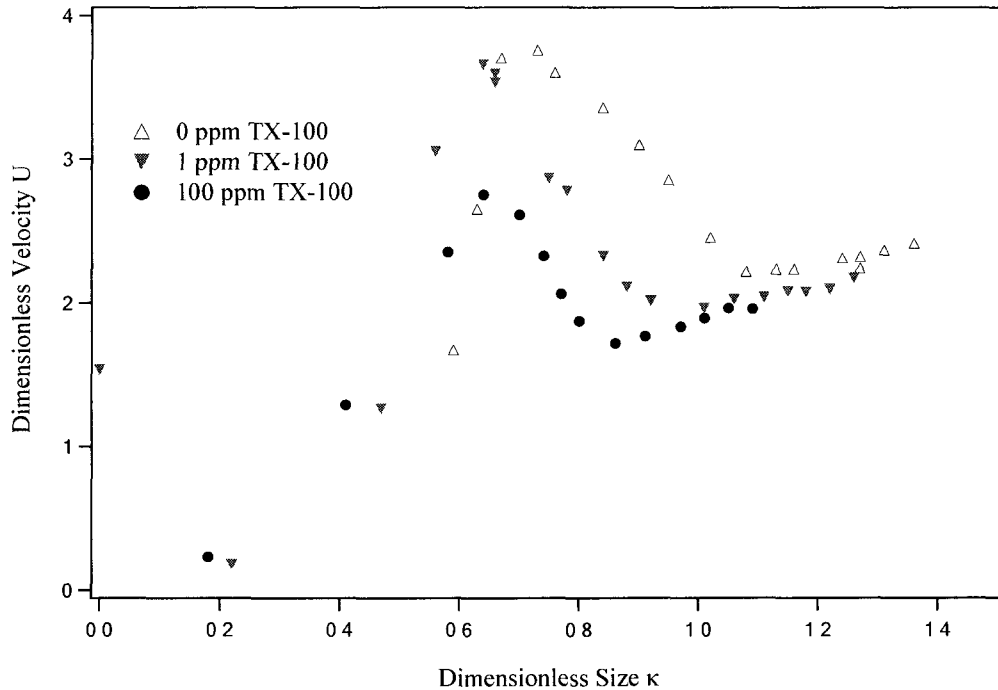


Figure 4.46: The terminal velocity as a function of bubble size for bubbles rising in 0.1 wt% polyacrylamide solution with various concentration (below CMC) of TX-100 in a 10mm \times 10 mm square channel.

The effect of a non-uniform film surrounding the bubble on the velocity of the rising bubbles in 2 wt% carboxymethyl cellulose solution is presented in Figure 4.47, which compares the terminal velocity-volume curve obtained for steady bubbles rising in a

10mm square channel and a circular channel with a hydraulic diameter, $D_H=10\text{mm}$ with the presence of 10ppm TX-100 (1-TC-e and 2-TC-e). The cross sectional area of the square channel is larger than the cross sectional area of the circular tube. The trend of the velocity-volume curve for the bubbles rising in the square channel is similar to that of the velocity-volume curve for the circular channel. The terminal velocity of a long bubble rising in the circular channel is $\approx 28\%$ lower than the velocity of a long bubble rising in the square channel. This is due to the leakage flux at the corners of the square channels which allows the bubbles to expand more radially outward. As a result, the bubbles are more elongated in circular channels as compared to square channels (see Figure 4.48). We can also see from the Figure 4.48 that the cusp is more pronounced in a square geometry.

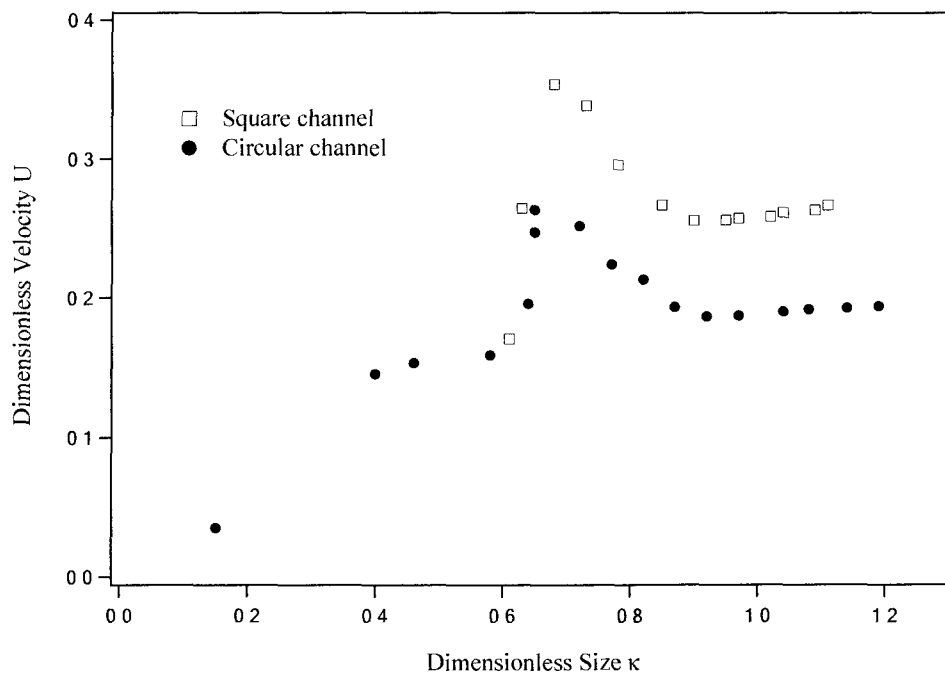


Figure 4.47: The terminal velocity as a function of bubble size for bubble rising in 2 wt% carboxymethyl cellulose solution with 10 ppm Triton X-100 in a circular tube (1-TC-e) and square channel (2-TC-e) with $D_H=10\text{mm}$.

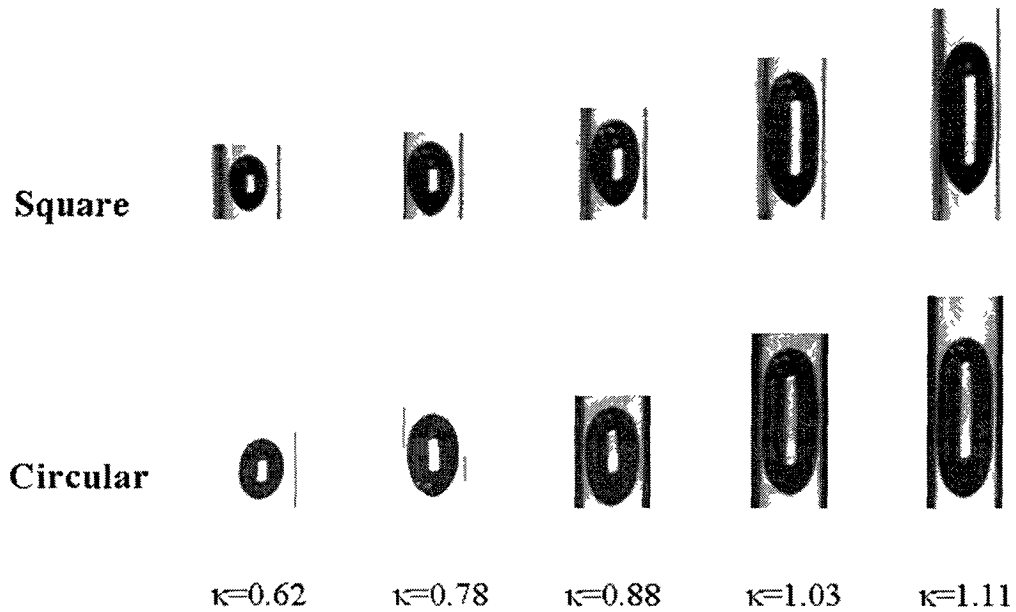


Figure 4.48: The bubble shapes corresponding to different bubble terminal velocity as a function of bubble size for 2 wt% carboxymethyl cellulose water solution with 1000 ppm of Tergitol in 10mm circular tube and 10 × 10 mm square channel.

As discussed in Section 4.1.2.1, the shape of the bubble rising in a rectangular channel is not axisymmetric and the distribution of the surfactants at the rear of the bubble depends on the magnitude of the flow along the sides of the bubble and the thin film separating the bubble from the front walls. In viscoelastic fluids, the surface tension forces in turn govern the shape and length of the cusp seen at the rear of the bubble. The effect of the shape of the confining domain on the cusps formed is seen in Figures 4.43, 4.49 - 4.52. When bubbles are rising in elastic fluids in square channels (Figures 4.43, 4.49, 4.50), the shape of the cusps become more pronounced as the surfactant concentration increases. However, the effect is opposite when bubbles are rising in a rectangular channel (Figures 4.51 and 4.52).

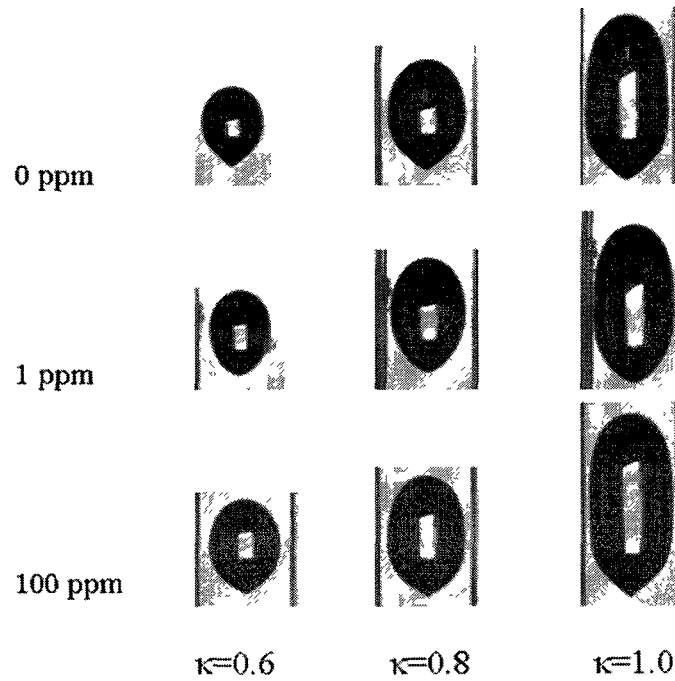


Figure 4.49: Shape comparison for bubbles rising in 2 wt% carboxymethyl cellulose solution with various concentration of Tergitol in 10mm \times 10 mm square channel.

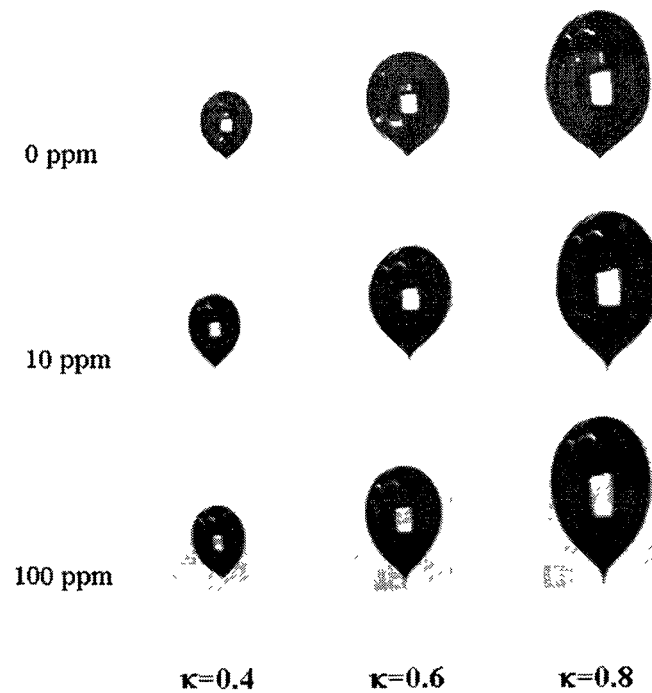


Figure 4.50: Shape comparison for bubbles rising in 2 wt% carboxymethyl cellulose solution with various concentration of TX-100 in 15 mm \times 15 mm square channel.

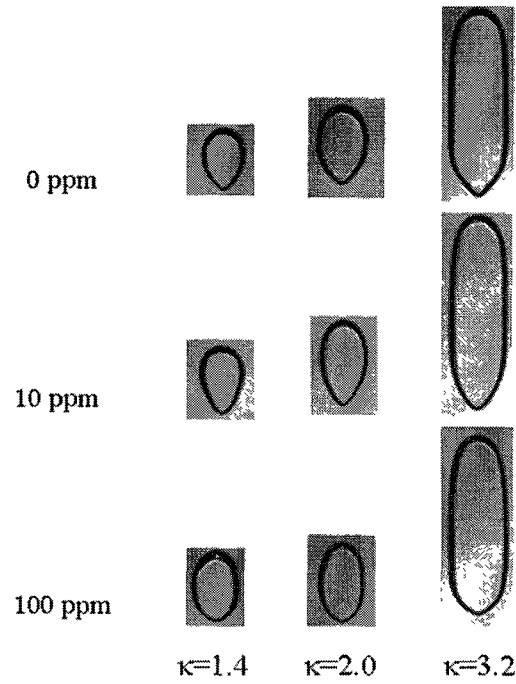


Figure 4.51: The bubble shapes corresponding to different bubble terminal velocity as a function of bubble size for 2 wt% carboxymethy cellulose solution with various concentration of Triton X-100 in 16mm × 3 mm rectangular channel.

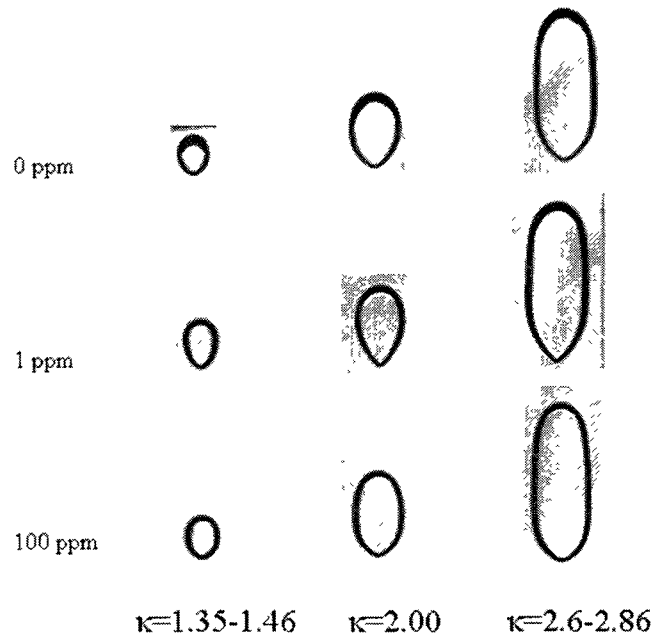


Figure 4.52: The bubble shapes corresponding to different bubble terminal velocity as a function of bubble size for 2 wt% carboxymethy cellulose solution with various concentration of Tergitol in 16mm × 3 mm square channel.

4.2.2.2 Surfactant Concentrations Above CMC

When surfactant concentration is raised to values above the CMC, remobilization of the interface is observed. This is shown clearly in Figure 4.53 where the terminal velocity is plotted as a function of bubble size for bubble rising in 0.1 wt% polyacrylamide solution with concentration of TX-100 above CMC (1000ppm) in a 10 mm × 10 mm square channel. For comparison, the velocity-volume curve in the absence of surfactant (0 ppm) and 100 ppm TX-100 is also plotted on the same graph. As seen in Figure 4.53, the terminal velocity of small bubbles with 1000 ppm TX-100 is almost the same as the similar sized bubbles in a clean 0.1 wt% polyacrylamide solution. However, for long bubbles, the terminal velocity is slightly higher than that for long bubbles rising in a clean 0.1 wt% polyacrylamide solution. Unlike Newtonian fluids, remobilization is seen for the entire range of bubble sizes in case of non-Newtonian bulk fluids. Figure 4.54 shows the shape comparison for bubble rising in 0.1 wt% polyacrylamide solution in 10×10mm square channel with various concentration of TX-100. The shape of the bubbles become more prolate as the surfactant concentration is increased from 0 ppm to 100 ppm because of accumulation of surfactants at the rear of the bubble which result in the stretching out of the cusp. As the surfactant concentration is increased to 1000 ppm surfactant solution the bubbles again become more oblate similar to the bubbles rising in a solution in the absence of surfactant. Moreover, the cusp tends to become less pronounced with increase in surfactant concentration.

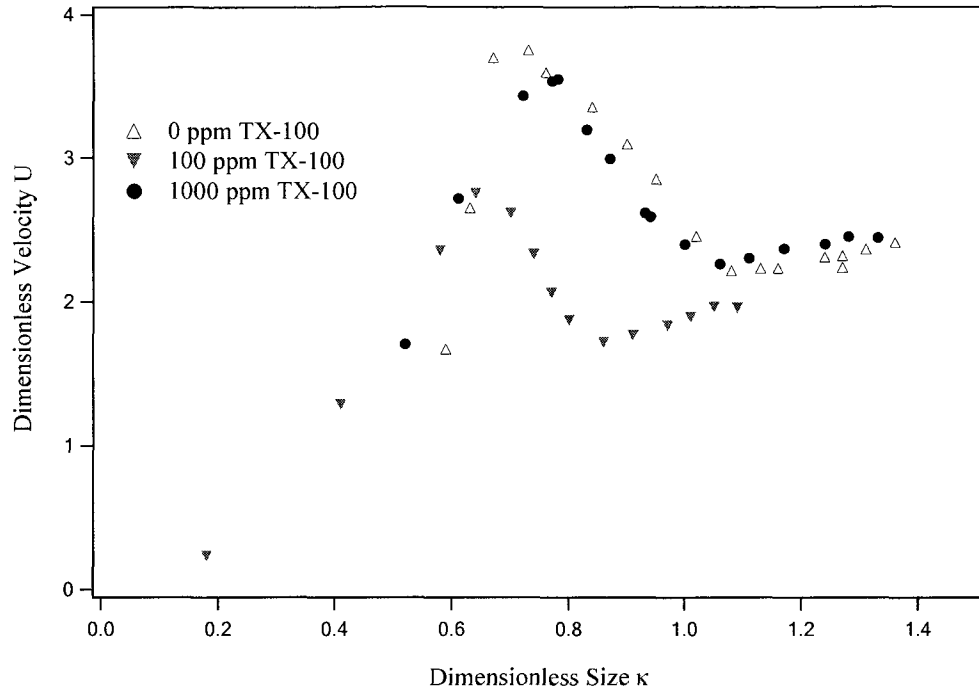


Figure 4.53: The terminal velocity as a function of bubble size for bubbles rising in 0.1 wt% polyacrylamide solution with various concentration of TX-100 in a 10mm \times 10 mm square channel.

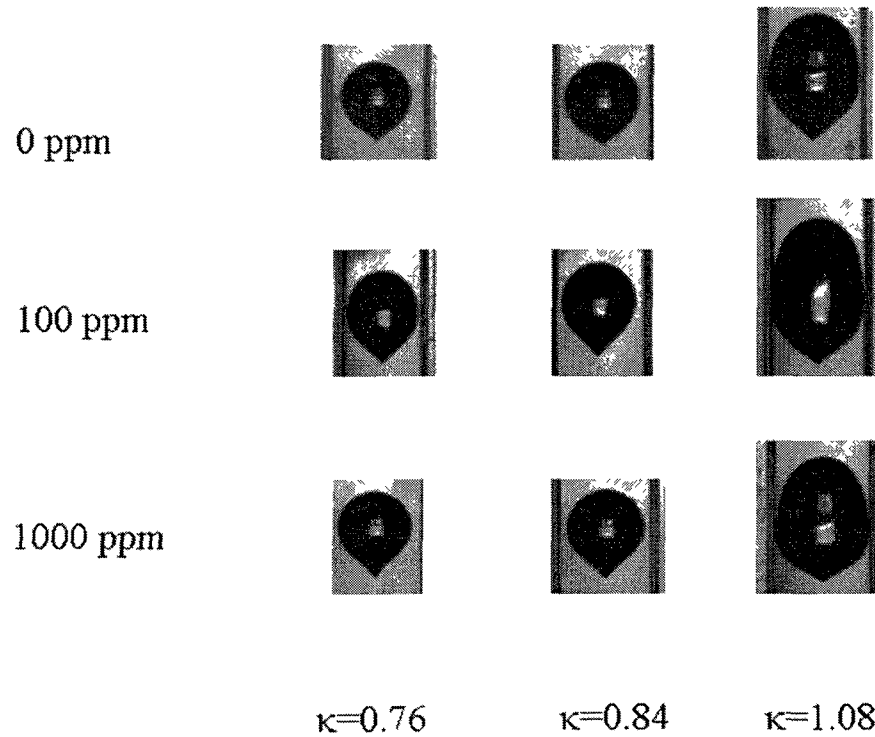


Figure 4.54: Shape comparison for bubble rising in 0.1 wt% polyacrylamide solution in 10 \times 10mm square channel.

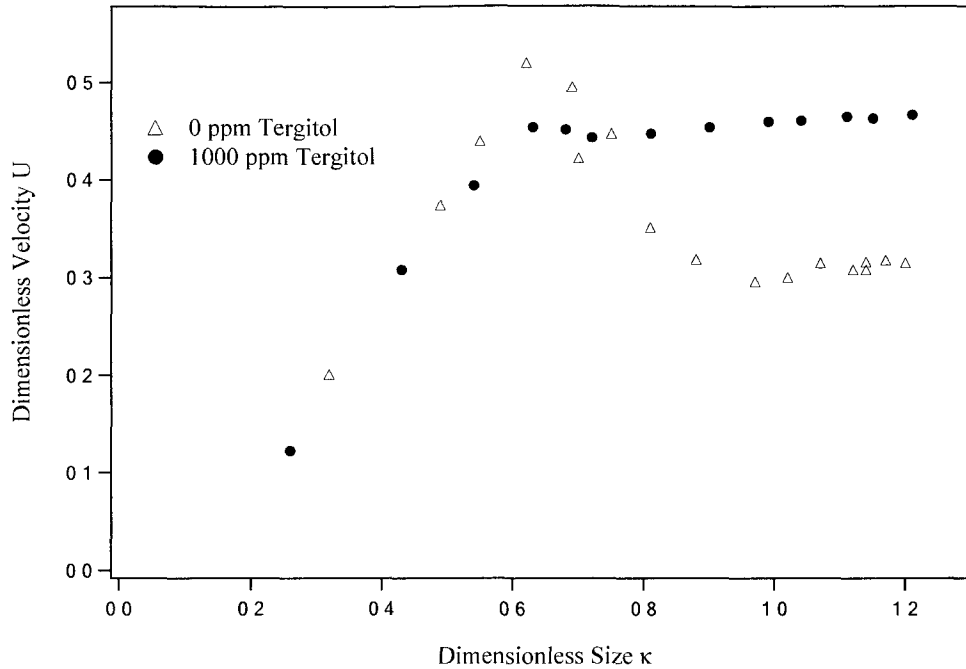


Figure 4.55: The terminal velocity as a function of bubble size for bubble rising in 2 wt% carboxymethyl cellulose solution with various concentration of Tergitol in 10mm × 10 mm square channel.

Remobilization of the interface is also seen for bubbles rising in 2 wt% carboxymethyl cellulose solution with concentration of Tergitol above CMC in 10mm × 10 mm square channel (Figure 4.55). As seen from Figure 4.55, the shape of the velocity-volume curve with 1000 ppm Tergitol in a 10×10 mm square channel is different from that in the surfactant-free case. There is a very small peak in the presence of 1000 ppm Tergitol in 2 wt% carboxymethyl cellulose solution in the square geometry. The terminal velocity of long bubbles in the 1000 ppm Tergitol solution is also much larger than that of similar sized bubbles in the 0 ppm solution. Similar enhancement in the mobility of long bubbles is seen for bubbles rising in 16 mm x 3 mm rectangular channels filled with 2 wt% carboxymethyl cellulose with concentration of TX-100 above CMC (Figure 4.56) and concentration of Tergitol above CMC (Figure 4.57). In all the cases, the bubbles in the

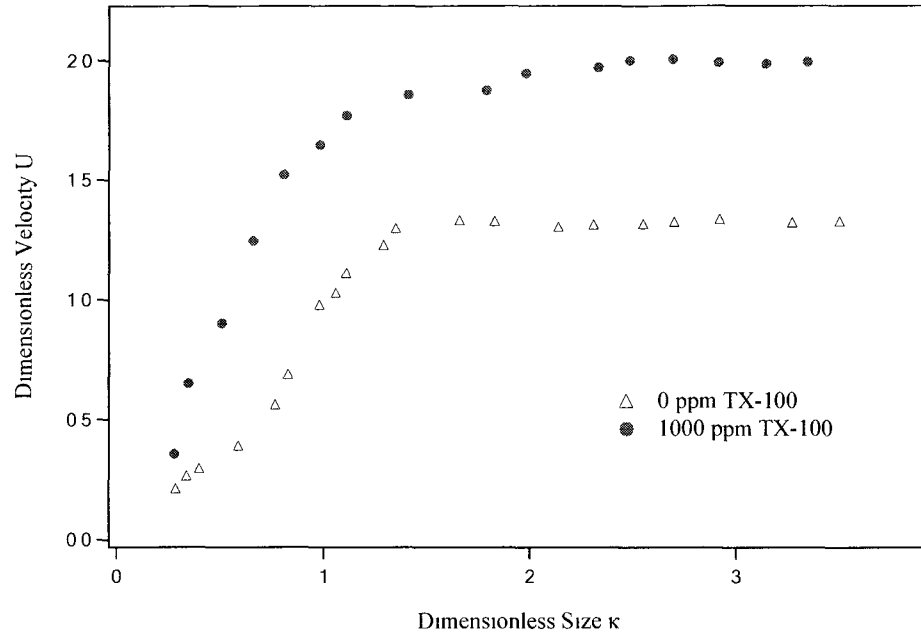


Figure 4.56: The terminal velocity as a function of bubble size for bubble rising in 2 wt% carboxymethyl cellulose solution with various concentration of Triton X-100 in 16mm \times 3 mm rectangular channel.

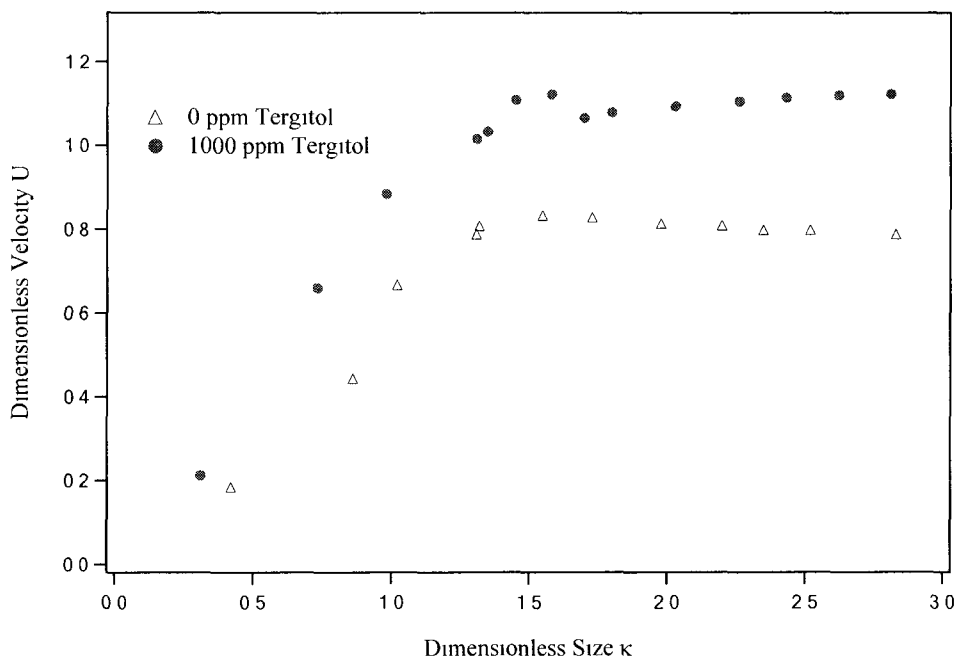


Figure 4.57: The terminal velocity as a function of bubble size for bubble rising in 2 wt% carboxymethyl cellulose solution with various concentration of Tergitol in 16mm \times 3 mm rectangular channel.

1000 ppm solution were more prolate than the surfactant-free case, but it is not clear if that is the reason why this enhanced mobility is seen for bubbles above the critical micellar concentration.

Chapter 5

SUMMARY AND FUTURE WORK

In this thesis, buoyancy-driven motion of bubbles in the presence of soluble surfactants was studied at finite Reynolds numbers. A single bubble was injected into a vertically positioned channel filled with an immiscible bulk fluid. Both Newtonian and non-Newtonian fluids were used as the bulk solution. The movement and deformation of the bubble was captured by a CMOS digital video camera. The steady shape, bubble size, bubble terminal velocity, film thickness, deformation parameter were analyzed by “Vision Assistant” software from captured frames. The effect of how bulk soluble surfactants affect the mobility and shape of air bubbles rising in confined domains filled with a liquid was investigated. Various geometries were used to determine how surfactants affect bubble shapes in different geometries.

In surfactant-free 75 wt% glycerol water solution, bubbles at small bubble sizes were nearly spherical in shape. As the bubble size increased, the bubbles became oblate losing fore and aft symmetry. As the bubble size became comparable to the tube, the bubble became more elongated with higher positive curvature at the front of the bubble. Beyond a critical bubble size, any increase in the volume of the bubble resulted in increasing the length of the bubble without affecting the shape of the front and rear ends of the bubble. The terminal velocity of small bubbles increased linearly with increasing bubble volume

because of the increased buoyancy force. As the bubble size became comparable to the channel size, the drag force due to the confining walls increased resulting in a decrease in the terminal velocity. Beyond a critical bubble volume, the bubble velocity reached a constant plateau value, where the bubble velocity was independent of the bubble volume. In 2 wt% carboxymethyl cellulose solution, bubbles changed directly from spherical to long elongated bubbles without taking on an oblate shape. The general shape of the velocity-volume curve was similar to the 75 wt% glycerol water solution case. Bubble shape transition similar to the 75 wt% glycerol-water solution was observed for bubbles rising in 0.1 wt% and 0.3 wt% polyacrylamide solutions. However, the velocity-volume curve did not reach a constant plateau value beyond a critical bubble volume, instead the bubble velocity increased slightly as the bubble volume increased. For bubbles rising in all the tested viscoelastic fluids in this thesis, a pointed cusp was observed at the trailing end of the bubbles due to the extra normal force exerted by the fluid. The cusp appeared to be axisymmetric for all the runs performed. No velocity jump was observed for viscoelastic fluids.

Different surfactants with varying concentrations below and above CMC were added to both the Newtonian and non-Newtonian bulk solutions. In the presence of very small quantities of surfactants the equilibrium surface tension did not change from its clean interface value. However, the terminal velocity for small bubbles was found to be lower than that of the surfactant-free system due to the non-equilibrium effects. Long bubbles

seemed to be unaffected by the presence of small amounts of surfactants. The surfactants were swept to the trailing end of the bubble and accumulated near the trailing pole due to surface convection. A non-uniform distribution of surfactants along the interface establishes a surface tension gradient which generates Marangoni stresses. The Marangoni stresses oppose the surface velocity resulting in a retardation of the overall mobility of the bubbles. Increasing surfactant concentration enhanced the Marangoni effect and the bubbles were further immobilized.

The general shape of velocity-volume curve with low concentration of surfactants was similar to the surfactant-free case. A change in shape of the velocity-volume curve was also seen for moderate surfactant concentrations. Two peaks were observed for 75 wt% glycerol water solution case with moderate surfactant concentrations for several surfactants in different channel geometries. In the presence of surfactants the bubbles moved slower with a more prolate shape. The deformation for bubbles moving in a rectangular channel in the presence of surfactants differed from bubbles rising through square and circular channels where the bubble shapes are axisymmetric.

When the surfactant concentration was above CMC, a uniform surfactant concentration was obtained along the interface. The surface tension gradient as well as the Marangoni stress was reduced resulting in partial remobilization. In 75 wt% glycerol-water solution, the terminal velocity of long bubbles was the same as that for the surfactant-free case.

Complete remobilization was not observed for small bubbles for any of the surfactant systems or geometries studied. However, in 0.1 wt% and 0.3 wt% polyacrylamide solutions, the terminal velocity of long bubbles was slightly higher than that of the surfactant-free case. In 2 wt% carboxymethyl cellulose solution in a rectangular geometry, the terminal velocity of long bubbles was much higher than the terminal velocity of long bubbles for the surfactant-free case.

The effect of surfactants on the bubble shape depended on the geometry of the confining walls. Cusps became more pronounced with increasing surfactant concentration for bubbles rising in circular and square channels filled with viscoelastic fluids. This was expected as elasticity caused cusps to form and surface tension forces opposed the cusp formation. With the addition of surfactants, surface tension forces were reduced at the rear of the bubble resulting in more pronounced cusps. In contrast, cusps for bubbles rising through viscoelastic fluids in a rectangular geometry tended to disappear with increasing surfactant concentration. This could be attributed to the non-axisymmetric shape the bubbles take in the rectangular channel and the distribution of the surfactants at the rear of the bubble depended on the thin film separating the bubble from the front wall. We also compared the velocity-volume curve for bubbles rising in a square channel with that for bubbles rising in a circular tube in the absence and presence of surfactants. The trend of the velocity-volume curve for the bubbles rising in a square channel is similar to that of the velocity-volume curve for a circular channel. However, the terminal velocities

for all bubbles moving in square channel were larger than those in circular channel due to leakage flux at the corners of the channel. In addition, the bubbles were more elongated in circular tubes compared to same sized bubbles in square channels.

The buoyancy-driven motion of bubbles in the presence of surfactants in confined domains is an important problem of great interest due to its application in many fields such as enhanced oil recovery, microfluidics, and solvent extraction. The results of this thesis are a first attempt at characterizing the buoyancy-driven motion of bubbles in non-circular channels in the presence of surfactants. Several future directions are suggested as follows to further exploit two-phase flow in confined domains:

- Investigate surfactant effects on the same type of fluids with different viscosities.
- Experiment on viscous drops other than air bubbles.
- Perform experimental and numerical studies for a wider range of Reynolds, Bond, and capillary numbers.
- Exploit surfactant effects on the microscale.
- Investigate new surfactants with different interface kinetics and new suspending fluids.

REFERENCES

- [1] L. Amaya-Bower, T. Lee, 2011. Numerical simulation of single bubble rising in vertical and inclined square channel using lattice Boltzmann method. *Chemical Engineering Science*, 66, 935–952.
- [2] G. Astarita, G. Apuzzo, 1965. Motion of Gas Bubbles in Non-Newtonian Liquids. *A.I.Ch.E. Journal*. 11(5), 815-820.
- [3] A. Belmonte, 2000. Self-oscillations of a cusped bubble rising through a micellar solution. *Rheol Acta*. 39, 554-559.
- [4] D. Bhaga, M.E. Weber, 1981. Bubbles in viscous liquids: shapes, wakes and velocities. *J. Fluid Mech.*, 105, 61-85.
- [5] Q.C. Bi, T.S. Zhao, 2001. Taylor bubbles in miniaturized circular and noncircular channels. *International Journal of Multiphase Flow*. 27, 561-570.
- [6] A. Borhan, J. Pallinti, 1995. Buoyancy-driven motion of viscous drops through cylindrical capillaries at small Reynolds numbers. *Ind. Eng. Chem. Res.* 34, 2750-2761.
- [7] F.P. Bretherton, 1961. The motion of long bubbles in tubes. *J. Fluid Mech.*, 10, 166-188.
- [8] J. D. Bugg, G. A. Saad, 2002. The velocity field around a Taylor bubble rising in a stagnant viscous fluid: numerical and experimental results. *Intl J. Multiphase Flow*. 28, 791–803.
- [9] J. Chen, K.J. Stebe, 1996. Marangoni retardation of the terminal velocity of a settling droplet: the role of surfactant physico-chemistry. *J. colloid and interface science*. 178, 144-155.
- [10] R. P. Chhabra, 2007. Bubbles, drops, and particles in non-Newtonian fluids (2nd Edition). Taylor&Francis Group.
- [11] C. Clanet, P. Héraud, G. Searby, 2004. On the motion of bubbles in vertical tubes of arbitrary cross-sections: some complements to the Dumitrescu–Taylor problem. *J. Fluid Mech.* 519, 359-376.
- [12] B. Cuenot., J. Magnaudet, B. Spennato, 1997. The effects of slightly soluble surfactants on the flow around a spherical bubble. *J. Fluid Mech.* 339, 25-53.

- [13] E.C. Donaldson, G.V. Chilingarian, T.F. Yen, 1989. Enhanced Oil Recovery: Processes and operations. Elsevier Science Publisher B.V.
- [14] J.Q. Feng, 2008. Buoyancy-driven motion of a gas bubble through viscous liquid in a round tube. *J. Fluid Mech.* 609, 377–410.
- [15] A. Frumkin, V.G. Levich, 1947. On surfactants and interfacial motion. *Zh. Fiz. Khim.* 21, 1183–204.
- [16] J. Hadamard, 1911. Movement permanent lent d'une sphere liquide et visqueuse. Dansun liquide visqueux, Comptes Rendus Hebdomadaires des Seances de l' *Academie des Sciences.* 152, 1735-1743.
- [17] J.R. Herrera-Velarde, R. Zenit, D. Chehata, B. Mena, 2003. The flow of non-Newtonian fluids around bubbles and its connection to the jump discontinuity. *J. Non-Newtonian Fluid Mech.* 111, 199–209.
- [18] R.A. Johnson, A. Borhan, 2003. Pressure-driven motion of surfactant-laden drops through cylindrical capillaries: effect of surfactant solubility. *J. Colloid and Interface Science.* 261(2), 529-541.
- [19] W.B. Kolb, R.L. Cerro, 1991. Coating the inside of a capillary of square cross-section. *Chemical Engineering Science.* 46(9), 2181-2195.
- [20] W.B. Kolb, R.L. Cerro, 1993. The motion of long bubbles in tubes of square cross section. *American Institute of Physics.* 5 (7), 1549-1557.
- [21] M. Krzan, K. Lunkenheimer, K. Malysa, 2004. On the influence of the surfactant's polar group on the local and terminal velocities of bubbles. *Colloids and Surfaces A: Physicochem. Eng. Aspects,* 250, 431–441.
- [22] V.G. Levich, 1962. *Physicochemical Hydrodynamics.* Englewood Cliffs, NJ: Prentice Hall.
- [23] J. Li, V. Bulusu, N.R. Gupta, 2008. Buoyancy-driven motion of bubbles in square channels. *Chemical Engineering Science,* 63, 3766-3774.
- [24] Q. Liao, T.S. Zhao, 2003. Modeling of Taylor bubble rising in a vertical mini noncircular channel filled with a stagnant liquid. *International Journal of Multiphase Flow.* 29, 411-434.
- [25] S.J. Lind, T.N. Phillips, 2010. The effect of viscoelasticity on a rising gas bubble. *J. Non-Newtonian Fluid Mech.* 165, 852–865.
- [26] Y.J.Liu, T.Y.Liao, D.D. Joseph, 1995. A two-dimensional cusp at the trailing edge of an air bubble rising in a viscoelastic liquid. *J. Fluid Mech.* 304, 321-342.

- [27] X.L. Luo, 1999. Numerical simulation of Weissenberg phenomena-the rod-climbing of viscoelastic fluids. *Comput. Methods Appl. Mech. Engrg.* 180, 393-412.
- [28] R. Nagarajan, E. Ruckenstein, 1991. Theory of surfactant self-assembly: a predictive molecular thermodynamic approach. *Langmuir.* 7, 2934 – 2968.
- [29] G.A. Nuñez, G.S. Ribeiro, M.S. Arney, J.Feng, D.D Joseph, 1994. Rod climbing and normal stresses in heavy crude oils at low shears. *J.Rheol.* 38(5), 1251-1270.
- [30] D. Ohlendorf, W.I.H. Hoffmann, 1986. Surfactant systems for drag reduction: Physico-chemical properties and rheological behaviour. *Rheol. Acta.* 25, 468-486.
- [31] R. Palaparthi, D.T. Papageorgiou, C. Maldarelli, 2006. Theory and experiments on the stagnant cap regime in the motion of spherical surfactant-laden bubbles. *J. Fluid Mech.* 559, 1-44.
- [32] S. Polonsky, L. Shemer, D. Barnea, 1999. The relation between the Taylor bubble motion and the velocity field ahead of it. *Int. J. Multiphase Flow.* 15, 957-975.
- [33] D. Rodrigue, J.F. Blanchet, 2002. Surface Remobilization of Gas Bubbles in Polymer Solutions Containing Surfactants. *J.Colloid and Interface Science.* 256, 249–255.
- [34] D. Rodrigue, D.D. Kee, C.F. Chan Man Fong, 1996. An experimental study of the effect of surfactants on the free rise velocity of gas bubbles. *J. Non-Newtonian Fluid Mech.*, 66, 213-232.
- [35] D. Rodrigue, D.D. Kee, C.F. Chan Man Fong, 1998. Bubble velocities: further developments on the jump discontinuity. *J. Non-Newtonian Fluid Mech.*, 79 , 45–55.
- [36] D. Rodrigue, D. De Kee, C.F. Chan Man Fong, 1999. The slow motion of a single gas bubble in a non-Newtonian fluid containing surfactants. *J. Non-Newtonian Fluid Mech.* 86, 211-227.
- [37] M.J. Rosen, 2004. *Surfactants and Interfacial Phenomena* Third Edition. John Wiley & Sons, Inc.,USA.
- [38] Rybczynski, 1911. Über die fortschreitende Bewegung einer flüssigen Kugel in einem sachen Medium, *Bull. Intern. Acad. Sci. Cracovie (Ser. A).* 1, 40-46.
- [39] T. Saito, K. Sakakibara, Y. Miyamoto, M. Yamada, 2010. A study of surfactant effects on the liquid-phase motion around a zigzagging-ascent bubble using a recursive cross-correlation PIV. *Chemical Engineering Journal.* 158, 39–50.

- [40] K.J.Stebe., C. Maldarelli, 1994. Remobilizing surfactant retarded fluid partial interfaces II. Controlling the surface mobility at interfaces of solutions containing surface active components. *J. colloid and interface science*. 163, 177-189.
- [41] R.G. Sousa, S.Nogueira, A.M.F.R. Pinto, M.L. Reithmuller, J.B.L.M. Campos, 2004. Flow in the negative wake of a Taylor bubble rising in viscoelastic carboxymethyl cellulose solutions: particle image velocimetry measurements. *J. Fluid Mech.* 511, 217-236.
- [42] R.G. Sousa, A.M.F.R. Pinto, J.B.L.M. Campos, 2005. Flow around individual Taylor bubbles rising in stagnant CMC solutions: PIV measurements. *Chem.Eng.Sci.*60,1859-1873.
- [43] R.G. Sousa, A.M.F.R. Pinto, J.B.L.M. Campos, 2006. Flow around individual Taylor bubbles rising in stagnant polyacrylamide (PAA) solutions: PIV measurements. *J. non-Newtonian fluids*. 135, 16-31.
- [44] G. I. Taylor, 1960. Deposition of a viscous fluid on the wall of a tube. *J.Fluid Mech.* 10, 161-165.
- [45] A. Tomiyama, G.P. Celata, S. Hosokawa, S. Yoshida, 2002. Terminal velocity of single bubbles in surface tension force dominant regime. *International J. Multiphase Flow*. 28, 1497-1519.
- [46] T. Touhami, D. Rana, G.H. Neale, V. Hornof, 2001. Study of polymer-surfactant interactions via surface tension measurements. *Colloid Polym. Sci.* 279, 297-300.
- [47] F.M. White, 1999. *Fluid Mechanics (4th Edition)*. McGraw-Hill.
- [48] W. Yan, C. A. Miller, G. J. Hirasaki, 2006. Foam sweep in fractures for enhanced oil recovery. *Colloids & Surfaces A: Physico. Eng. Aspects*. 282-283, 348-359.
- [49] J. Yue, L. Luo, Y.Gonthier, G. Chen, Q. Yuan, 2009. An experimental study of air-water Taylor flow and mass transfer inside square microchannels. *Chemical Engineering Science*. 64, 3697- 3708.
- [50] Y. Zhang, J. A. Finch, 2001. A note on single bubble motion in surfactant solutions. *J. Fluid Mech.* 429, 63-66.
- [51] Y. Zhang, J. B. McLaughlin, J. A. Finch, 2001. Bubble velocity profile and model of surfactant mass transfer to bubble surface. *Chemical Engineering Science*. 56, 6605-6616.